ROYAL SOCIETY OF CHEMISTRY

REVIEW

Check for updates

Enabling storage and utilization of low-carbon electricity: power to formic acid

Sudipta Chatterjee, †[ab] Indranil Dutta, †[ab] Yanwei Lum, [c] Zhiping Lai ★[ad] and Kuo-Wei Huang ★[ab]

Formic acid has been proposed as a hydrogen energy carrier because of its many desirable properties, such as low toxicity and flammability, and a high volumetric hydrogen storage capacity of 53 g H_2 L^{-1} under ambient conditions. Compared to liquid hydrogen, formic acid is thus more convenient and safer to store and transport. Converting formic acid to power has been demonstrated in direct formic acid fuel cells and in dehydrogenation reactions to supply hydrogen for polymer electrolyte membrane fuel cells. However, to enable a complete cycle for the storage and utilization of low-carbon or carbon-free electricity, processes for the hydrogenation and electrochemical reduction of carbon dioxide (CO_2) to formic acid, namely power to formic acid, are needed. In this review, representative homogenous and heterogeneous catalysts for CO_2 hydrogenation will be summarized. Apart from catalytic systems for CO_2 hydrogenation, a wide range of catalysts, electrodes, and reactor systems for the electrochemical CO_2 reduction reaction (eCO_2RR) will be discussed. An analysis for practical applications from the engineering viewpoint will be provided with concluding remarks and an outlook for future challenges and R&D directions.

Broader context

Development and transition into a low-carbon and renewable energy future is a must in order to mitigate the climate change associated with CO_2 emissions from our extensive fossil fuel-based energy use. A sustainable system needs to come along with viable energy storage and utilization processes. Besides batteries, storing low-carbon electricity as chemical fuels has been envisioned to play an essential role, in particular, to allow wide distribution of renewable energy and to decarbonize the transportation sector. In this context, formic acid offers several unique strengths, making it suitable for both short- and long-term applications.

1. Introduction

The global energy consumption rate in 2018 was estimated to be 19.0 TW (10^{12} watts) on average.[1,2] Approx. 80% of the energy supplies come from fossil fuels, in the forms of oil, coal, and gas, resulting in an annual carbon dioxide (CO_2) emission of 33.2 gigatonnes with approx. 25% contributed by the transport sector.[1] The associated increase of the atmospheric CO_2 concentration from preindustrial 280 to 415 ppm nowadays is highly related to climate issues such as global warming and extreme weather.[3] To mitigate climate change and to address the challenges facing the depleting fossil resources, low-carbon energy generation and distribution systems must be developed, and, accordingly, the transport sector needs to be decarbonized through electrification.[4–6] Complementary to batteries, hydrogen (H_2) is considered as a promising bridge between the power generation plants and end-user applications, because H_2 can be produced *via* electrolysis of water and efficiently converted back into electricity on demand by fuel cells.[7–9] However, viable options in H_2 delivery and storage have not reached a practical level due to the safety concerns and the huge energy loss in the H_2 liquefaction step and boil-off during transportation.[10,11] In this regard, formic acid (FA) has several specific advantageous properties as a hydrogen energy carrier with great potential to make a significant contribution.[12–16]

Formic acid is the common name of methanoic acid, having a chemical formula of HCOOH. It is a liquid under ambient conditions. Although FA contains only 4.34 wt% H_2, because of the high density (1.22 g cm^{-3}) of pure FA (Table 1),[17] its volumetric capacity reaches 53 g H_2 L^{-1} (or 1.77 kW h L^{-1}), equivalent to ~ 650 bars of H_2. In addition to the low toxicity and flammability, FA is convenient to store and transport; thus,

[a] Division of Physical Science and Engineering, King Abdullah University of Science and Technology, Thuwal 23955-6900, Saudi Arabia.
E-mail: zhiping.lai@kaust.edu.sa, hkw@kaust.edu.sa

[b] KAUST Catalysis Centre, King Abdullah University of Science and Technology, Thuwal 23955-6900, Saudi Arabia

[c] Institute of Materials Research and Engineering, 2 Fusionopolis Way, 138634, Singapore

[d] Advanced Membranes and Porous Materials Center, King Abdullah University of Science and Technology, Thuwal, Saudi Arabia

† These authors contributed equally.

1194 | *Energy Environ. Sci.*, 2021, **14**, 1194–1246

This journal is © The Royal Society of Chemistry 2021

FA could be suitable for automotive and back-up power applications.[12] Indeed, the potential utilization of FA as a secondary fuel has been examined in direct formic acid fuel cells (DFAFCs),[18] although the long-term usage is still restricted by electrode poisoning issues. In contrast, the FA reforming strategy to supply H_2 for polymer electrolyte membrane fuel cells (PEMFCs) appears to be a promising option, taking advantage of PEMFCs as a mature technology. Significant progress in the catalyst development for the selective dehydrogenation of FA was witnessed in the last two decades.[14–16,19] The FA to power concept has been successfully demonstrated by a number of groups in FA-based electricity generation devices.[20,21] One potential drawback of FA is its corrosiveness, but such situations can be managed by proper design of suitable containers and pipelines,[22,23] and thus the

Table 1 Properties of formic acid

Formic acid: CH_2O_2	
Molecular mass	46.03
Density (20 °C)	1.22 g cm^{-3}
Dielectric constant (20 °C)	57.9
Melting point	8.4 °C
Boiling point	100.8 °C
pK_a	3.75

existing gasoline infrastructure may be employed for FA distribution after minor modifications.

To realize the proposed carbon-neutral "formic acid economy",[24] it is of the utmost importance to advance and integrate the power-to-FA processes to complete the cycle for the storage and utilization of low carbon electricity (Fig. 1). It can be

Sudipta Chatterjee

Sudipta Chatterjee received his PhD degree in Inorganic Chemistry from Indian Association for the Cultivation of Science, India, in 2017. He then worked as a Postdoctoral Associate at Cornell University, USA, from 2017 to 2019. Since July 2019, he is working as a Postdoctoral Fellow at KAUST Catalysis Center, KAUST, Saudi Arabia. His research areas lie in the field of small molecule activation and reduction (O_2, H^+, CO_2) towards sustainable energy production and identification of vital intermediates using electrochemical, spectro-electrochemical and DFT studies towards understanding the structure–function correlations.

Indranil Dutta

Indranil Dutta received his MSc at the University of Hyderabad (India) in Inorganic Chemistry. He pursued his PhD degree on metal–metal and metal–ligand cooperation strategies for organic transformation at Indian Institute of Technology, Kanpur, India. Afterwards he moved to Osaka University, Japan, as a Postdoctoral Fellow before moving to KAUST, KSA. Currently, he has been working with Prof. Kuo-Wei Huang since 2019. His broad research interests include the design of various cooperative catalysts and study of their reactivity towards small molecule activation and in particular for dehydrogenation chemistry. His present work focuses on formic acid dehydrogenation and CO_2 utilization.
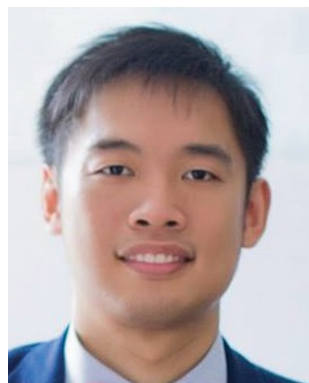
Yanwei Lum

Yanwei Lum is a Research Scientist at the Agency for Science, Technology and Research (A*STAR) in Singapore. He received his BEng from Imperial College London and PhD from University of California, Berkeley. Before joining A*STAR he was a PostDoctoral Fellow at the University of Toronto. His research interests include electrochemistry, materials chemistry, CO_2 conversion to chemicals/fuels and partial oxidation of hydrocarbon feedstocks.

Zhiping Lai

Zhiping Lai is Professor of Chemical Engineering at King Abdullah University of Science and Technology. He received his BE and MS from Tsinghua University China and PhD from the University of Massachusetts Amherst. Before joining KAUST, he was a research associate at the University of Minnesota Twin Cities and an Assistant Professor at Nanyang Technological University. His research focuses on developing high-performance membranes out of ordered porous materials and their applications in the separation of hydrocarbon mixtures, seawater desalination, lithium–sulfur batteries, and low-grade heat recovery. He is the recipient of the 2020 AIChE Industrial Gases Award.
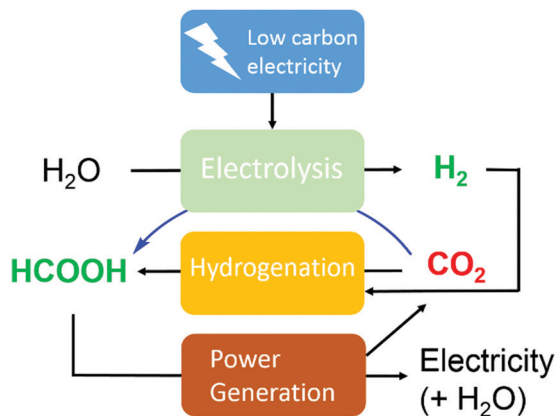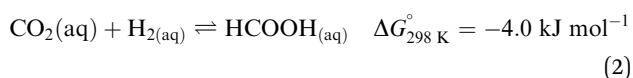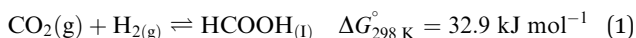
This journal is © The Royal Society of Chemistry 2021

Energy Environ. Sci., 2021, **14**, 1194–1246 | **1195**

Fig. 1 Storage and utilization of low carbon energy using formic acid.

envisioned that FA may be prepared by catalytic CO_2 hydrogenation using green H_2 from the electrolysis of water or by the electrochemical CO_2 reduction reaction (eCO_2RR). In this review, representative reactions in both processes will be summarized and discussed. It starts by covering the development of CO_2 hydrogenation using homogeneous, supported, and heterogeneous catalysts and the roles of the solvent and additives. This is then followed by reports of the eCO_2RR with comments on the catalysts, electrodes, and the design of systems. A techno-economic analysis for practical applications will be discussed. Finally, concluding remarks and an outlook for challenges and opportunities will be provided with suggestions on future R&D directions.

2. Hydrogenation of carbon dioxide

$$CO_2(g) + H_{2(g)} \rightleftharpoons HCOOH_{(l)} \quad \Delta G^{\circ}_{298\,K} = 32.9 \text{ kJ mol}^{-1} \quad (1)$$

$$CO_2(aq) + H_{2(aq)} \rightleftharpoons HCOOH_{(aq)} \quad \Delta G^{\circ}_{298\,K} = -4.0 \text{ kJ mol}^{-1} \quad (2)$$

Kuo-Wei Huang is Professor of Chemical Science at King Abdullah University of Science and Technology. He received his BS from National Taiwan University as a Yuan T. Lee Fellow and PhD from Stanford University as a Regina Casper Fellow. Before joining KAUST, he was an Assistant Professor at National University of Singapore and Goldhaber Distinguished Fellow at Brookhaven National Laboratory. The research interests of his group include CO_2 utilization, hydrogen storage, and small molecule activation by the $PN^3(P)$ platform his group has developed and pioneered. He was recently highlighted in the "Pioneers and Influencers in Organometallic Chemistry" series in Organometallics 2020.

Kuo-Wei Huang

The transformation of gaseous CO_2 to liquid FA is entropically disfavored due to a phase change (eqn (1)), but the thermodynamic preference is changed in the presence of aqueous medium (eqn (2)), although it may complicate the product separation. Continuous efforts have been made to scrutinize the reaction conditions to understand the influences of various catalysts, solvents, temperature, additives, *etc.* In order to shift the equilibrium from the reaction mixture of CO_2 and H_2 to the product, organic and inorganic bases are often used to give formate salts or other derivatives of FA as final products. A number of reviews have discussed the continuous progress and challenges of several homogeneous catalytic systems in last two decades or so.[25–31] Herein, the development will be summarized to compare the catalytic efficacies and to highlight the most efficient catalytic systems.

2.1. Homogeneous catalysis

2.1.1. Noble-metal-based catalysts. The first report in 1976 by Inoue and co-workers opened the field of homogeneous catalytic CO_2 hydrogenation to FA catalyzed by a series of phosphine based Ru, Rh, Pd, Ir, *etc.* complexes.[32,33] Using $Ru(H)_2(PPh_3)_4$ (**1**) in benzene/water (H_2O) containing trimethylamine (NEt_3) as a base, the best activity, a turnover number (TON) of 87 and a turnover frequency (TOF) of 4.5 h^{-1}, was achieved under 2.5 MPa CO_2 and 2.5 MPa H_2 at room temperature (RT). During the 1990s, Leitner *et al.* reported a catalytic system comprising [Rh(cod)Cl]$_2$/dppb (cod: 1,4-cyclooctadiene, dppb = 1,1-bis(diphenylphosphino)butane) (**2**) to yield a TON of 1150 in DMSO/NEt_3 at ambient temperature under 40 bar H_2/CO_2 (1 : 1).[34] A water soluble Rh complex, a Wilkinson-type catalyst [RhCl(mtppms)$_3$] (mtppms = monosulfonated triphenylphosphine) (**3**), was later reported for the hydrogenation in H_2O/dimethylamine with a TON of 3439.[35] The ligand effect was further investigated by keeping the solvent system intact. Combination of several mono- and bidentate phosphines/[Rh(cod)-(μ-Cl)$_2$] (**4**) resulted in the formation of FA with concentrations up to 2.58 M. It was concluded that chelating ligands were more active.[36] Importantly, while most hydrogenation reactions were studied in organic solvents, it was found that the presence of water may increase the catalytic aptitude. The Lau group demonstrated a significant rate enhancement using [TpRuH(PPh$_3$)-(CH$_3$CN)] [Tp = hydrotris(pyrazolyl)borate] (**5**) in the presence of water (Fig. 2).[37] The hydrogen bonding of a coordinated water molecule was found to facilitate the CO_2 insertion into the Ru–H bond.
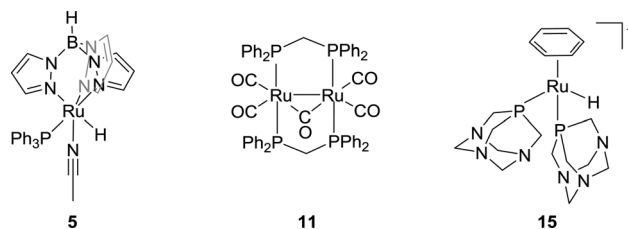

Fig. 2 Structures of selected ruthenium-based catalysts **5**, **11** and **15**.

Employment of super critical CO_2 (scCO$_2$) for hydrogenation was first introduced by the Noyori group. In the presence of NEt_3 and a trace amount of water, $RuCl_2(PMe_3)_4$ (6) and $Ru(H)_2(PMe_3)_4$ (7) gave high initial rates (TOF of 1400 h^{-1}), which were attributed to the enhanced miscibility of H_2 in scCO$_2$.[38] Using DMSO or MeOH instead of water led to an improved catalytic efficacy (TOF of 4000 h^{-1}), presumably due to the stabilization of catalytic intermediates by hydrogen bonding.[39] Fachinetti and co-workers also used the same catalytic system in neat NEt_3 using a biphasic medium.[40] The Jessop group reported a high TOF of 95 000 h^{-1} at 50 °C using $[RuCl(OAc)(PMe_3)_4]$ (8) and NEt_3 in pentafluorophenol under 190 bar H_2/CO_2.[41] *In situ* generated catalysts from $[RuCl_2(C_6H_6)]_2$ (9) and various phosphine ligands, such as PMe$_3$, PPhMe$_2$, bis(diphenylphosphino)-methane (dppm), 1,1-bis-(diphenylphosphino)ethane (dppe), and *cis*- or *trans*-Ph$_2$PCH=CHPPh$_2$, were examined in a MeOH/triisopropylamine (N^{i}Pr$_3$) solvent, and it was concluded that steric factors play the decisive role in comparison to electronic ones for monodentate phosphines.[42] For weakly basic diphosphines, smaller bite angles offered better activity, while, for more basic diphosphines, a reverse trend was observed.

In 1995, Chen and co-workers demonstrated that employment of *cis*-$[Ru(Cl_2bpy)_2(H_2O)_2][CF_3SO_3]_2$ (bpy = 2,2′-bipyridine) (10) in EtOH in the presence of NEt_3 resulted in TONs of up to 5000.[43] Puddephatt *et al.* reported a dinuclear ruthenium phosphine complex $[Ru_2(\mu\text{-}CO)\text{-}(CO)_4(\mu\text{-}dppm)_2]$ (11) for CO_2 hydrogenation in the presence of NEt_3 with a TON of 2160 (Fig. 2). 1.4 M FA was obtained under 38 bar H_2/CO_2 (1:1) and the FA concentration was doubled by doubling the total gas pressure.[44] The Joó group examined a number of rhodium and ruthenium based catalysts *viz.* $[RhCl(tppms)_3]$ (12), $[RuCl_2(mtppms)_2]_2$ (13), and $[RuCl_2(pta)_4]$ (14) (tppms = *meta*-trisulfonated triphenylphosphine, PTA = 1,3,5-triaza-7-phosphaadamantane) in aqueous medium without amine additives.[45–49] A maximum TOF of 9600 h^{-1} was achieved using complex 13 at 80 °C in a 0.3 M sodium bicarbonate solution. Catalyst 12 was found to hydrogenate the aqueous solution of CaCO$_3$ (0.1 M) to FA/formate under 100 bar H_2/CO_2 (4:1). These

findings inspired several groups to use aqueous medium for homogeneous CO_2 and bicarbonate hydrogenation. Subsequently, Kathó and co-workers reported the hydrogenation of 0.1 M HCO$_3^-$ solution under 10 MPa H_2 using $[(C_6H_6)RuH(pta)_2]^+$ (15) and proposed a mechanism involving hydride transfer to the bicarbonate moiety (Fig. 2).[50] The Beller group reported that the incorporation of various phosphine ligands into precatalyst 9 resulted in improved reactivity. When dppm was used as a ligand, a high TOF of 1260 h^{-1} was obtained. However, the catalytic activity was lost after the first few hours.[51]

In 2004, Himeda and co-workers employed hydroxy functionalized proton-responsive bipyridine (bpy)/phenanthroline (phen)-type ligands to develop a number of new catalysts.[52–55] Such proton responsive units allow the electronic properties to be controlled upon changing the pH values of the reaction medium. Under alkaline conditions, deprotonation of the hydroxyl group afforded the corresponding oxyanions as efficient hydrogenation catalysts. Initially, Ru(II), Rh(III) and Ir(III) complexes containing a 4,7-dihydroxy-1,10-phenanthroline (dhphen) ligand skeleton (16–18) were tested towards hydrogenation of bicarbonate solutions (Fig. 3). $[Cp*Ir(dhphen)Cl]Cl$ (17) (Cp* = 1,2,3,4,5-pentamethyl-cyclopentadienyl) showed the best performance with a TON of 21 000 (formate concentration of 0.42 M) and a TOF of 23 000 h^{-1} under basic conditions at 120 °C. Interestingly, an improved TOF of 33 000 h^{-1} was achieved with decreasing the catalyst concentration under otherwise similar conditions. The Ru analog 16 displayed an almost 3-fold-increase in the final formate concentration (1.2 M), albeit with a decreased TOF of 3360 h^{-1} at 120 °C. In the presence of an unsubstituted 1,10-phenanthroline ligand, both Ir and Rh complexes 19 and 20 did not show any reactivity (Fig. 3). These findings indicated the importance of oxyanionic species formation, presumably to enhance the solubility. The strong electron-donating of the oxyanion, generated from $[Cp*Ir(4dhbp)Cl]Cl$ (21) (4dhbp = 4,4′-dihydroxy-2,2′-bipyridine), imparted higher catalytic efficiency and was found 1000 times more reactive with a TOF of 5100 h^{-1} than the unsubstituted $[Cp*Ir(bpy)Cl]Cl$ (22) with a TOF of 4.7 h^{-1} at 80 °C under 1 MPa H_2/CO_2 (1:1) (Fig. 3). Himeda, Fujita and co-workers further

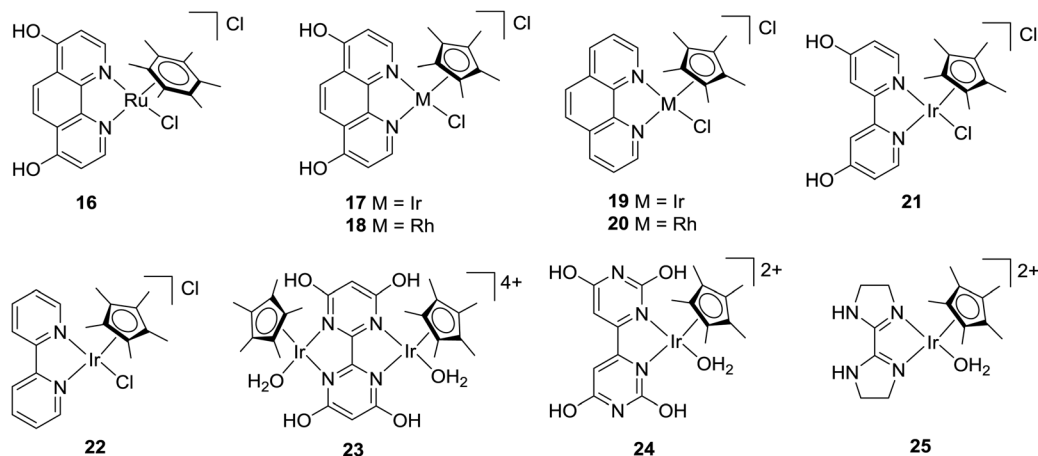

Fig. 3 Catalysts for CO_2 hydrogenation in basic aqueous media.

designed a binuclear Ir complex (23) having a bipyrimidine ligand with four hydroxyl groups for bicarbonate (2 M $KHCO_3$) hydrogenation (Fig. 3).[56] Under 50 bar H_2, formate salt was formed with a TOF of 53 800 h^{-1} and a TON of 79 000 at 80 °C. Similar activity was observed using the corresponding monomer analog (24), suggesting that bimetallic cooperativity may not be the crucial factor (Fig. 3). Interestingly, Ir complex 25 bearing a non-functionalized imidazoline moiety also showed similarly good activity (Fig. 3).[57] The importance of the pendant base effect was proposed to enhance proton transfer through a water bridge in stabilizing the transition state involving the rate-determining H_2 heterolysis step.

The Fukuzumi group reported a proton-responsive catalyst $[Cp*Ir(N1)(OH_2)]^+$ (26) for the efficient production of formate in 2.0 M $KHCO_3$ aqueous solution (pH 8.8) with a TON of 100 (20 h) and a TOF of 6.8 h^{-1} at ambient temperature and pressure (Fig. 4).[58] Himeda et al. also reported an Ir complex (27) bearing pyrimidine and imidazole groups with enhanced reactivity (TOFs ranging from 440 h^{-1} at 50 °C to 6440 h^{-1} at 120 °C) under 10 bar H_2/CO_2 (1:1) in basic media (Fig. 4).[59] Thiel and co-workers studied a series of Ru(II) complexes $[(N-N')RuCl(PMe_3)_3]$ (28a–j) ($N-N'$ = pyridinylazolato) with variable electronic properties to probe the structure–activity relationships for CO_2 hydrogenation and a maximum TON of 4800 was achieved (Fig. 4).[60] Ru catalysts having simple phosphite ligands, such as $P(OMe)_3$, $P(OEt)_3$, $P(O^iPr)_3$, and $P(OPh)_3$, showed good reactivities under the $scCO_2$ condition with DBU (1,8-diazabicyclo[5.4.0]undec-7-ene) and the highest TON of 6630 was obtained with $P(OMe)_3$.[60]

Several Ir and Ru complexes containing N-heterocyclic carbene (NHC) ligands were studied by the Peris group using H_2 or ^iPrOH (isopropanol) as the hydrogen source for CO_2 reduction

to FA (Fig. 5).[61] The strong σ donating ability of NHC ligands was crucial for the thermal stability of these catalysts. Ir 29 gave a TON of 150 under 50 bar CO_2 in the presence of 0.5 M KOH at 110 °C in ^iPrOH (Fig. 5). Employing bis NHC based Ir complex 30, a TON of 1600 was achieved under 60 bar H_2/CO_2 (1:1) in a 2 M KOH solution at 80 °C (Fig. 5). On the other hand, analogous Ru 31 resulted in a significant improvement in the TON (23 000) even under a lower pressure (40 bar H_2/CO_2) but at an elevated temperature of 200 °C (Fig. 5). When the ligand was modified by incorporating sulfonate substituents into the carbon side chains, the corresponding more water-soluble complex 32 afforded a TON of 190 000 under 60 bar H_2/CO_2 (1:1) in a 1 M KOH solution at 200 °C (Fig. 5). However, under the transfer hydrogenation condition, the catalyst lifetime decreased significantly (TON = 2700).[62]

Himeda and co-workers have reported a variety of Cp*Ir complexes (33–36) bearing pyridine-pyrazole moieties for CO_2 hydrogenation to formate (Fig. 6).[63] The introduction of an OH group on the pyrazole ring led to improved catalytic efficiency. Using 36 under 1.0 MPa H_2/CO_2 (1:1) in 1.0 M aqueous $NaHCO_3$ solution at 50 °C, a maximum TON of 7850 was obtained after 48 h. Under alkaline conditions, the OH group was converted to an oxyanionic species via deprotonation which was more electron donating than the neutral OH group to offer improved reactivities. Very recently, they also prepared several Cp*Ir catalysts (e.g. 37–40) based on picolinamidate ligands with a concept of enhanced electron-donating ability of the ligand via the coordinated anionic nitrogen atom (Fig. 6).[64] The influence of the proton responsive OH group at the ortho- or para-position of the pyridine ring was investigated. Catalyst 38 having an anionic coordinating amide N atom and an OH group in the second coordination sphere showed the best reactivity towards CO_2 hydrogenation in basic aqueous solution under ambient conditions with a TOF of 198 h^{-1}. Interestingly, complex 37, devoid of any ortho-OH groups, exhibited better long-term efficiency with a TON of 14 700 after 348 h under ambient conditions.

A record high TON was achieved by the Nozaki group in 2009 using a PNP ([2,6-bis(di-isopropylphosphinomethyl)pyridine]) based Ir trihydride catalyst (41) in a 1 M aqueous KOH solution (Fig. 7).[65] A TOF of 150 000 h^{-1} at 200 °C under 50 bar H_2/CO_2 (1:1) and an unprecedented TON of 3 500 000 at 120 °C in a total period of 48 hours were obtained. High temperature, pressure, a strong base and a polar solvent were all necessary for these high reactivities to be realized. A plausible mechanism was proposed based on a combined computational and experimental study.
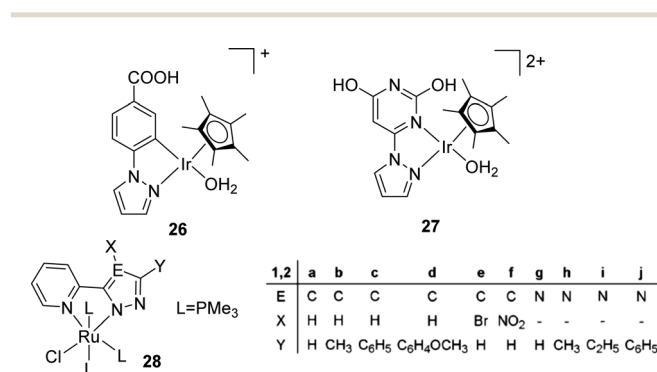

Fig. 4 Structures of selected Ir and Ru catalysts.

1,2	a	b	c	d	e	f	g	h	i	j
E	C	C	C	C	C	C	N	N	N	N
X	H	H	H	H	Br	NO_2	-	-	-	-
Y	H	CH_3	C_6H_5	$C_6H_4OCH_3$	H	H	H	CH_3	C_2H_5	C_6H_5
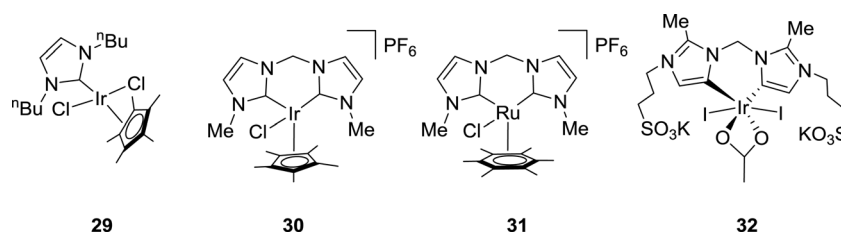
Fig. 5 Carbene-based catalysts 29–32.

1198 | Energy Environ. Sci., 2021, 14, 1194–1246

This journal is © The Royal Society of Chemistry 2021
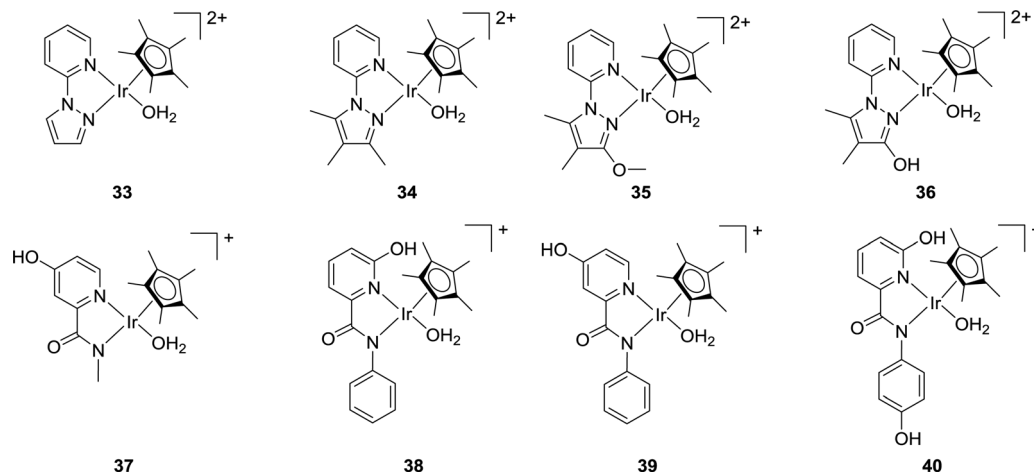
Fig. 6 Pyrazole and picolinamide derived catalysts **33–40**.

The insertion of CO_2 into an Ir–H bond from **41** to **42** first occurs, followed by the deprotonation of a CH_2 arm and the dearomatization of the central pyridine ring to give **43** with dissociation of formate as a rate determining step. The hydrogenation of **43** then regenerates **41** to complete the catalytic cycle (Fig. 7).[66]

Hazari and co-workers prepared an air-stable and water soluble saturated analog, $IrH_3(PNP)$ (**44**),[67] and showed that the presence of a strong electron-donating *trans* hydride ligand may weaken the Ir–H bond to facilitate the CO_2 insertion process to give a hydrogen bonded [Ir]-formate species (**45**; Fig. 8). An overall TON of 348 000 was achieved after 24 h at 185 °C under 56 bar H_2/CO_2 (1 : 1). DFT calculations were conducted to elucidate the mechanism. The influence of the H-bond donor was supported by comparing CO_2 insertion into the syn (H_a) and anti (H_b) hydrides with respect to the N–H bond (Fig. 8a). The H-bond assisted CO_2 insertion into H_a was found to be more favored over that into H_b, which was thermodynamically uphill.

Fig. 7 The proposed mechanism for CO_2 hydrogenation by **41**.

Overall, the CO_2 insertion into H_a or H_b resulted in an H-bound formate intermediate. The dissociation of the formate moiety and re-coordination then led to an O-bound species **45**. The formate in **45** can be replaced by H_2 to give the dihydrogen intermediate **46**. Deprotonation of the coordinated dihydrogen then regenerates the trihydride **44** (Fig. 8b). Experimental evidence and theoretical results suggested that nucleophilic attack of hydride on CO_2 is the rate-limiting step.

Pincer type Ru catalysts have also been employed for CO_2 hydrogenation. For example, the Sanford group demonstrated that the dearomatized Ru–PNN pincer complex (**47**) afforded a TON of 23 000 in the presence of K_2CO_3 under 40 bar H_2/CO_2 (3 : 1) at 120 °C in diglyme (Fig. 9).[68] When the amine donor group was replaced by a phosphine, the Pidko group showed that the pincer complex (**48**) gave a TOF of 1 100 000 h^{-1} and a TON of 37 000 under 40 bar H_2/CO_2 (3 : 1) at 120 °C using DMF (dimethylformamide) as the solvent and DBU as the base (Fig. 9).[69] Even lowering the overall pressure to 5 bars and the reaction temperature to 90 °C, a high TOF of 60 000 h^{-1} was achieved. Experimental evidence and DFT calculations suggested that a dihydrido Ru species (**49**) is the active catalyst (Fig. 9).[70,71] Szymczak and co-workers have also evaluated a series of Ru complexes (*e.g.* **50–52**) having an *N,N,N*-pincer ligand backbone and studied the effects of the steric bulk, ligand charges and bite angles on the catalytic activity (Fig. 9).[72] It was concluded that decreased ligand charge and the presence of *o*-substituents expedite the catalytic efficacy, whereas the bite angles have only small impacts. Under the optimized conditions, **51** was found to be the best with a TON of 60 000 after 18 h at 120 °C.

The Huang group has shown that replacing the CH_2 spacers in pyridine-based pincer complexes led to distinct kinetic and thermodynamic properties.[73,74] A new variety of PN^3P–Ru(II) pincer complex (**53**) was prepared for CO_2 hydrogenation in a 1 : 1 THF (tetrahydrofuran)/H_2O biphasic system (Fig. 10). Hydrogenation of $NaHCO_3$ solution was also realized with a TON of 33 000 after 50 h under 1600 psi H_2 at 130 °C.[75] A combination of direct CO_2 capture from air by various amines followed by hydrogenation was demonstrated with an efficiency
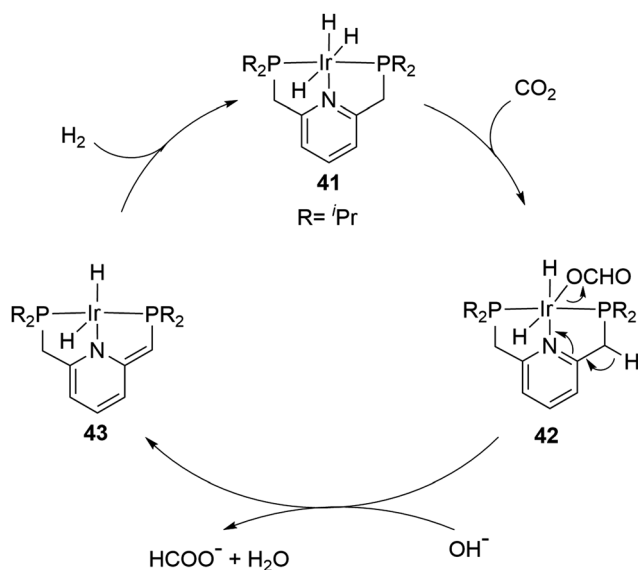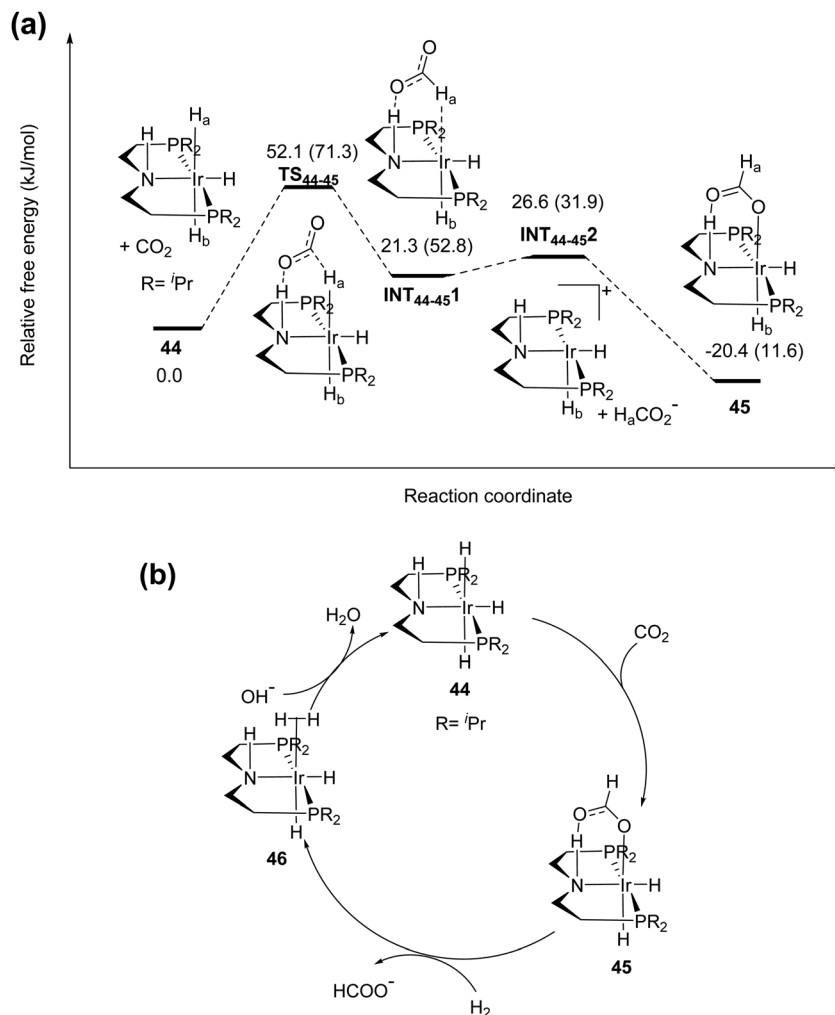
(a)

(b)

Fig. 8 (a) Pathway for insertion of CO_2 into **44**. Numbers in parentheses are for insertion into H_b. (b) The proposed mechanism for CO_2 hydrogenation by **44**.
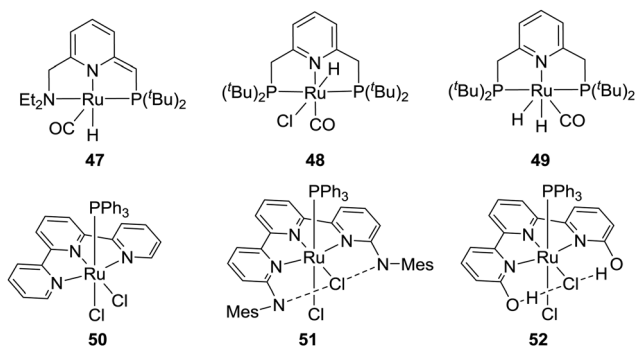

Fig. 9 Pincer type Ru catalysts **47–52**.

130 °C for direct CO_2 hydrogenation to formate (Fig. 10).[76] A possible catalyst deactivation pathway was suggested by the formation of a dearomatized PN³P*Ir(I)–CO species (**56**; Fig. 10).

Schaub and Paciello developed for the first time a scalable methodology based on an integrated CO_2 hydrogenation, catalyst recycling, and FA isolation process.[77] Reactions were performed in a biphasic diol/trihexylamine ($NHex_3$) medium using a homogeneous ruthenium catalyst, $Ru(H)_2(P^nBu_3)_4$ (**57**), leading to the formation of a $NHex_3$·FA salt. Upon completion, the product-rich phase was extracted with $NHex_3$, followed by separation by distillation, whereas the amine phase containing the catalyst was recycled for the next hydrogenation process.

of 39%. A biphasic 2-MeTHF/H_2O system using PMDTA (N,N,N',N'',N''-pentamethyldiethylenetriamine) as the CO_2 absorber was established for easy product separation and catalyst recycling. Interestingly, in contrast to Nozaki's results, PN³P–Ir pincer complexes (**54** and **55**) only gave a maximum TON of 5100 under 120 psi H_2/CO_2 (1:1) in 1:4 THF/H_2O at
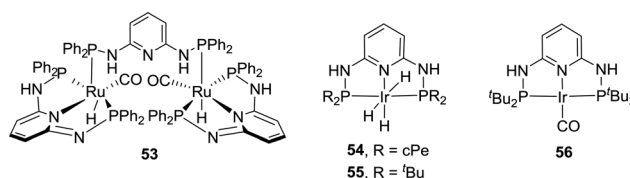
Fig. 10 Phosphorus-nitrogen PN³P–pincer complexes **53–56**.

1200 | *Energy Environ. Sci.*, 2021, **14**, 1194–1246

This journal is © The Royal Society of Chemistry 2021
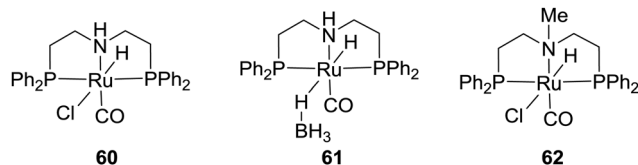
Fig. 11 Examples of commercial Takasago catalysts.

Pioneering work from He *et al.* led to the development of efficient CO_2 capture and subsequent hydrogenation.[78] PEI600 (polyethylenimine, M_w = 600) is stable and non-volatile, and it can absorb CO_2 with a capacity of 0.159 g of CO_2/0.3 g of amine in ethylene glycol. Heldebrant *et al.* reported the $RuCl_2(PPh_3)_3$ (**58**) catalyzed hydrogenation of captured CO_2 into methyl formate with a TON of up to 5100 after 40 h in a switchable ionic liquid (IL) comprising DBU and methanol at 140 °C.[79] Higher reaction temperatures and an excess of methanol promoted the esterification process and in turn led to methyl formate formation. Leitner and co-workers employed a suitable catalyst/IL matrices for the production of pure FA.[80] The catalyst precursors, $[Ru(cod)X_2]$ (**59**) (X_2 = acac (acetylacetonate), Cl_2, or (methylallyl)$_2$), were combined with tppms (monosulfonated triphenylphosphine)/PBu_4 (tetrabutylphosphonium) or EMIM (1-ethyl-3-methylimidazolium) in continuous-flow hydrogenation of scCO_2. They further developed biphasic systems for integrated CO_2 hydrogenation and facile product separation. $HNMe_2$, HN^iPr_2, and NEt_3 were used as amine

sources and the FA adduct was extracted into the aqueous phase, whereas the catalyst was immobilized in a hydrophobic solvent.

The commercial Takasago PN^{H}P-pincer Ru catalysts (**60** and **61**) and their methylated analog (**62**) were examined by the Prakash and Olah group for H_2 storage in organic solvent/H_2O in the presence of alkali hydroxides, carbonates, bicarbonates, and CO_2 (Fig. 11).[81] **60** and **61** could achieve formate formation with TOFs of 1688 and 958 h^{-1}, respectively, using $NaHCO_3$ in THF/H_2O at 80 °C under 40 bar H_2. Interestingly, the presence of the N–H group in the ligand backbone may not be necessary as **62** also showed a similar catalytic performance with a TOF of 1096 h^{-1} in a dioxane/H_2O solution of NaOH at 70 °C under 80 bar H_2/CO_2 (3:1). When integrated with CO_2 capture in the presence of amines, high activities were reached using tetramethylguanidine (TMG) and DABCO (1,4-diazabicyclo[2.2.2]octane) with up to 95% yield and a TON of 7375 in a dioxane/water medium under 50 bar H_2.[82] Similar results were also demonstrated by Prakash and co-workers using hydroxide bases (NaOH, KOH, and CsOH) for integrated CO_2 capture and subsequent conversion to formate salts.[83,84] Employment of a biphasic 2-MeTHF/water system allowed easy separation and reuse of the catalyst(s) over multiple cycles without a significant decrease in catalytic aptitude. Finally, Table 2 lists some of the noble-metal-based catalytic systems for CO_2 hydrogenation.

2.1.2. Non-noble-metal-based catalysts. Inoue *et al.* have previously noted low activities (TON = 7) of $[Ni(dppe)_2]$ (**63**) in CO_2 hydrogenation in 1976.[32,33] In 2003, Jessop and co-workers

Table 2 Overview of selected noble metal based catalytic systems

Catalyst precursor	Solvent	Base	H_2/CO_2 (bar)	Temp. (°C)	TON	TOF (h^{-1})	Ref.
$[RuH_2(PPh_3)_4]$ (**1**)	C_6H_6/H_2O	NEt_3	25/25	RT	87	4	33
$[Rh(cod)Cl]_2$/dppb (**2**)	DMSO	NEt_3	20/20	RT	1150	30–47	34
$[RhCl(mtppms)_3]$ (**3**)	H_2O	$NHMe_2$	20/20	RT	3439	290	35
$[TpRuH-(PPh_3)(CH_3CN)]$ (**5**)	CF_3CH_2OH	NEt_3	25/25	100	1815	110	37
$RuCl_2(PMe_3)_4$ (**6**)	scCO_2	NEt_3/H_2O	85/120	50	7200	1040	38
$RuH_2(PMe_3)_4$ (**7**)	scCO_2	NEt_3/H_2O	85/120	50	3700	1400	38
$RuH_2(PMe_3)_4$ (**7**)	scCO_2	NEt_3/DMSO	85/120	50	2000	4000	39
$[RuCl(OAc)(PMe_3)_4]$ (**8**)	scCO_2	NEt_3/C_6F_5OH	70/120	50	31 200	95 000	41 and 42
$[Ru(Cl)(bpy)_2(H_2O)][CF_3SO_3]_2$ (**10**)	EtOH	NEt_3	30/30	150	5000	625	43
$[Ru_2(\mu\text{-}CO)\text{-}(CO)_4(\mu\text{-}dppm)_2]$ (**11**)	Acetone	NEt_3	35/35	RT	2160	103	44
$[RuCl_2(mtppms)_2]_2$ (**13**)	H_2O	$NaHCO_3$	60/35	80	NA	9600	49
$[(C_6H_6)RuH(pta)_2]^+$ (**15**)	H_2O	$NaHCO_3$	100/0	80	NA	409	50
$[RuCl_2(C_6H_6)]_2$ (**9**)/dppm	H_2O	$NaHCO_3$	50/35	70	2520	1260	51
$[Cp^*Ir(dhphen)Cl]Cl$ (**17**)	H_2O	KOH	30/30	120	21 000	23 000	52
$[Cp^*Ir(4dhbp)Cl]Cl$ (**21**)	H_2O	KOH	5/5	80	11 000	5100	55
$[Cp^*Ir(4dhbp)Cl]Cl$ (21)	**H_2O**	**KOH**	**30/30**	**120**	**190 000**	**42 000**	**54**
$[(Cp^*Ir)_2(thbpm)(H_2O)_2](SO_4)_2$ (**23**)	H_2O	$KHCO_3$	50/0	80	79 000	53 800	56
$[Cp^*Ir(N1)(OH_2)]^+$ (**27**)	H_2O	$KHCO_3$	10/0	120	NA	6440	59
$IrH_3(PNP)$ (41)	**H_2O/THF**	**KOH**	**4/4**	**200**	**300 000**	**150 000**	**65 and 66**
$IrH_3(PNP)$ (41)	**H_2O/THF**	**KOH**	**4/4**	**120**	**3 500 000**	**73 000**	**65 and 66**
$IrH_3(PNP)$ (**44**)	H_2O	KOH	28/28	185	348 000	14 500	67
$Ru(PNN)CO(H)$ (**47**)	Diglyme	K_2CO_3	30/10	200	23 000	2200	68
$[Ru(H)(PNP)Cl(CO)]$ (48)	**DMF**	**DBU**	**30/10**	**120**	**200 000**	**1 100 000**	**69**
$[Ru(H)(PNP)Cl(CO)]$ (**48**)	DMF	DBU	2.5/2.5	90	NA	60 000	69
$[Ru(NNNN)(Cl)_2(PPh_3)]$ (**51**)	DMF	DBU	70/6	120	60 000	NA	72
$Ru(PN^3P)$ (**53**)	H_2O/THF	$NaHCO_3$	110/0	130	33 000	13 000	75
$IrH_3(PN^3P)$ (**55**)	H_2O/THF	KOH	4/4	130	5100	283	76
$[Cp^*Ir(N\text{–}N)(OH_2)]^{2+}$ (**36**)	H_2O	$NaHCO_3$	5/5	50	7850	650	63
$[Cp^*Ir(N\text{–}N)(OH_2)]^+$ (**37**)	H_2O	$NaHCO_3$	1/1	RT	14 700	NA	64
$[IrI_2(AcO)(bis\text{-}NHC)]$ (32)	**H_2O**	**KOH**	**30/30**	**200**	**190 000**	**2500**	**62**
$[Ru(H)(PNP)Cl(CO)]$ (**60**)	THF/H_2O	$NaHCO_3$	40/0	80	NA	1688	82
$[Ru(H)(PN^{Me}P)Cl(CO)]$ (**62**)	Dioxane/H_2O	NaOH	60/20	70	NA	1096	82

This journal is © The Royal Society of Chemistry 2021

Energy Environ. Sci., 2021, **14**, 1194–1246 | **1201**

showed that, with the right combination of metal and ligand, [NiCl$_2$(dcpe)] (**64**) (dcpe = bis(dicyclohexylphosphino)ethane) offered a TON of 4400 under 200 bar H$_2$/CO$_2$ (1:4) in a DMSO/DBU solution.[85] In 2010, the Beller group developed an iron based catalytic system for hydrogenation of a bicarbonate solution.[86] A system comprising Fe(BF$_4$)$_2$·6H$_2$O/tris[2-(diphenylphosphino)-ethyl]phosphine (**65**) gave the formate product with a TON of 610 under 60 bar H$_2$ in MeOH at 80 °C. Under similar reaction conditions, the analogous Co(BF$_4$)$_2$·6H$_2$O/tris[2-(diphenylphosphino)ethyl]phosphine (**66**) catalyst achieved a comparable activity with a TON of 645. Interestingly, improved activities, a TON of 3877 and a TOF of 190 h^{-1}, were realized at an elevated temperature of 120 °C.[87] Modifying the ligand system to tris[[2-(diphenylphosphino)phenyl]phosphine with Fe(BF$_4$)$_2$·6H$_2$O (**67**) afforded enhanced activity with a TON of 7500 at 100 °C.[87] Application of the same catalyst for CO$_2$ hydrogenation using 30 bar H$_2$/CO$_2$ (1:1) in a MeOH/NEt$_3$ solution yielded FA and methyl formate with a total TON of 1700. Improved formate selectivity was observed in the presence of water where formation of methyl formate was suppressed. Linehan *et al.* reported a Co(dmpe)$_2$H (dmpe: 1,2-bis(dimethylphosphino)-ethane) complex (**68**) for CO$_2$ hydrogenation in THF in the presence of a very strong base, Verkade's base (Fig. 12).[88] Under 1.8 and 20 atm of equimolar H$_2$/CO$_2$ pressure, high TOFs of 6400 and 74 000 h^{-1} were obtained, respectively, at room temperature. Initially, the metal hydride gets transferred to CO$_2$ to form [Co(dmpe)$_2$]$^+$ (**69**) and formate. Subsequently, addition of H$_2$ resulted in Co(III) dihydride intermediate **70**, which further underwent base mediated deprotonation to regenerate the Co(I) hydride (Fig. 12a). To further support the proposed mechanism of the hydride transfer step, detailed DFT calculations were carried out.[89] Two possible routes were considered: (I) direct hydride transfer from the metal complex to an encountered CO$_2$ (Fig. 12b) and (II) an associative pathway involving the binding of CO$_2$ through its carbon to the metal (Fig. 12c). For the direct hydride transfer process (Fig. 12b), electrostatic interactions between the Co–H moiety and CO$_2$ resulted in **Int$_{68}$1$_I$**. The free energy of activation for the hydride transfer **TS$_{68}$1$_I$** was calculated to be 17.2 kcal mol^{-1}. Subsequently, nucleophilic attack of the hydride to CO$_2$ resulted in an H-bound formate **Int$_{68}$2$_I$** species, which underwent an intramolecular rearrangement to generate an O-bound formate complex *via* transition state **TS$_{68}$2$_I$**. In the associative mechanism (Fig. 12c), the initial step is the endergonic formation of species **Int$_{68}$1$_{II}$**. This association proceeds with the binding of CO$_2$ to the Co, affording a six coordinated intermediate **Int$_{68}$2$_{II}$** *via* **TS$_{68}$1$_{II}$** with an energy barrier of 15.8 kcal mol^{-1}. In the following step, intramolecular hydride transfer occurs from the Co center to the electrophilic carbon of CO$_2$ to generate H-bound intermediate **Int$_{68}$3$_{II}$** through **TS$_{68}$2$_{II}$**. **Int$_{68}$3$_{II}$** has a similar relative energy and structure to those of **Int$_{68}$2$_I$** and can follow the same pathway to yield an O-bound formate complex. Overall, the associative pathway is favored by 1.4 kcal mol^{-1} over the direct hydride transfer and was proposed to be the preferred mechanism. It is evident that the rate determining step was the binding of CO$_2$ to Co and this was consistent with the fact that the rate increased
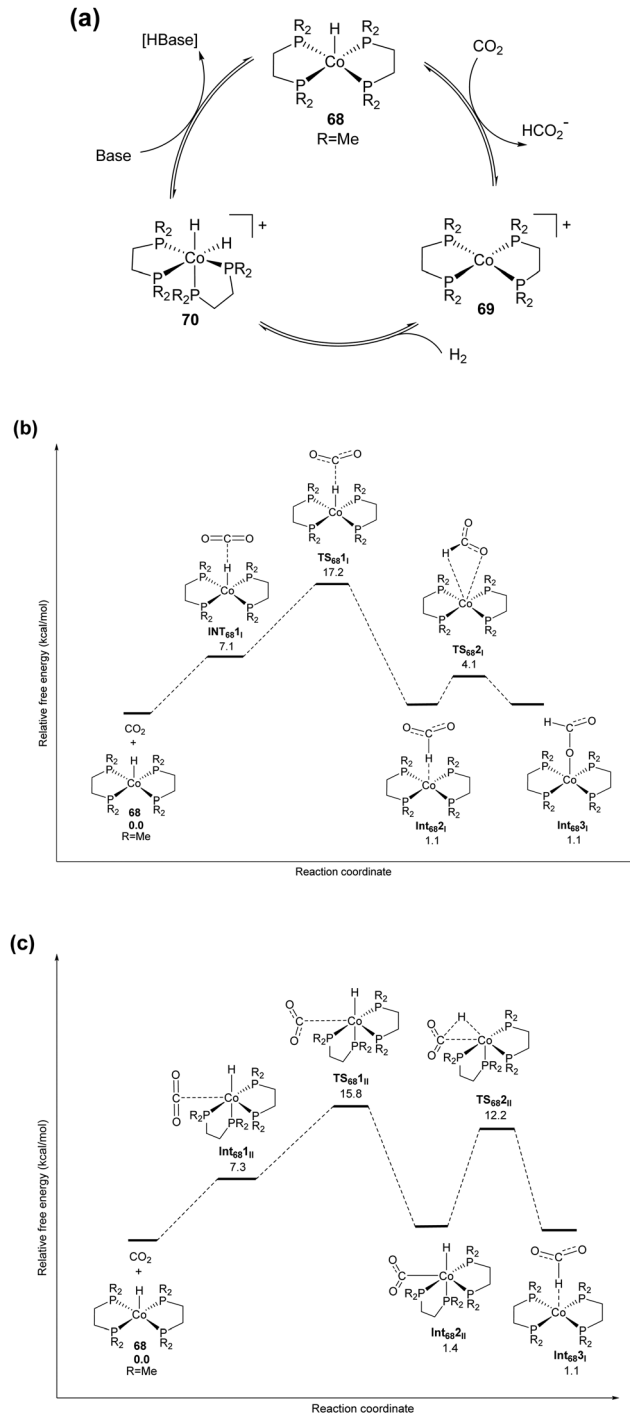

Fig. 12 (a) Proposed reaction mechanism for CO$_2$ hydrogenation using **68**. Free energy profiles of the (b) direct hydride transfer pathway and (c) associative pathway using **68**.

linearly with the CO$_2$ gas pressure while it was independent of both the hydrogen pressure and base concentration. Despite the decent activity, the main drawback was the necessity of Verkade's base to regenerate **68** from intermediate [Co(dmpe)$_2$(H)$_2$]$^+$ (**70**). The ratio of CO$_2$/H$_2$ was found to be crucial, as with increasing the ratio above 1, CO formation occurred due to the reverse water–gas shift (RWGS) reaction.[88]
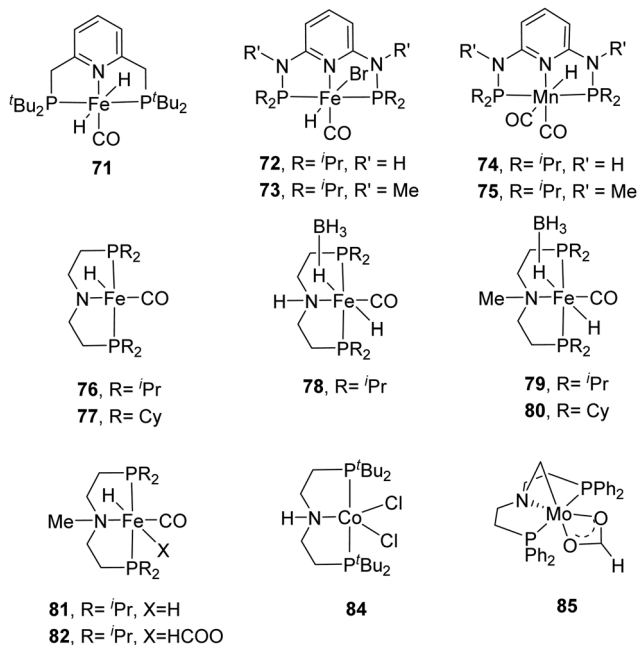
1202 | *Energy Environ. Sci.*, 2021, **14**, 1194–1246

This journal is © The Royal Society of Chemistry 2021

Fig. 13 Selected non-noble metal catalysts having a pincer backbone for CO_2 hydrogenation.

Milstein *et al.* employed a pyridine-based PNP–Fe pincer complex (**71**) for CO_2 and bicarbonate hydrogenation under low hydrogen pressures (Fig. 13).[90] Under 10 bar H_2/CO_2 (2:1), a maximum TON of 788 and a TOF of up to 160 h^{-1} were obtained. Subsequently, the Kirchner and Gonsalvi group demonstrated the activity of a set of iron PN^{3}P-pincer complexes having either N–H (**72**) or N–Me (**73**) arms towards CO_2 and bicarbonate hydrogenation under comparable reaction conditions (Fig. 13).[91] Employing **72** under 8.5 bar H_2 at 80 °C in a H_2O/THF (4:1) solvent, a TON of 140 was achieved for bicarbonate hydrogenation after 16 h. Using a higher H_2 pressure of 90 for 24 h yielded an improved TON of 4560. For CO_2 hydrogenation, a maximum TON of 10 275 was obtained using **73** in the presence of DBU in EtOH. The importance of

the protic solvent (H_2O) was realized as the reaction did not proceed in THF, presumably because the protic solvent helps to stabilize the catalytic intermediates *via* hydrogen bonding. The Mn(I) analogs **74** and **75** were also investigated by the same group (Fig. 13).[92] **74** displayed better activity compared to the Fe counterpart with a TON of 5520 under 80 bar H_2/CO_2 (1:1) in the presence of DBU in THF/H_2O at 80 °C. Employing LiOTf (lithium triflate) as an additive and lowering the catalyst loading to 0.002 mol% resulted in a larger TON of 30 000.

Hazari, Bernskoetter and co-workers studied a number of Fe(II) carbonyl hydride complexes bearing a saturated pincer ligand (**76–82**, Fig. 13).[93] Addition of a Lewis acid such as LiOTf was found to increase the reaction rates. The best results were obtained with TONs of 58 990 and 46 130 for **79** and **82**, respectively, after 24 h. Mechanistic insights suggested initial base promoted activation of **79** followed by rapid CO_2 insertion into the Fe–H bond leading to a metal coordinated formate species as a catalytic resting state (**82**) (Fig. 14). Lewis acid assisted substitution of the formate ligand by dihydrogen occurred to yield a transient cationic Fe(II)–H_2 complex (**83**; Fig. 14). Subsequent deprotonation of the dihydrogen fragment by DBU completes the catalytic cycle. In 2016, Bernskoetter *et al.* synthesized analogous Co and Mo catalysts (**84** and **85**) for CO_2 hydrogenation with LiOTf as the Lewis acid additive (Fig. 13). The highest TON of 29 000 was obtained for **84** in CH_3CN at 45 °C under 69 bar H_2/CO_2 (1:1) using DBU as the base after 16 h,[94] but poor reactivity (TON of 35) was observed for **85**.[95]

While Cp*Ir(III) complexes tethered to proton-responsive dihydroxybipyridine ligands were active catalysts for CO_2 hydrogenation,[52–55] Fujita *et al.* have shown that their Co(III) counterparts only offered limited catalytic aptitudes due to poor thermal stability.[96] However, the Khusnutdinova group demonstrated that with Mn complex **86** bearing 6,6′-dihydroxy-2,2′-bipyridine (Fig. 15), a TON of 6250 (98% yield) was obtained when the reaction was performed under 6 MPa H_2/CO_2 (1:1) in the presence of DBU in CH_3CN at 65 °C.[97] Employing Mn **87** yielded only a trace amount of formate under otherwise identical
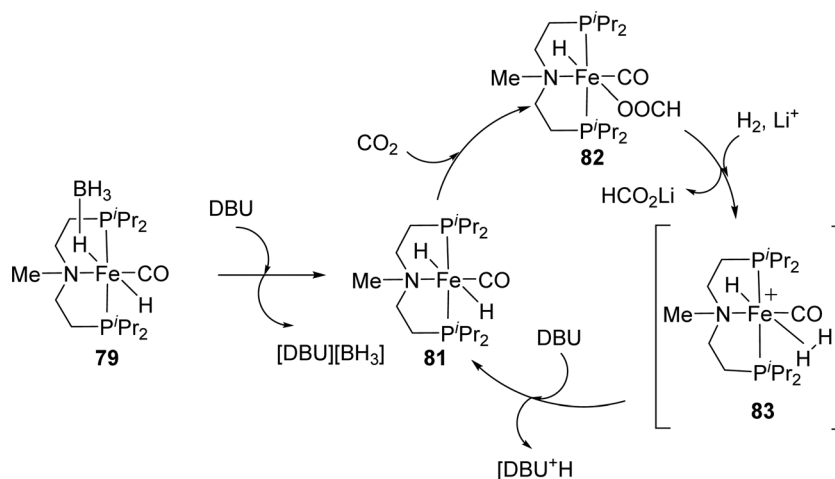

Fig. 14 Proposed reaction mechanism for CO_2 hydrogenation using **79**.
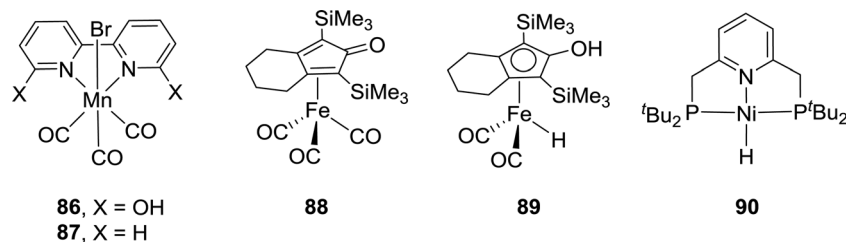
Fig. 15 Other selected non-noble metal catalysts.

reaction conditions, indicating the crucial role of the adjacent –OH group (Fig. 15).

In 2015, Yang, Zhou and co-workers examined Fe complex **88** for hydrogenation of bicarbonates and CO_2 to formates and identified the Knölker complex (**89**) as the active catalytic intermediate in this process (Fig. 15).[98] Using $NaHCO_3$, the optimized activity with a TON of 447 was achieved under 30 bar H_2 in EtOH/H_2O at 120 °C after 24 h. Employing 20 bar of CO_2 as the substrate in the presence of NaOH under similar reaction conditions resulted in only traces of formate, presumably because the formation of the Knölker complex was hindered. Enthaler and Junge et al. evaluated a pincer based Ni hydride catalyst (**90**) for the hydrogenation of $NaHCO_3$ (Fig. 15).[99] Under 55 bar H_2 in MeOH, the corresponding formate salt was formed at 150 °C with a TON of 3038. Interestingly, the Ikariya group demonstrated that simple Cu(II) salts, such as $Cu(OAc)_2 \cdot H_2O$, showed certain catalytic reactivity for CO_2 hydrogenation in the presence of DBU, albeit with limited performance.[100] Table 3 summarizes selective non-noble-metal-based catalytic systems for CO_2 hydrogenation.

2.1.3. Catalysis under base-free conditions. The reaction conditions for hydrogenation of CO_2 or bicarbonate to FA discussed above suggest that in general the majority of catalytic systems require the use of bases or basic additives to achieve acceptable efficiencies. These basic additives react with FA to generate formate salts or adducts to shift the thermodynamic equilibrium to the product side, and the base may also accelerate the H_2 heterolysis step and thus promote the catalytic activity. However, there are a few major drawbacks. The formate

derivatives reduce the overall gravimetric H_2 storage capacity. Moreover, during the reverse FA dehydrogenation process, possible base entrainment in the gaseous product will require additional treatments before fuel cell applications. As a result, additional neutralization and purification steps and energy are necessary to convert the formate products to FA. From atom-economic and industrial perspectives, the direct hydrogenation of CO_2 to FA in the absence of a stoichiometric base is thus an attractive goal. While the base free condition is desirable, there are only a limited number of examples in a homogeneous system. The first example was reported by Khan et al. in 1989.[101] An aqueous solution containing 0.01 M K[Ru(EDTA-H)Cl]·$2H_2O$ (**91**) (edta = ethylenediaminetetraacetate) catalyzed base free CO_2 hydrogenation under 17 bar H_2 and 3 bar CO_2 to generate FA and a small amount of formaldehyde at 40 °C with an FA formation rate of 62.5×10^{-3} M min^{-1}. However, the products slowly decomposed into H_2O and CO under the reaction conditions. Tsai and Nicholas demonstrated that [Rh(nbd)(PMe$_2$Ph)$_3$]BF$_4$ (**92**) (nbd = norbornadiene) achieved a maximum FA concentration of 0.18 M without a base additive under 96 bar of H_2/CO_2 (1 : 1) at 40 °C in wet THF for 48 h.[102] To justify the role of H_2O, it was concluded that hydrogen bonding between the H_2O molecules and CO_2 could stabilize the transition state for CO_2 insertion and in turn reduce the activation energy. In 1994, Leitner and co-workers used Ru catalyst **2** for CO_2 hydrogenation under 40 bar H_2/CO_2 (1 : 1) without a base to give a final FA concentration of 0.034 M with a TON of 6 and TOF of 0.9 h^{-1} at ambient temperature.[103] In 2004, the Fukuzumi

Table 3 Overview of selected non noble metal based catalytic systems

| Catalyst precursor	Solvent	Base	H_2/CO_2 (bar)	Temp. (°C)	TON	TOF (h^{-1})	Ref.
Ni(dppe)$_2$ (**63**)	C_6H_6	NEt$_3$/H_2O	25/25	RT	7	0.35	33
[NiCl$_2$(dcpe)] (**64**)	DMSO	DBU	160/40	50	4440	20	85
Fe(BF$_4$)$_2$·6H_2O/PP$_3$ (**65**)	MeOH	NaHCO$_3$	60/0	80	610	30	86
Co(BF$_4$)$_2$·6H_2O/PP$_3$ (**66**)	MeOH	NaHCO$_3$	60/0	120	3877	190	87
Fe(BF$_4$)$_2$·6H_2O/PP$_3$ (**67**)	MeOH	NaHCO$_3$	60/0	100	7500	750	87
Co(dmpe)$_2$H (**68**)	THF	Verkade's base	10/10	21	9400	74 000	88
[Fe(H)$_2$(PNP)(CO)] (**71**)	THF/H_2O	NaOH	6.7/3.3	80	788	160	90
[Fe(H)(PNP)(CO)Br] (**72**)	NaHCO$_3$	NEt$_3$/C_6F_5OH	90/0	80	4560	NA	91
[Fe(H)(PNP)(CO)Br] (**73**)	EtOH	DBU	4.25/4.25	80	10 275	NA	91
[Mn(H)(PNP)(CO)$_2$] (**74**)	THF/H_2O	DBU	40/40	80	5520	NA	92
[Mn(H)(PNP)(CO)$_2$] (**74**)	THF/H_2O	DBU/LiOTf	40/40	80	30 000	NA	92
[Fe(PNP)(H)(BH$_4$)(CO)] (79)	**THF**	**DBU/LiOTf**	**35/35**	**80**	**58 990**	**NA**	93
[Fe(PNP)(H)(OOCH)(CO)] (82)	**THF**	**DBU/LiOTf**	**35/35**	**80**	**46 100**	**23 200**	93
[Co(PNP)(CO)$_2$]Cl (**84**)	CH$_3$CN	DBU/LiOTf	35/35	45	29 000	5700	94
[Mn(bpy(OH)$_2$)(CO)$_3$(Br)] (**86**)	CH$_3$CN	DBU	30/30	65	6250	238	54
[(PCP)Ni(H)] (**90**)	MeOH	NaHCO$_3$	55/0	150	3038	150	99
Cu(OAc)$_2$·H_2O	Dioxane	DBU	20/20	100	167	NA	100
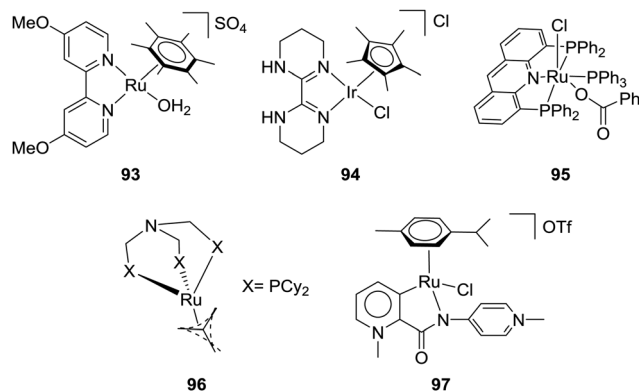
Fig. 16 Structures of catalysts for base-free CO_2 hydrogenation.

group employed a water soluble ruthenium catalyst, $[(C_6Me_6)Ru(4,4'-dmbpy)(OH_2)]SO_4$ (dmbpy = dimethoxy-2,2'-bipyridine) (**93**), to obtain a TON of approx. 55 under 25 bar CO_2/55 bar H_2 in H_2O at 40 °C (Fig. 16).[104] Laurenczy et al. achieved a better FA concentration of 0.2 M using Ru catalyst **15** in H_2O under 200 bar H_2/CO_2 (3:1) at 60 °C with a TON of 74.[105] The reactivities in common organic solvents, e.g. CH_3CN, toluene, MeOH, EtOH, and propylene carbonate, were comparable, whereas DMSO gave significantly improved efficiency with a TON of 750, corresponding to 1.9 M FA. Further studies suggested a stronger hydrogen-bonding network in the FA/DMSO system compared to that in FA/H_2O mixtures to be the decisive factor for the enhanced CO_2 hydrogenation activity.[106] The catalyst was recycled in DMSO and in H_2O without loss of catalytic activity. In 2016, Li and co-workers reported an iridium catalyst (**94**) for hydrogenation of CO_2 to FA in aqueous medium in the absence of any additives (Fig. 16).[107] Under 50 bar H_2/CO_2 (1:1), a TOF of 13 000 h^{-1} during the first 5 min was observed to yield a 0.005 M FA solution at 80 °C. With an increased pressure of 76 bar H_2/CO_2 at 40 °C, a 0.117 M FA solution with a TON of over 10 000 was achieved.

The Leitner group demonstrated that $[Ru(acriphos)(PPh_3)(Cl)(PhCO_2)]$ (acriphos: 4,5-bis(diphenylphosphino)acridine) (**95**) catalyzed CO_2 hydrogenation to FA under 80 bar H_2/CO_2 (1:1) to afford a TON of 1094 (0.09 M FA) in DMSO at 60 °C after 16 h (Fig. 16).[108] Interestingly, the solvent mixture of 95% DMSO/5% H_2O (v/v) enhanced the TON to 4200 (0.33 M FA) under otherwise identical conditions. This particular water concentration was

crucial as either a lower or higher concentration had a detrimental effect on the yields. DFT calculations revealed the advantageous effect of the water molecule, suggesting thermodynamic stabilization of FA. Model CO_2 hydrogenation was repeated in the presence of an acetate buffer (CH_3COOH/CH_3COONa 1:1, pH 4.75) to achieve an almost 4-fold enhanced FA concentration of 1.27 M with a TON of 16 310. Klankermayer and co-workers recently disclosed that $[Ru(N\text{-}triphosCy)(tmm)]$ (tmm = trimethylmethane) (**96**) bearing sterically demanding cyclohexyl groups catalyzed CO_2 hydrogenation in the presence of $Al(OTf)_3$ as the Lewis acid additive (Fig. 16).[109] Under 120 bar H_2/CO_2 (3:1) in MeOH/dioxane at 60 °C, FA was formed and subsequently converted to methyl formate with a maximum TON of 9542.

Ionic liquids (ILs) with basic anions are beneficial for efficient CO_2 hydrogenation under base-free conditions.[110] Albrecht et al. have recently reported Ru catalyst **97** and employed an imidazolium-based IL (BMMI·OAc = 1-butyl-2,3-dimethylimidazolium acetate) as the buffering media for CO_2 hydrogenation (Fig. 16).[111] The pH may be stabilized by the IL to prevent catalyst deactivation, and, at the same time, the acetate counteranion may bring the selectivity towards FA synthesis. A TON of 4520 was achieved under 60 bar H_2/CO_2 (1:1) in DMSO/water (5 v/v% water) at 70 °C after 72 h. Table 4 summarizes selective catalytic systems that can perform CO_2 hydrogenation under base-free conditions.

2.2. Heterogeneous catalysis

The discussions in Section 2.1 clearly indicate that excellent TONs and TOFs could be achieved using homogeneous catalysts. However, the foremost challenge of employing homogeneous systems for scale-up production is catalyst and product separation.[40] Moreover, as a catalyst promotes reactions from both sides, decomposition of the generated formate/FA back into CO_2 and H_2 may occur during the catalyst and product separation step(s).[77,105,112] Heterogeneous catalysts thus have strong merit for product separation and continuous operation, but they are comparatively less investigated. In this section, the development will be summarized to compare their catalytic efficacies and highlight the most efficient catalytic systems.

2.2.1. Bulk metal catalysts. Bulk metals were the simplest materials examined for CO_2 hydrogenation.[113,114] As early as 1914, Bredig and Carter already tested the activities of metal Pd black under relatively mild conditions, e.g. 70–95 °C, 0–30 bar

Table 4 Overview of selected catalysts that perform under base free conditions

Catalyst precursor	Solvent	H_2/CO_2 (bar)	Temp. (°C)	TON	TOF (h^{-1})	Ref.
K[Ru(edta-H)Cl]·2H_2O ((**91**))	H_2O	3/17	40	NA	120	101
[Rh(nbd)(PMe$_2$Ph)$_3$]BF$_4$ ((**92**))	THF/H_2O	48/48	40	130	3	34
[Rh(cod)Cl]$_2$/dppb (**2**)	DMSO	20/20	RT	6	0.9	86
$[(C_6Me_6)Ru(4,4'-dmbpy)(OH_2)]SO_4$ (**93**)	H_2O	55/25	40	55	NA	104
$[RuCl_2(pta)_4]$ (**15**)	DMSO	50/50	60	750	NA	87
$[Cp*Ir(N–N)Cl]Cl$ (**94**)	H_2O	25/25	80	1100	13 000	107
$[Ru(acriphos)(PPh_3)(Cl)(PhCO_2)]$ (**95**)	DMSO/H_2O	40/40	60	4200	260	108
$[Ru(N\text{-}triphosCy)(tmm)]$ (**96**)	MeOH/dioxane	90/30	60	9542	NA	109
$[Ru(C–N)(p\text{-}cymene)(Cl)](OTf)$ (**97**)	DMSO/H_2O	30/30	70	4520	117	111

This journal is © The Royal Society of Chemistry 2021

Energy Environ. Sci., 2021, **14**, 1194–1246 | **1205**

CO_2/bicarbonates, 30–60 bar H_2.[113] The Wrighton group reported a TON of 2.1 when 1 M aqueous $NaHCO_3$ solution was hydrogenated under static 1.7 atm H_2 by Pd black.[115] Takahashi and co-workers examined a mixture of Fe and Ni powders and H_2O as a hydrogen source.[116] Under hydrothermal conditions at 300 °C in the presence of K_2CO_3, formate was formed in 2.5% yield based on Fe. Various group 8–11 metal blacks, including RANEY® Ni, Co, Cu, Ru, Rh, Pd, Ag, Ir, Pt, and Au, were examined by Fachinetti et al.,[117] and only Au metal blacks exhibited some activity. However, aggregation of catalytic metal particles led to a decrease in active catalytic surface sites and catalyst deactivation. Upadhyay and Srivastava synthesized Ru nanoparticles in various sizes ranging from 17.1 to 22.6 nm in situ in a series of functionalized DAMI (1,3-di(N,N-dimethyl-lamino ethyl)-2-methyl imidazolium) ILs to achieve quite impressive catalytic performance with TONs as high as 24 000 and TOFs up to 9900 h^{-1} under 50 bar H_2/CO_2 (1:1) at 50 °C.[118] The Umegaki group also explored Ru nanoparticles, generated in MeOH under solvothermal conditions, for hydrogenation of scCO_2. In the presence of NEt_3 and H_2O as promoters, a high TON of 6351 was obtained after 3 h at 80 °C under 13 MPa H_2/CO_2 (5/8).[119] Huo, Jin, Chen et al. later investigated nano-porous Ni (NiNPore) catalysts for hydrogenation of $NaHCO_3$ to FA in aqueous medium.[120] A TON of 3476 was obtained under 6 MPa H_2 at 150–200 °C. Recently, Liu and co-workers have observed some activity on Pd/C in base-free CO_2 hydrogenation in [Bmim][OAc] (1-butyl-3-methylimidazolium acetate) with a maximum TON of 594.[121]

2.2.2. Supported metal catalysts. For heterogeneous catalysis, a reaction in general proceeds through the following steps: (1) adsorption of reactants onto the catalyst surface, (2) the adsorbed substrates undergo reactions catalyzed by the active sites, and (3) desorption of products from the catalyst surface. The number of metal atoms present on the surface of the bulk metal is significantly smaller than that present in the interior, thus offering limited active sites. Furthermore, under the reaction conditions, these bulk metals often aggregate and the number of active metal atoms on the catalyst surface can be further reduced. Employing support materials is a common strategy to minimize aggregation issues, and these materials may create unique active sites at the perimeter of the active metal and alter the electronic properties. The Wrighton group has studied the effect of active metals and supports, and Pd/C was identified to give improved reactivity with a TON of 115.[115] Fachinetti and co-workers also found that by employing a dispersed Au catalyst on TiO_2 (1 wt% Au/TiO_2) the catalytic performance was enhanced with a TON of 855 under otherwise similar conditions.[117] The catalyst also exhibited excellent stability as 1.3 kg of the FA–NEt_3 adduct with an acid/amine molar ratio of 1.7 was formed after continuing the reaction for 37 days.[122] Despite the stability of the supported Au particles, the reaction rate decreased as this catalyst also promoted the water gas shift reaction leading to CO accumulation (63 mmol).

The Pidko group compared several unsupported and supported Au nanoparticles (NPs) towards CO_2 hydrogenation, and, again, a higher efficiency per unit mass of Au was observed
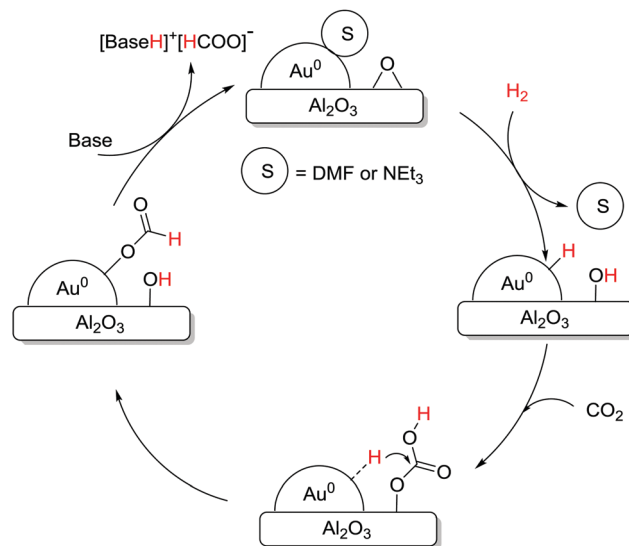

Fig. 17 Mechanistic pathway of CO_2 hydrogenation over supported Au nanoparticles.

with the supported system under 40 bar equimolar pressure in EtOH using NEt_3 at 40 °C.[123] A variety of supports, e.g. Al_2O_3, TiO_2, CeO_2, ZnO, MgCr-HT, MgAl-HT (hydrotalcite), and $CuCr_2O_4$, were screened and Au NP/Al_2O_3 displayed the best reactivity with a TON of 215, presumably due to the cooperative effect between Au^0 NPs and the basic Al_2O_3. Kinetic modelling and temperature dependent TOF studies suggested that Au NP/Al_2O_3 had a near-zero apparent activation energy (1.2 kcal mol^{-1}). A plausible mechanism according to spectroscopic analysis suggests initial heterolytic dissociation of H_2 at the Au/support interface to induce the formation of surface hydroxyl and Au–H species (Fig. 17). CO_2 is then adsorbed on the surface to form the surface bicarbonate intermediate, which further reacts with Au–H to afford an Au–formate intermediate. This species subsequently migrates to the thermodynamically more stable alumina surface and the successive elimination of formate closes the catalytic cycle.

Liu, Wang, Huang and co-workers used a Schiff-base-modified Au nanocatalyst supported on SiO_2 towards CO_2 hydrogenation. Very high activity with a maximum TON of 14 470 was achieved over 12 h in H_2O/MeOH at 90 °C.[124] HAADF-STEM (high-angle annular dark-field scanning transmission electron microscopy) analysis confirmed that the gold species existed primarily as sub-nanoclusters with sizes of 1.4 nm along with single atoms of a lower fraction. Computational investigations were conducted to evaluate plausible catalytic pathways (Fig. 18a). The activated H species were generated via dissociation of H_2 with a barrier of 0.67 eV (**TS-1**) and a weak exothermic contribution (∼0.10 eV). In the subsequent step, the CO_2 molecule is captured as a zwitterion intermediate on the interface of the gold nanocluster and Schiff base, which is further hydrogenated to an HCO_2 intermediate by activated H through **TS-2** with a barrier of 1.00 eV as the rate-limiting step. The HCO_2 moiety is then readily hydrogenated to cis-HCOOH by another surface H species via **TS-3** with an
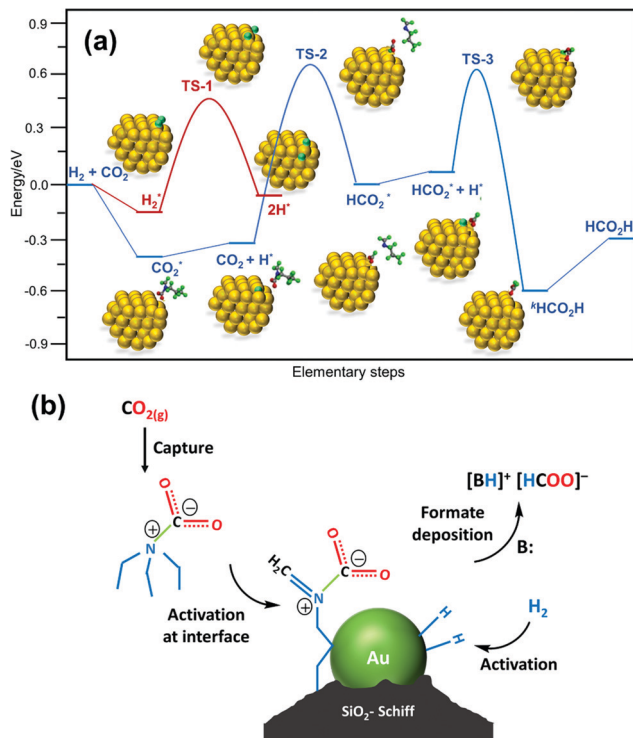
1206 | Energy Environ. Sci., 2021, **14**, 1194–1246

This journal is © The Royal Society of Chemistry 2021

Fig. 18 (a) Free energy diagram for CO_2 hydrogenation over the Au/SiO$_2$–Schiff catalyst. The energy profile was constructed based on the DFT calculation analysis of each elementary step. (b) Proposed synergistic mechanism for the hydrogenation of CO_2 to formate in the presence of carbamate over the Au/SiO$_2$–Schiff catalyst.[124]

energy barrier of 0.58 eV, which is subsequently released from the catalyst surface leading to the product. Based on computational analysis and a kinetic study, a mechanism was proposed (Fig. 18b). In the initial step, CO_2 activation is achieved through a weakly bonded carbamate zwitterion intermediate at the gold–Schiff base interface. Simultaneously, H_2 dissociation is promoted by the low-coordinated sites of the gold nanoclusters to generate the activated hydride species. Finally, the carbamate zwitterion intermediates are hydrogenated by the hydride species at the gold–Schiff base interface, and product formate is thus formed after two-step hydrogenation and acid–base neutralization in basic medium.

In 2015, Lin et al. found that the hydrogenation of carbonates (Na$_2$CO$_3$, K$_2$CO$_3$ and (NH$_4$)$_2$CO$_3$) was sluggish compared to that of bicarbonates (NaHCO$_3$, KHCO$_3$ and NH$_4$HCO$_3$).[125] Using porous carbon material (activated carbon, AC) supported Pd as the catalyst, a higher yield of 42.4% with a TON of 782 was observed for NH$_4$HCO$_3$, compared to NaHCO$_3$ and KHCO$_3$ under 2.75 MPa H_2 at ambient temperature. Controlled studies suggested that even using CO_2, HCO$_3^-$ was the actual substrate in the catalytic cycle. Thus, the trend of the observed reactivity was rationalized by the higher equilibrium concentration of HCO$_3^-$ ions (0.92 M) over CO$_3^{2-}$ ions for NH$_4$HCO$_3$ than that of NaHCO$_3$ (0.61 M) or KHCO$_3$ (0.89 M). However, increasing the temperature had a detrimental effect owing to the Pd/AC promoted decomposition of NH$_4$HCO$_3$ back into CO_2, H_2 and NH$_3$. Cao and

co-workers evaluated the catalytic performance of Pd NPs supported on reduced graphite oxide nanosheets (Pd/r-GO) for reversible (de)hydrogenation between KHCO$_3$ and HCOOK.[126] The highest TON of 7088 was observed using 1 wt% Pd/r-GO under 4 MPa H_2 at 100 °C after 32 h. However, upon increasing the catalyst loading, the catalytic efficiency gradually decreased due to the larger lattice strain of Pd NPs in 1 wt% Pd/r-GO than those in 2 and 5 wt% Pd/r-GO. The Song and Gai group employed chitin supported Pd NPs to hydrogenate aqueous Na$_2$CO$_3$.[127] Under 40 bar H_2/CO_2 (1 : 1) at 60 °C, FA was produced with a TOF of 257 h^{-1}.

The existence of hydroxyl groups on the surface of the support is proposed to enhance the overall catalytic performance by improving the CO_2 adsorption.[128] The Wang and Ma group has prepared Ru catalysts on various supports and shown that the reactivity followed the order of Ru/MgO (no activity) < Ru/AC (TON of 10) < Ru/γ-Al$_2$O$_3$ (TON of 91) under 13.5 MPa H_2/CO_2 (5/8.5) in EtOH/NEt$_3$ at 80 °C, since γ-Al$_2$O$_3$ has more hydroxyl groups on the surface. The presence of RuO$_2$ during catalyst preparation was found to have a detrimental effect on the activity. They further examined Ru-DBU/Al$_2$O$_3$ for hydrogenation of scCO$_2$ under 15 MPa H_2/CO_2 (2 : 3) in the presence of NEt$_3$ at 80 °C to achieve a maximum TOF of 239 h^{-1}.[129] Liu et al. later applied γ-Al$_2$O$_3$ nanorods (γ-Al$_2$O$_3$(n)) as a support and obtained superior reactivity with a TON of 731 compared to that of Ru/γ-Al$_2$O$_3$ under otherwise similar reaction conditions.[130,131] The high surface area with abundant hydroxyl groups likely increased the interactions with the Ru species to offer improved activity. The Mori and Yamashita group used layered double hydroxides (LDHs) as the support to prepare single-atom Ru catalysts and achieved a maximum TON of 698 under 2 MPa H_2/CO_2 (1 : 1) at 100 °C with a Mg^{2+}/Al^{3+} ratio of 5 in the LDH.[132] The catalytic activity was significantly influenced by the CO_2 adsorption capacity in the vicinity of the Ru center.

Mu and co-workers reported nano-Ni as an efficient catalyst for FA synthesis using 1 mM NaHCO$_3$.[133] The reaction pathway was elucidated by DFT calculations to involve the attack of active H to C of HCO$_3^-$ (Fig. 19) and subsequent removal of the hydroxyl group from the bicarbonate moiety. Finally, the remaining active site of H_2 combines with the hydroxyl group to produce water along with FA.

Nguyen et al. explored bimetallic synergism towards CO_2 hydrogenation. Employing carbon nanotube–graphene supported PdNi alloys (PdNi/CNT–GR), base free FA synthesis was achieved.[134] The choice of the composite support materials was determined in order to avoid the stacking of GR and bundling of CNTs. Applying bimetallic PdNi/CNT–GR (Pd$_3$Ni$_7$/CNT–GR; Pd – 30%, Ni – 70%), 1.92 mmol of FA was generated along with a trace amount of acetic acid under 5 MPa H_2/CO_2 (1 : 1) at 40 °C,

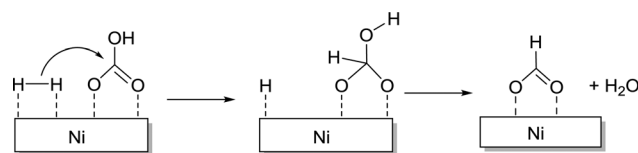Fig. 19 Pathways of the CO_2 reduction process on Ni nanoclusters in aqueous solutions.

This journal is © The Royal Society of Chemistry 2021

Energy Environ. Sci., 2021, 14, 1194–1246 | 1207

Table 5 Overview of selected bulk and supported metal catalysts

Catalyst precursor	Solvent	Base/additive	H_2/CO_2 (bar)	Temp. (°C)	TON	TOF (h^{-1})	Ref.
Pd bulk	H_2O	$KHCO_3$	60/0	70	5	0.22	113
Pd bulk	H_2O	$NaHCO_3$	1/0	RT	2.1	0.02	115
Ni/Fe powder	H_2O	K_2CO_3	0/11	300	0.022	0.01	116
Ru NPs	[DAMI][OTf]	NA	250/250	50	19 862	9931	118
Ru NPs	[DAMI][OTf]	H_2O	250/250	50	24 545	4909	118
Ru NPs	$scCO_2$	NEt_3/H_2O	50/130	80	6351	2117	119
NiNPore	H_2O	$NaHCO_3$	60/0	200	3476	1738	120
Pd/C	[Bmim][OAc]	NA	50/30	40	594	NA	121
Pd NP/C	H_2O	$NaHCO_3$	1.7/0	RT	115	25	115
Au (AUROlite)/TiO_2	NEt_3	NEt_3	90/90	40	855	16.4	117
Au/SiO_2–Schiff	H_2O/CH_3OH	NEt_3	50/30	90	14 470	1206	124
Au NP/MgAl-HT	EtOH	NEt_3	20/20	70	91	4.5	123
Au NP/TiO_2	EtOH	NEt_3	20/20	70	111	5.5	123
Au NP/Al_2O_3	EtOH	NEt_3	20/20	70	215	11	123
Ru/AC	EtOH	NEt_3	50/85	80	10	10	128
Ru/γ-Al_2O_3	EtOH	NEt_3	50/85	80	91	91	128
Ru-DBU/Al_2O_3	DMSO	NEt_3/KH_2PO_4	60/90	80	NA	239	129
Ru/γ-$Al_2O_3(n)$	EtOH	NEt_3	50/85	80	731	731	130
Ru/LDH	H_2O	NaOH	10/10	100	698	29	132
PdAg/amine-RFX	H_2O	$NaHCO_3$	10/10	100	867	NA	135
Pd/AC	H_2O	$NaHCO_3$	27.5/0	RT	527	527	125
Pd/AC	H_2O	$KHCO_3$	27.5/0	RT	567	567	125
Pd/AC	H_2O	NH_4HCO_3	27.5/0	RT	782	782	125
Pd/r-GO (1 wt%)	H_2O	$KHCO_3$	40/0	100	7088	221	126
Pd/r-GO (5 wt%)	H_2O	$KHCO_3$	40/0	100	1658	165	126
Pd NP/chitin	H_2O	Na_2CO_3	20/20	60	NA	257	127

albeit with a small TON of 6.4. The fact that mono-metallic counterparts Pd/CNT–GR and Ni/CNT–GR both exhibited poorer catalytic efficiency suggested plausible bimetallic cooperativity. Later, Mori, Yamashita and co-workers also synthesized a series of catalysts comprising PdAg NPs supported on resorcinol-formaldehyde polymers having variable amine contents (PdAg/amine-RFX).[135] Employment of the support with the highest amine concentration resulted in a maximum TON of 867 towards FA synthesis, which was around 10 times higher than that of monometallic Pd/amine-RFX, again suggesting the importance of bimetallic cooperativity. Very recently, the Yu and Yan group has demonstrated zeolite-encaged Pd–Mn nanocatalysts (PdMn$_X$@S-1) for efficient CO_2 hydrogenation to formate.[136] With catalyst PdMn$_{0.6}$@S-1, the highest formate generation rate of 382 mol$_{formate}$ mol$_{Pd}^{-1}$ h^{-1} was achieved at room temperature with a TOF of 466 h^{-1}. This was around 2-fold higher than that of catalyst Pd@S-1. This superior reactivity was attributed to the bimetallic synergism between Pd and Mn species, which increases the electron density on Pd surfaces and in turn

improves the reaction rate. The important results discussed in Sections 2.2.1 and 2.2.2 have been summarized in Table 5.

2.2.3. Heterogenized catalysts. Compared to homogeneous systems, the advantage of heterogeneous catalysts seems limited to easy product separation and recyclability. As existing homogeneous catalysts exhibit the best performance, heterogenization of homogeneous complexes may provide an opportunity to combine the strength of both homogeneous and heterogeneous systems.

2.2.3.1 Grafted molecular catalysts. Mesoporous silica supported immobilized Ir complexes (**98–101**) for CO_2 hydrogenation were first reported by Hicks and co-workers (Fig. 20).[137] Among several grafted complexes (**98–101**) and the homogeneous analog (**102**), catalysts having a phosphine backbone (**98–100** and **102**) were found to be active (Fig. 20). Using catalyst **98**, a TON of 1300 was obtained under 4 MPa H_2/CO_2 (1:1) in the presence of NEt_3 as the base in H_2O at 60 °C after 2 h. Under similar reaction conditions, the rest of the catalysts performed poorly, *e.g.* **99**,
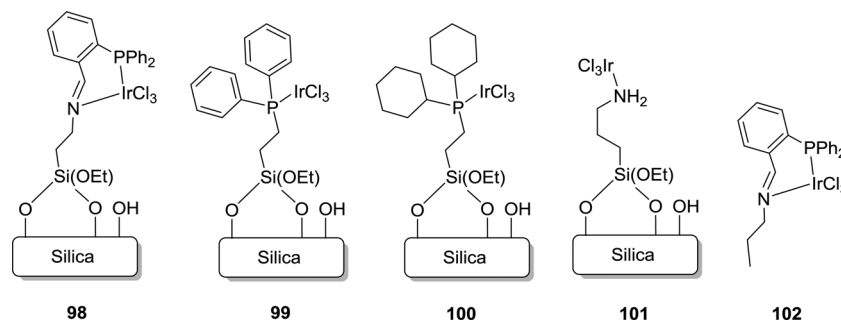

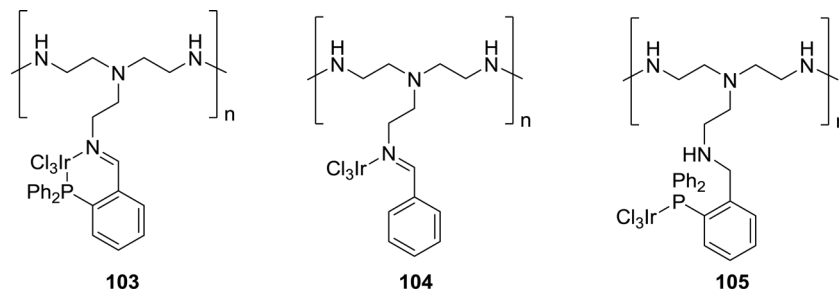**Fig. 20** Examples of grafted Ir catalysts.

1208 | *Energy Environ. Sci.,* 2021, **14**, 1194–1246

This journal is © The Royal Society of Chemistry 2021

Fig. 21 Polyethyleneimine (PEI) supported Ir catalysts.

100 and **102** with TONs of 110, 400, and 70, respectively. Continuing the reaction for a longer time (20 h) and elevating the temperature to 120 °C resulted in higher TONs of 2700 and 2300, respectively, for **98**. X-ray photoelectron spectroscopy (XPS) revealed similar environments around Ir metal in **98** (61.6 eV) and **102** (61.8 eV), but such a substantial difference in catalytic activity suggested the improved stability and activity of the homogeneous system upon heterogenization. The Hicks group further explored polyethyleneimine (PEI), an aliphatic amine-based organic polymer containing primary, secondary and tertiary amine groups, as a support (Fig. 21).[138] Such materials have the unique property to stabilize formate and act as a CO_2 capturing agent. Imine containing catalyst **104** exhibited superior activity compared to catalyst **103**, generated by tethering complex **102** on PEI, and catalyst **105**, having a phosphine backbone. Interestingly, increasing the Ir loading on the PEI backbone had a significant effect on the reactivity. Ir-25% (PEI-PN/Ir-25) exhibited a reduced TOF of 94 h^{-1} compared to Ir-65% (PEI-PN/Ir-65) with a TOF of 310 h^{-1}, likely due to the existence of agglomerated Ir NPs as confirmed by XPS and TEM. Furthermore, the catalyst efficacy decreased during the recycling experiments, particularly for low molecular weight PEI catalysts, due to the increased solubility.

Yamashita and co-workers reported a PEI-tethered Ir–iminophosphine complex (Ir–PN–PEI) immobilized in titanate nanotubes (TNTs), Ir–PN–PEI@TNT, for CO_2 hydrogenation (Fig. 22).[139] Using Na$^+$ type TNT, the resultant Ir–PN–PEI@TNT(Na$^+$) (**106**) afforded continuous FA production over 20 h with a TON of 1012 under 2.0 MPa H$_2$/CO$_2$ (1:1) at 140 °C. Comprehensive structural analyses suggested that these TNTs provided tight interactions of the active components with the support. CO_2 adsorption measurements and kinetic studies indicated that the ability of the TNTs to strongly stabilize the polymer species and to adsorb/condense CO_2 molecules in the vicinity of the active Ir centre is the key to its catalytic performance.

Zheng and co-workers extensively examined the effect of various supports and the donor atoms for CO_2 hydrogenation to FA/formate.[140–144] A variety of immobilized Ru complexes with silica, mesoporous MCM-41, and polystyrene as the support and different functional donor groups, such as CN, SH and NR$_2$, were investigated (**107–116**; Fig. 23). Under 14.7 MPa H$_2$/CO$_2$ (5.4/9.3) in EtOH using NEt$_3$ as the base and PPh$_3$ as an additive at 80 °C, the amine functionalized MCM-41 support (**107**, TON = 1022) exhibited better activity than those of the nitrile (**108**, TON = 723) and thiol (**109**, TON = 537) functionalities. This trend was attributed to the stronger electron donating ability of amine groups to metal ions. Interestingly, during recycling studies, catalyst **109** retained its integrity for a longer time than catalysts **107** and **108**, which deactivated faster. This robustness was due to a better back donating ability of the SH group than the CN and NR$_2$ donors. **107** also displayed better reactivity than that of silica supported **110** (TON of 656), due to the high surface area (852 m^2 g^{-1}) and the uniform pore size (3.5 nm) of MCM-41. Catalyst **110** having the organic support polystyrene displayed somewhat poorer activity with a TON of 151 under otherwise similar reaction conditions. Among various amine functionalized silica supported catalysts, **112** containing secondary amine groups
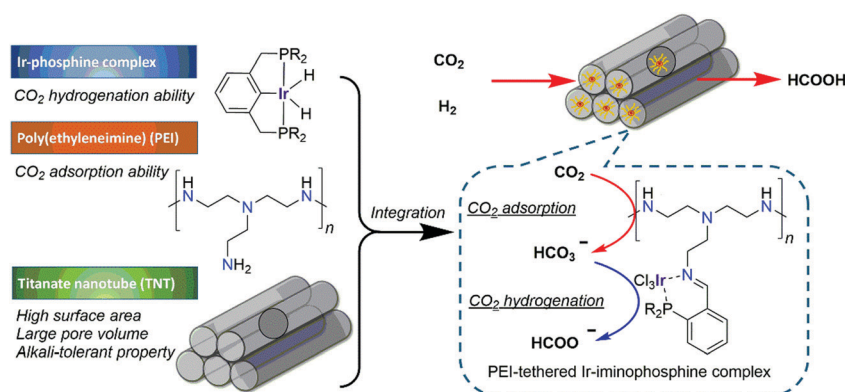

Fig. 22 Schematic illustration of Ir–PN–PEI@TNT(Na$^+$) **106** mediated CO_2 hydrogenation.[139]
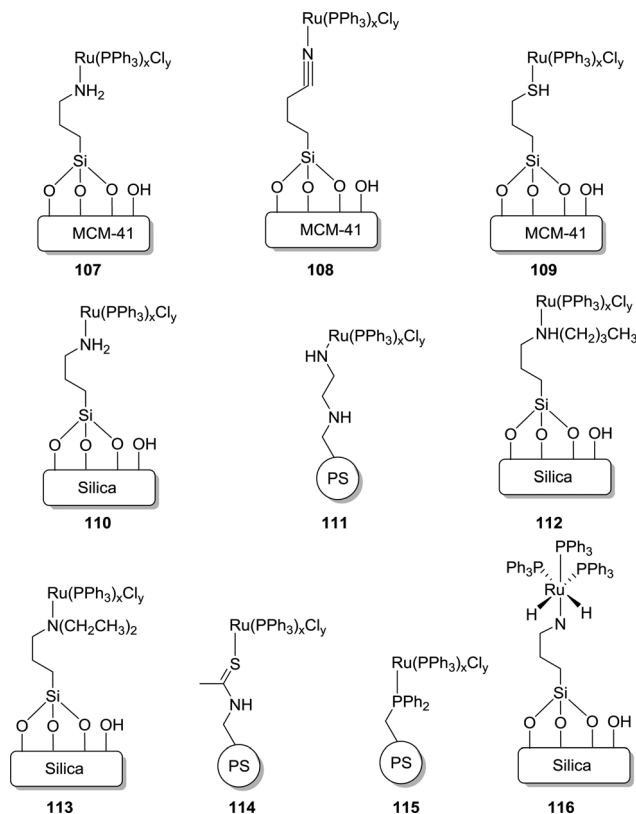
Fig. 23 Examples of grafted Ru catalysts with various supports and functional groups.

was more active with a TON of 1384 compared to **110** (TON of 656) and **113** (TON of 868). Similarly, catalyst **111** performed slightly better with a TON of 151 than **114** (TON of 75) and **115** (TON of 143). These observations indicated that the catalyst efficacy depends sensitively on the electron donating ability of the ligands. It was proposed that the octahedral dihydrido Ru **116** may serve as the active catalytic species in these reactions. Inspired by the work of Zhang, Han *et al.* prepared a molecular heterogeneous pre-catalyst "Si"–(CH$_2$)$_3$NH(CSCH$_3$)–[RuCl$_3$–PPh$_3$] (**117**) supported with silica and polystyrene. The precatalyst was synthesized by mixing RuCl$_3$·3H$_2$O and "Si"–(CH$_2$)$_3$NH(CSCH$_3$) with subsequent addition of the PPh$_3$ ligand.[145] Amine functionalized ILs were used as a reusable base during this process. The resulting formate salt and catalyst could easily be separated by filtration. Using **117** and the IL under 18 MPa H$_2$/CO$_2$ (1:1) gave a maximum TOF of 103 h^{-1} at 60 °C. Subsequently, diamine-functionalized ILs were also employed to enhance the TOF to 920 h^{-1} under 18 MPa H$_2$/CO$_2$ (1:1) at 80 °C.[146]

2.2.3.2 Heterogenized porous polymers. Considering the high surface area and well defined porosity of porous organic frameworks, they were explored as potential catalyst supports to outperform silica, polystyrene and aliphatic polymer supports.[147,148] Liu and co-workers synthesized a Tröger's base-derived microporous organic polymer (TB-MOP) supported Ru catalyst TBMOP–Ru (**118**) by coordination bonding between the
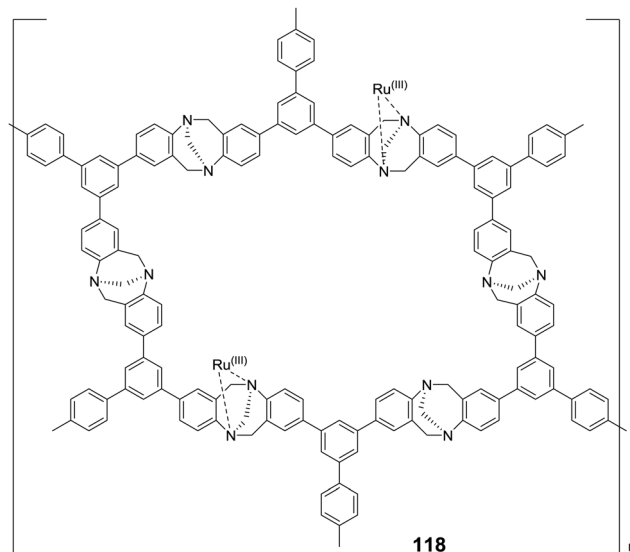

Fig. 24 Structural representation of catalyst **118**.

Ru ions and the N atoms of the TB-MOP (Fig. 24).[149] The microporous structure was confirmed by Brunauer–Emmett–Teller (BET) measurements. Under 12 MPa H$_2$/CO$_2$ (1:1) in the presence of NEt$_3$ as the base and PPh$_3$ as the additive, decent activity was achieved with a TON of 2254 at 40 °C after 24 h. The activity significantly dropped in the absence of PPh$_3$, suggesting that PPh$_3$ may mediate *in situ* generation of the active catalytic species. Moreover, during the recycling studies, catalyst leaching (detected by ICP-OES) occurred, and a reduced TON was observed from the second cycle onwards. This was attributed to the weaker complex forming ability of the Tröger's base compared to PPh$_3$.

The pioneering work of Himeda on homogeneous Cp*Ir catalysts has set a benchmark for other systems to achieve comparable reactivities. The Yoon group developed a procedure to immobilize complex **22** within a covalent triazine framework (CTF) (Fig. 25).[150] bpy incorporated CFT (bpy–CTF) was treated
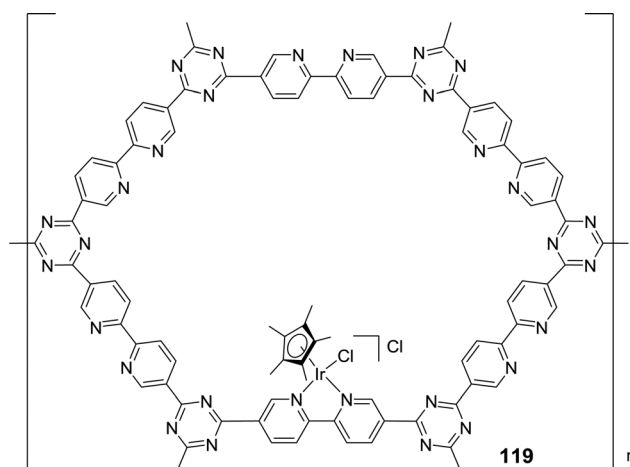

Fig. 25 Structural illustration of catalyst **119**.

1210 | *Energy Environ. Sci.*, 2021, **14**, 1194–1246

This journal is © The Royal Society of Chemistry 2021

with $[IrCp*Cl_2]_2$ to afford a heterogenized material, bpy–CTF–$[IrCp*Cl]Cl$ (**119**). XPS measurements of **119** and its homogeneous analog revealed an identical binding energy for Ir $4f_{7/2}$ (62.1 eV), indicative of a similar coordination environment around the Ir center. This was further confirmed by SEM, illustrating a uniform distribution of Ir and Cl atoms throughout the material. Moreover, EDS and XPS studies supported that the atomic ratio of Cl and Ir was close to 2. Detailed analysis of ICP-MS revealed a relatively high Ir content (4.7 wt%) in the framework, suggesting the presence of one $[IrCp*]$ unit for every sixth CTF ring. Under 4 MPa H_2/CO_2 (1:1), **119** gave a TON of 500 in the presence of NEt_3 in H_2O at 80 °C after 2 h. A TON of 3320

was achieved by increasing the temperature to 120 °C, but a higher temperature, 160 °C, led to a decrease in the activity (TON = 2720). Such observations were well correlated to the exothermic nature of the reaction. Moreover, a maximum TON of 5000 was achieved when the total pressure of H_2/CO_2 was increased to 8 MPa at 120 °C. **119** was reused with no substantial loss of activity for up to five runs.

Most of the above mentioned catalytic tests were performed under batch conditions but Urakawa *et al.* demonstrated a continuous synthesis of FA and methyl formate using DCP–CTF–$[IrCp*Cl]Cl$ (**120**) (DCP = 2,6-dicyanopyridine) (Fig. 26).[151] The microporous structure was confirmed by BET measurements (surface area of 734 $m^2 g^{-1}$) and STEM and EDX analyses further indicated the homogeneous dispersion of Ir in the matrix. When the reaction mixture ($H_2:CO_2:S = 4:4:1$ molar ratio, S = MeOH, H_2O, NEt_3) was introduced into the reactor containing **120** at 300 bar at 100 or 180 °C, weight time yields of 5.4–385.5 $mg_{FA} g_{Ir}^{-1} h^{-1}$ were achieved. *In situ* vibrational spectroscopy revealed that strong interactions of CO_2 and H_2 with CTF may account for its stability even under harsh supercritical and flow conditions.

Yoon and co-workers further immobilized $[IrCp*Cl_2]_2$ onto graphitic carbon nitride (g-C_3N_4) (**121**) and a heptazine-based framework (HBF) (**122**) (Fig. 27).[152] EDS measurements revealed the ratio of Ir to Cl as 1:2 and SEM analysis suggested uniform metalation. ICP-MS analysis of **122** revealed a very low Ir content (0.86 wt%) in the framework. Under a total pressure of 8 MPa, **122** afforded a TON of 6400 in H_2O at 120 °C after 10 h in the presence of NEt_3. **122** could be recycled for five runs without any substantial loss of activity and, in each run, 90% catalytic activity was retained with an average TON of 4000.

Yoon *et al.* also grafted $Ru(acac)_2$ onto CTF and synthesized an analogous material to **119**, $[bpy–CTF–Ru(acac)_2]Cl$ (**123**) (Fig. 28). A maximum initial TOF of 22 700 h^{-1} was achieved under 8 MPa H_2/CO_2 (1:1) at 120 °C.[153] **123** was recycled for
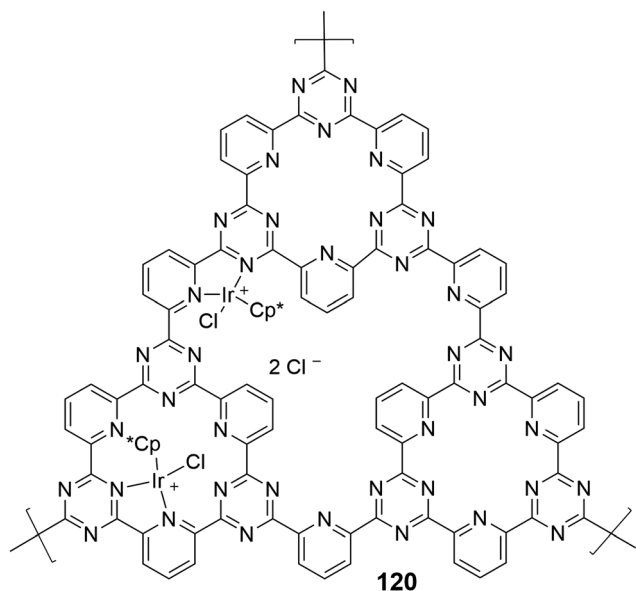

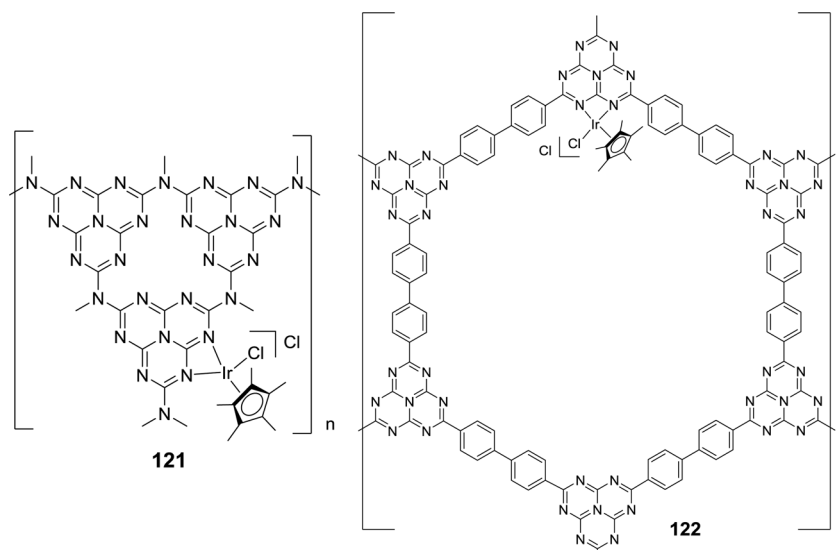Fig. 26   Structural representation of catalyst **120**.

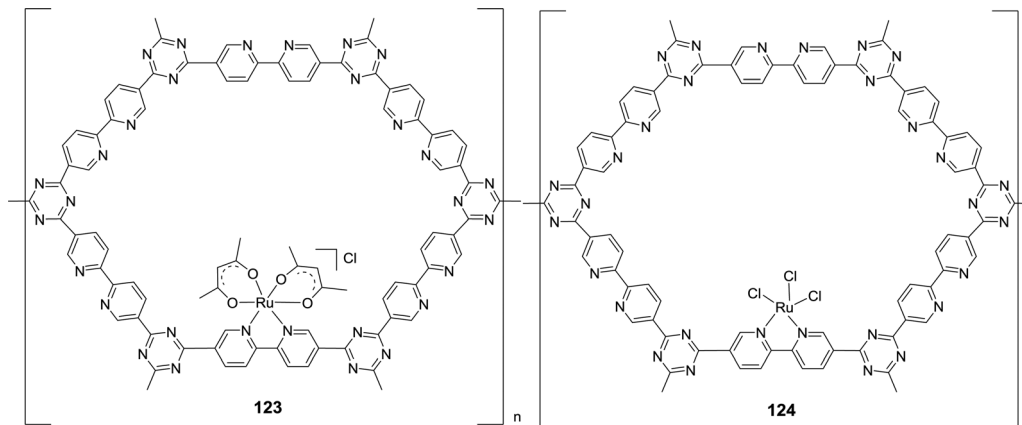Fig. 27   Structural representation of catalysts **121** and **122**.

This journal is © The Royal Society of Chemistry 2021

Energy Environ. Sci., 2021, **14**, 1194–1246 | **1211**

Fig. 28 Structural representation of catalysts **123** and **124**.

4 consecutive runs and the catalyst integrity was maintained throughout the reactions as confirmed by SEM-EDS mapping and XPS analysis. When $RuCl_3 \cdot xH_2O$ was grafted onto the same support, the resulting [bpy–CTFRuCl$_3$] (**124**) gave an initial TOF of 38 800 h^{-1} and produced formate in the presence of NEt_3 with a final concentration of 2.05 M in 2.5 h (Fig. 28).[154] **124** was also reused over 5 cycles without loss of activity.

The Yoon group also exploited mesoporous g-C$_3$N$_4$ as the support for Pd NPs (Pd/mpg-C$_3$N$_4$) (**125**) and studied CO$_2$ hydrogenation.[155] Under 4 MPa H$_2$/CO$_2$ (1:1) in a 20% NEt$_3$/D$_2$O solution at 150 °C, Pd/mpg-C$_3$N$_4$ afforded a TON of 81 after 24 h. Keeping the other parameters fixed but increasing $p(H_2)/p(CO_2)$ to 2 resulted in an enhanced TON of 106. Later, Mondelli, Pérez-Ramírez, and co-workers studied a bifunctional catalyst comprising Pd NPs deposited on bulk g-C$_3$N$_4$ under base-free conditions for FA production.[156] The Pd metal provided the necessary redox sites for H$_2$ splitting, whereas the basic amino groups of the support were involved in CO$_2$ activation. Thermal exfoliation, hard-templating and carbon enrichment were performed to maximize the edge-defects of the g-C$_3$N$_4$ carrier, which in turn enhanced the catalyst productivity. Subsequently, the Huang and the Liang groups developed a mesoporous Pd catalyst (Pd/u-CN$_{100}$) (**126**) tethered on Schiff base modified graphitic carbon nitride having a high surface area (Fig. 29).[157] Grafting of an appropriate amount of terephthalaldehyde (TPAL) into the support led to scattered Schiff base and multiple nitrogen based species. These had a significant impact on the high dispersion of Pd nanoclusters, electronic environment and a large promotion of the material surface area and volume, which in turn influenced the catalytic efficiency. Under 7 MPa H$_2$/CO$_2$ (1:1), **126** afforded a maximum TOF of 98.9 h^{-1} at 110 °C in EtOH.

The Palkovits group reported cross-linked polyphosphine (pdppe) as a support for [(Ru(p-cymene)Cl$_2$)$_2$] for CO$_2$ hydrogenation to formate (Fig. 30).[158] The XPS measurement of the resulting Ru@pdppe (**127**) confirmed the oxidation state of Ru as +2 and the TEM analysis revealed the absence of any NPs. Under 100 bar H$_2$/CO$_2$ (1:1) in the presence of K$_2$CO$_3$ in water, a maximum TON of 13 170 was observed at 120 °C. Recycling studies were performed for up to eight runs; however, a
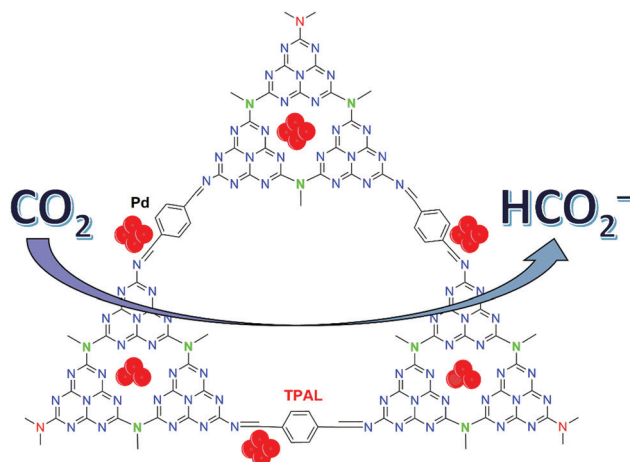

Fig. 29 Schiff base modified Pd/u-CN$_{100}$ (**126**) catalyst for CO$_2$ hydrogenation.[157]

significant deactivation was observed after the first cycle, due to the structural changes of the metal complex.

Recently, Jung et al. employed a melamine polymer-network (MPN) as the support for grafting $RuCl_3 \cdot xH_2O$ to prepare Ru@MPN (**128**) (Fig. 30).[159] Under 80 bar H$_2$/CO$_2$ (1:1), **128** afforded a maximum TON of 4706 in H$_2$O at 120 °C after 12 h in the presence of NEt$_3$. From experimental observations, a mechanism was proposed where HCO$_3^-$, generated by the reaction of CO$_2$ and H$_2$O in the presence of NEt$_3$, replaces the metal coordinated chloride. It is followed by the reaction with H$_2$ to generate a Ru–H intermediate as the active catalytic species (**129**) (Fig. 30). CO$_2$ can then be inserted into the Ru–H bond to generate a metal coordinated formate species (**130**; Fig. 30). **129** is regenerated by base mediated heterolytic H$_2$ splitting.

Metal organic frameworks (MOFs) could also serve as a potential candidate for supports for metal precursors. In 2017, Cheng, Wang, Lin and co-workers for the first time prepared MOF supported Ir based catalysts mbpyOH-Ir-UiO (**131**) and mbpy-Ir-UiO (**132**) for CO$_2$ hydrogenation.[160] Under 0.1 MPa H$_2$/CO$_2$ (1:1) in 1 M NaHCO$_3$ aqueous solution at 85 °C, **131** gave a better TON of 6149 than that of **132** (TON = 417).

1212 | *Energy Environ. Sci.*, 2021, **14**, 1194–1246

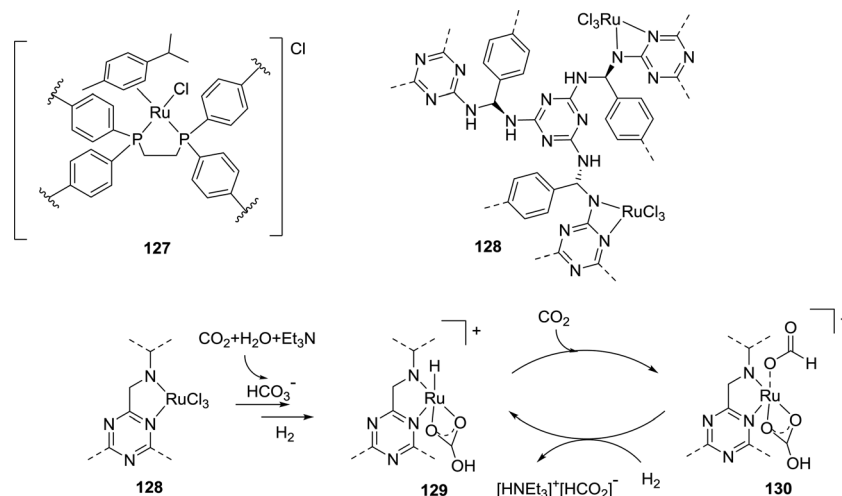This journal is © The Royal Society of Chemistry 2021

Fig. 30 Structural representation of **127** and **128**, and the proposed mechanism of CO_2 hydrogenation by **128**.

Experimentally observed high kinetic isotope effect (KIE) value of 140 suggested the involvement of a concerted proton–hydride shuttle in the rate-determining step of the reaction. A thorough computational analysis revealed the energetics of the transition states associated with the H_2 heterolysis and proton–hydride transfer steps with corresponding activation energies of 0.34 kcal mol^{-1} and 16.26 kcal mol^{-1}, respectively. This observation further suggested that the proton–hydride transfer is the rate limiting step of the process. Wang *et al.* immobilized Ru complexes, such as $RuCl_3$, $[Cp*RuCl_2]_2$ and $[Ru(C_6Me_6)Cl_2]_2$, on an azolium based MOF to prepare Ru–NHC-MOF catalysts **133–135**,

respectively.[161] Catalyst **135** was found to be the most efficient among them owing to the presence of the strong electron-donating C_6Me_6 ligand. Using K_2CO_3 as an inorganic salt additive and DMF as the solvent, a TON up to 3803 was achieved under 8 MPa H_2/CO_2 (1:1) at 120 °C. A summary of selected heterogenized catalysts for CO_2 hydrogenation is provided in Table 6.

2.3. Economic feasibility of CO_2 hydrogenation catalysts

The parameters of catalytic activity above evidently indicate that homogeneous catalytic systems mostly outperform

Table 6 Overview of selected heterogenized catalysts

Catalyst precursor	Solvent	Base/additive	H_2/CO_2 (bar)	Temp. (°C)	TON	TOF (h^{-1})	Ref.
98	H_2O	NEt_3	20/20	60	1300	620	137
100	H_2O	NEt_3	20/20	60	400	200	137
98	H_2O	NEt_3	20/20	120	2300	1200	137
98	H_2O	NEt_3	20/20	60	2700	140	137
103	H_2O	NEt_3	20/20	120	248	248	138
Ir–PN–PEI@TNT(Na^+) (**106**)	H_2O	NaOH	10/10	140	1012	50.6	139
107	EtOH	PPh_3/NEt_3	54/93	80	1022	1022	142
110	EtOH	PPh_3/NEt_3	40/120	80	656	656	140
111	EtOH	PPh_3/NEt_3	50/80	80	151	151	142
108	EtOH	PPh_3/NEt_3	54/93	80	723	723	142
112	EtOH	PPh_3/NEt_3	54/93	80	1384	1384	142
113	EtOH	PPh_3/NEt_3	40/120	80	868	868	140
109	EtOH	PPh_3/NEt_3	40/120	80	537	537	140
117	H_2O	[mammim][TfO]/PPh_3	90/90	60	206	103	145
117	H_2O	[DAMI][TfO]/PPh_3	40/120	80	1840	920	146
TBMOP–Ru (**118**)	NEt_3	PPh_3	60/60	60	2254	94	149
(Pd/mpg-C_3N_4) (**125**)	D_2O	NEt_3	27/13	150	106	4.4	155
bpy–CTF– [$IrCp*Cl$]Cl (**119**)	H_2O	NEt_3	20/20	120	3320	1660	150
bpy–CTF– [$IrCp*Cl$]Cl (**119**)	H_2O	NEt_3	40/40	120	5000	5300	150
[bpy–CTF–Ru(acac)$_2$]Cl (123)	**H_2O**	**NEt_3**	**40/40**	**120**	**21 200**	**22 700**	153
[bpy–CTFRuCl$_3$] (124)	**H_2O**	**NEt_3**	**40/40**	**120**	**20 000**	**38 800**	154
122	H_2O	NEt_3	40/40	120	6400	1500	152
Ru@pdppe (**127**)	H_2O	K_2CO_3	50/50	120	13 170	3290	158
Ru@MPN (**128**)	H_2O	NEt_3	40/40	120	4706	4964	159
mbpyOH-Ir-UiO (**131**)	H_2O	$NaHCO_3$	0.5/0.5	85	6149	410	160
mbpy-Ir-UiO (**132**)	H_2O	$NaHCO_3$	0.5/0.5	85	427	28	160
133	EtOH	NEt_3	40/40	120	313	156	161
134	EtOH	NEt_3	40/40	120	454	227	161
135	DMF	NEt_3	40/40	120	3803	1900	161

This journal is © The Royal Society of Chemistry 2021

Energy Environ. Sci., 2021, **14**, 1194–1246 | 1213

heterogeneous catalysts. Although the catalytic efficiencies are commonly characterized by their TON and TOF values, determining their practical applicability is not so straightforward and consideration based on economic parameters is necessary. To assess such a situation, we have previously introduced a dimension-free key-parameter to normalize the catalyst costs based on the TON. The "catalyst price normalized to TON" (CON, eqn (3)) describes the contribution of the catalyst in the cost of the product, formic acid.[12,19] Hence, a large TON value and a low production cost of the catalyst are advantageous. Any CON value greater than 1 suggests that the catalyst is more expensive than the product and will not be suitable for large scale application. For FA manufacturing, TOFs are less relevant, but it should be noted that a catalyst with a low TOF will require a larger reactor to achieve similar productivity to that of catalysts with high TOFs; thus, a potentially higher investment in the infrastructure may be needed.

$$CON = (P_{cat}/TON)K_{Prod} \qquad (3)$$

with $K_{Prod} = (P^{\circ}_{Prod})^{-1} \cdot (Mw_{cat}/Mw_{Prod})$, where Mw_{cat} is the molecular weight of the catalyst, Mw_{Prod} is the molecular weight of the product, P°_{Prod} is the target price of the product per kg, and P_{cat} is the price of the catalyst per kg.

Seven high performance homogeneous and two heterogeneous catalytic systems with reasonably high TON values were selected for the CON analysis (Fig. 31). The corresponding CON values were calculated for large industrial scale FA production using eqn (3) assuming a base price of $600 ton$_{FA}^{-1}$ (per ton of FA) and a 90% reduction in the catalyst cost from the lab scale (Table 7). It is understandable that low CON values are necessary for economic feasibility. Unfortunately, it is evident that most of the catalysts, except **41**, are not suitable for practical applications just based on the large CON values. It becomes even more challenging if a target base price of $300 ton$_{FA}^{-1}$ is

Table 7 Assessment of catalysts using the CON model

Catalyst	Reaction conditions	TON	Cost[a] ($ per mole)	CON
21	In H_2O at 120 °C	190 000	311 000	5.93
32	In H_2O at 200 °C	190 000	87 000	1.66
41	In H_2O/THF at 200 °C	300 000	161 000	1.94
41	In H_2O/THF at 120 °C	3 500 000	161 000	0.17
44	In H_2O at 185 °C	348 000	204 000	2.12
48	In DMF at 120 °C	200 000	97 000	1.76
79	In THF at 80 °C	58 990	18 000	1.12
82	In THF at 80 °C	46 100	22 000	1.76
123	In H_2O at 120 °C	21 200	87 000	14.79
124	In H_2O at 120 °C	20 000	86 000	15.59

[a] The cost estimation was calculated based on commercial prices of available starting materials based on the same reaction procedures and yields reported in individual literature. Since solvent and manpower costs were not taken into account, these values should be used for preliminary economic evaluation only.

assumed. One also notes that the condition to achieve a high TON for **41**, with a catalyst loading of 0.0010 μmol, may compromise the productivity. The reaction conditions should also be taken into account to justify whether the process is realistic to be ventured.

3. Electrochemical reduction of carbon dioxide

The electrochemical CO_2 reduction reaction (eCO$_2$RR) using renewable energy offers a direct pathway for power-to-formic acid where CO_2 is utilized as a storage medium as well as a feedstock for valuable fuels/chemicals, and this has previously been discussed in various perspectives, review articles and book chapters.[162–171] Electrocatalysis has several advantages: (1) the process can be controlled by adjusting the potentials and reaction temperatures, (2) the electrolytes can be recycled in many cases, (3) the set-up is modular, compact, and easy to scale
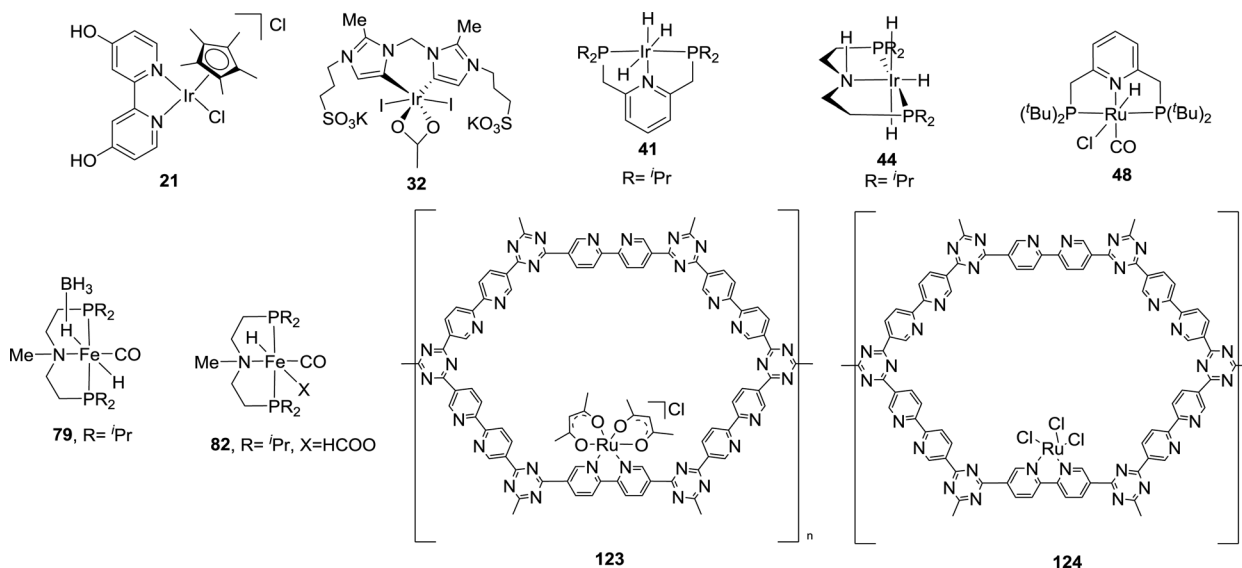

Fig. 31 Representative examples of catalysts chosen for CON calculations during CO_2 hydrogenation.

1214 | *Energy Environ. Sci.*, 2021, **14**, 1194–1246

This journal is © The Royal Society of Chemistry 2021

up, (4) the reaction may be conducted at room temperature and atmospheric pressure, and (5) direct use of renewable and/or low-carbon electricity is applicable. The eCO_2RR is, in general, considered to involve three main steps: (1) CO_2 activation by chemical adsorption of CO_2 on the surface of a catalyst, (2) electron (e^-) and proton (H^+) transfer to break C–O bonds and/or form C–H bonds, and (3) rearrangement of the product(s) followed by desorption from the electrode surface and diffusion into the electrolyte. However, the eCO_2RR faces several challenges in controlling the selectivity because the transfer of different H^+ and e^- equivalents may lead to divergent end-products (either liquids such as methanol and ethanol or gases such as CO, methane and ethylene) and the competing H_2 evolution reaction (HER).[172] Therefore, comprehensive and in-depth understanding of the thermodynamic and kinetic properties for minimizing and/or circumventing competitive pathways is critical to achieve high selectivity and energy efficiency.[173]

Significant efforts have been devoted to probing the reaction mechanisms of electrochemical CO_2-to-FA conversion with a combination of experimental results and theoretical analyses utilizing DFT studies discussed succinctly in some recent literature reports.[174–177] $HCOO^-$ or HCOOH is generated possibly via an intermediate that binds to a metal electrode either through one O atom (monodentate) or two O atoms (bidentate) (Fig. 32a). This intermediate can form via CO_2 insertion into metal-hydride bonds or through direct protonation with H^+ from solution (Fig. 32). An alternate pathway is proposed to proceed via a $CO_2^{\bullet-}$ radical that reacts readily with neighboring H_2O or H^+ to generate $HCOO^-$ or HCOOH (Fig. 32b). Sometimes, the presence of HCO_3^-

was found to enhance $HCOO^-$ production eliminating CO_3^{2-} in the solution (Fig. 32b). In this context, Sridhar and co-workers evaluated in their engineering and economic feasibility study that the propensity to produce either formate salt or FA with relatively low specific energy consumption and high faradaic efficiencies (FEs, eqn (4)) is higher compared to other CO_2 reduction products except CO.[178] The electrochemical CO_2 conversion performance is often quantified via two criteria, (i) a high energy efficiency (EE) and (ii) a high reaction rate. The EE is a vital parameter because it specifies the recoverable energy contained in the product and defines the energy cost of producing the product (eqn (5)).[162] A high EE is commonly achieved through a combination of high selectivity (faradaic efficiency (FE)) and low overpotential (η) (eqn (5))

$$\varepsilon_{Faradaic} = \frac{n \cdot F \cdot N}{Q} \quad (4)$$

$$\varepsilon_{Energetic} = \frac{E^0}{E^0 + \eta} \times \varepsilon_{Faradaic} \quad (5)$$

where $\varepsilon_{faradaic}$ = faradaic efficiency, $\varepsilon_{Energetic}$ = energy efficiency, n = number of electrons, F = Faraday's constant, N = number of moles of product, Q = charge passed, E^0 = standard potential, and η = overpotential.

Although the thermodynamic potential for one electron reduction of CO_2 to $CO_2^{\bullet-}$ is extremely high (ca. -1.90 V vs. SHE) in aqueous solution, for ne^-/nH^+ ($n \geq 2$) reduction to HCOOH, HCOO, HCHO, CH_3OH, and CH_4, these values are relatively low (Table 8). This is likely because of the involvement
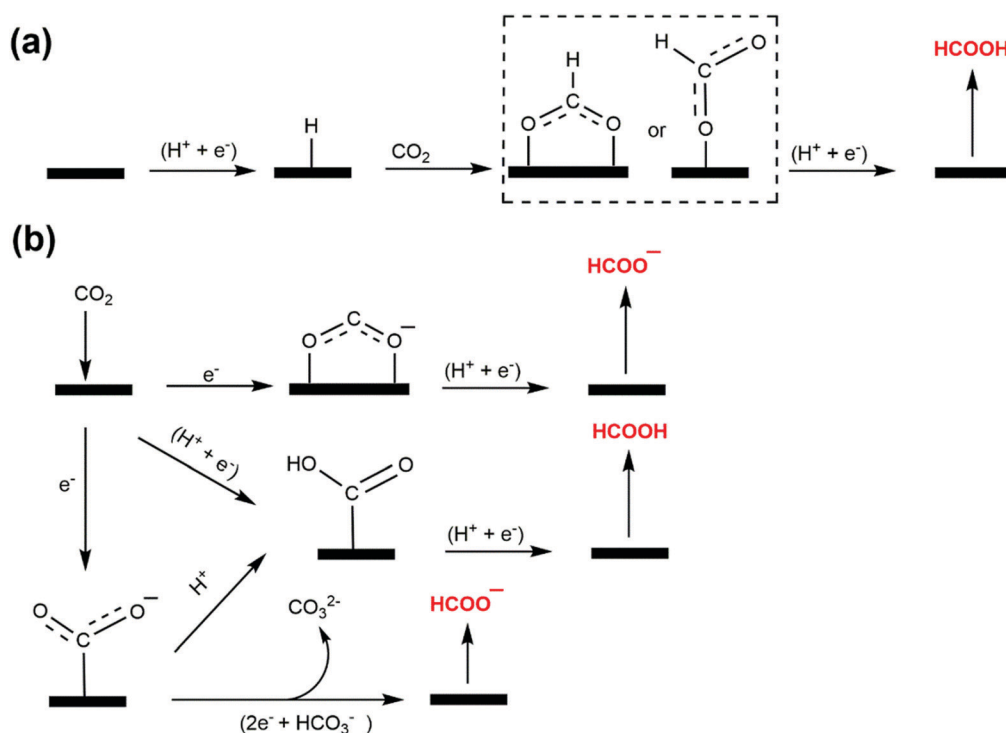

Fig. 32 Possible reaction pathways for the eCO_2RR to $HCOO^-$ or HCOOH via the (a) monodentate or bidentate intermediate route and (b) $CO_2^{\bullet-}$ intermediate route.[171,174]

This journal is © The Royal Society of Chemistry 2021

*Energy Environ. Sci.*, 2021, **14**, 1194–1246 | **1215**

Table 8 Selected standard potentials of CO_2 reduction in aqueous solutions (V *vs.* SHE) at 1.0 atm pressure and 25 °C. These values were calculated according to the standard Gibbs energies of the reactants in the reactions.[165,168,179,180]

Half-cell thermodynamic reactions	E^0 (V *vs.* SHE)
$CO_2(g) + e^- \rightarrow CO_2^{\bullet-}$	-1.900^a
$CO_2(g) + 2e^- + 2H^+ \rightarrow HCOOH(l)$	-0.250
$CO_2(g) + 2e^- + H_2O(l) \rightarrow HCOO^-(aq) + OH^-$	-1.078
$CO_2(g) + 2e^- + 2H^+ \rightarrow CO(g) + H_2O(l)$	-0.106
$CO_2(g) + 2e^- + H_2O(l) \rightarrow CO(g) + 2OH^-$	-0.934
$CO_2(g) + 4e^- + 4H^+ \rightarrow CH_2O(l) + H_2O(l)$	-0.070
$CO_2(g) + 6e^- + 6H^+ \rightarrow CH_3OH(l) + H_2O(l)$	0.016
$CO_2(g) + 8e^- + 8H^+ \rightarrow CH_4(g) + H_2O(l)$	0.169
$CO_2(g) + 2e^- + 2H^+ \rightarrow H_2C_2O_4(aq)$	-0.500
$CO_2(g) + 2e^- \rightarrow C_2O_4^{2-}(aq)$	-0.590

^{a} This potential is in water. In DMF, the value is -1.970 *vs.* SHE.

of proton coupled electron transfer (PCET) and multi-electron transfer pathways, leading to routes that involve low η processes.[166] Similarly, due to lower energy consumption, the CO_2-to-FA pathway is always favored over CO_2-to-oxalic acid ($H_2C_2O_4$) conversion (Table 8). These concepts are well-established in the literature and hundreds of catalytic systems have been developed in the past few decades where these ideas were successfully implemented to selectively produce formate/ FA from CO_2. The three most common catalyst forms for formate production are: (i) using heterogenous solid electrodes for direct reduction of CO_2, (ii) using homogeneous solution electrocatalysts, and (iii) chemically modified electrodes where catalysts are immobilized (Fig. 33a).[181] The direct eCO$_2$RR on a bare heterogenous electrode surface normally requires large overpotentials, resulting from the disparity between the applied electrode potential ($E_{applied}$) and $E^0_{(products/CO2)}$ at a given current density (CD or j; defined as the total current per unit area of the electrode and describing the total rate of reaction). Low η and high product selectivity with a considerable reaction rate constant (K_{cat}) are highly desired for a catalyst having $E^0(cat^{ox/red})$

well matched to $E^0_{(products/substrates)}$ for an ideal outcome.[167] In general, for continuous CO_2 reduction, the eCO$_2$RR is accomplished in an electrolytic cell which consists of a cathode and an anode across which an electrical current or voltage is applied (Fig. 33b). These two electrodes are usually coated with catalysts and placed in chambers separated by an ion exchange membrane. A suitable solvent/electrolyte, for transferring ions, along with CO_2, is introduced in the cathode chamber. This half-cell CO_2 reduction is completed by the 2nd half-cell complementary oxidation reaction occurring at the anode (eqn (6) and (7)). The general cathodic and anodic reactions for the eCO$_2$RR to FA are:

$$\text{Cathode: } 2CO_2 + 4H^+ + 4e^- \rightarrow 2HCOOH \quad (6)$$

$$\text{Anode: } 2H_2O \rightarrow O_2 + 4H^+ + 4e^- \quad (7)$$
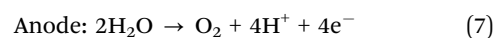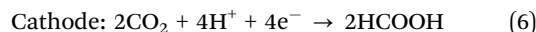
The factors governing the efficiency and selectivity of electrocatalytic production of FA are not only the reaction mechanisms involving various reaction intermediates, but also common factors and reaction parameters such as the solvents/electrolytes, pH of the solution, CO_2 pressure of the system, electrode materials, catalysts, design of the electrochemical cell/reactors *etc.* In the following section of this review, these factors will be elucidated and discussed individually, mainly focusing on the FE, η, partial current density (PCD; defined as the product of FE$_{product}$ and j), and stability of the electrocatalysts. Finally, we have provided a discussion in Section 3.6 towards the development of practical systems for electrocatalytic FA production with current progress in the field.

3.1. Effects of the solvent and electrolyte

Solvents including supporting electrolytes provide a delivery medium for protons and electrons, which are crucial during the eCO$_2$RR in aqueous medium.[182] The thermodynamic potentials as well as thermochemical properties such as pK_a or the
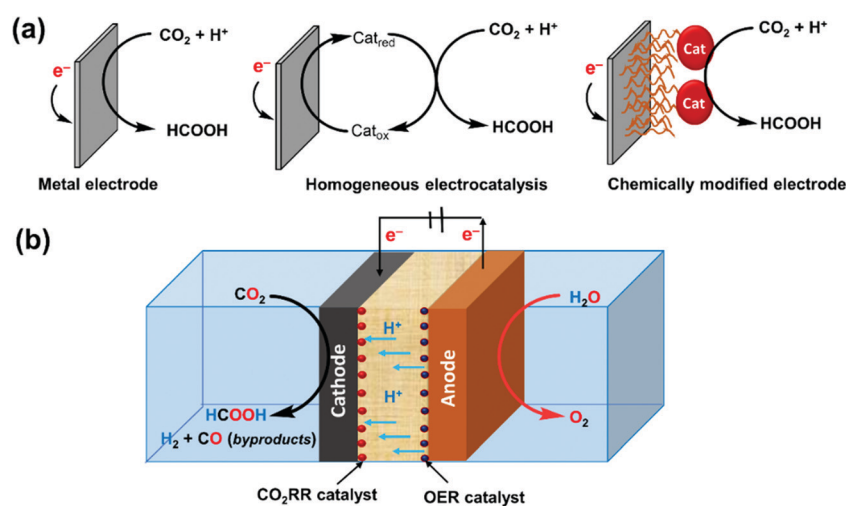

Fig. 33 (a) Electrochemical reduction of CO_2 by metal electrodes (left), homogeneous electrocatalysis (middle) and chemically modified electrodes (right). (b) Schematic representation of the electrochemical processes to convert CO_2 to FA in an electrolytic cell.

1216 | *Energy Environ. Sci.*, 2021, **14**, 1194–1246

This journal is © The Royal Society of Chemistry 2021

hydricity of the metal-hydride intermediates vary with solvents and should be tuned judiciously to suppress HER activity. Although the eCO_2RR usually occurs in an aqueous medium, the low solubility of CO_2 and competitive HER impose restrictions on the efficiency of the eCO_2RR. Recently, there is an increasing number of reports of CO_2-to-FA conversion utilizing organic solvents and solid electrolytes to achieve higher CO_2 solubility, to limit HER activity and temperature resistance, and to allow easy downstream separation of products.[183–186]

In the case of aqueous electrolytes, the use of bicarbonate (HCO_3^-) and carbonate (CO_3^{2-}) anions as the source of CO_2 can enhance the eCO_2RR by increasing the local CO_2 concentration.[187,188] On the other hand, Li^+, Na^+, K^+, H^+ and NH_4^+ cations were found to favor the eCO_2RR where $KHCO_3$ solution was the commonly adopted aqueous electrolyte and could be widely used for various electrodes including Cu, Sn, Hg, Pb, carbon, gas diffusion electrodes (GDEs) etc.[189] Typically, 0.5 M $KHCO_3$ solution saturated with CO_2 gives a pH of 7.25 ± 0.05 (pH = 8.4 when saturated with Ar). In 2017, Ikemiya et al. studied the effects of alkali metal cations (Na^+, K^+, Rb^+ and Cs^+) on the FE for the production of FA using a boron-doped diamond electrode.[190] While the highest FE of 71% was observed for a 0.075 M Rb^+ solution neutralized to pH 6.2, the lowest FE was obtained for the solution having the smallest cation Na^+. This FE dependency was rationalized by the strong interaction between alkali metals and water molecules.[191]

Non-aqueous electrolytes require the applicable salts to be soluble in organic solvents, e.g., MeOH, MeCN, DMF, etc. A mixture of KOH and CH_3OH can generate K^+ and HCO_3^- in the presence of CO_2 in MeOH to produce FA from the eCO_2RR over Cu and Pb electrodes, suppressing the HER ($FE_{H_2} < 3.5\%$).[192] Tetraethylammonium salts (TEA, $C_8H_{20}N^+$) are another type of organic electrolytes that are soluble in the organic phase. Hori and co-workers studied the eCO_2RR at a Pt electrode in 0.1 M TEAP (P: perchlorate) MeCN–H_2O mixtures at a constant CD of 5 mA cm^{-2}.[193] Pt is inert in the eCO_2RR in aqueous media and can reduce CO_2 mainly to oxalic acid in MeCN. Increasing [H_2O] leads to selectivity towards FA with a concomitant drop in oxalic acid formation.

ILs are liquid salts with high electrical conductivity suitable for eCO_2RR applications. The structure of ILs allows coordination with CO_2 to foster CO_2 adsorption on the catalyst surface and to reduce the CO_2 activation energy barrier.[194,195] For

example, 1-ethyl-3-methylimidazolium trifluoroacetate ([EMIM][TFA]) was used by the Watkins group as a co-catalyst in the electrochemical conversion of CO_2 to FA by various metals (In, Sn, and Pb) and In was found to be more active than Sn and Pb.[196] A novel [EMIM][N(CN)$_2$]/water system was also employed for the eCO_2RR to FA on a Sn powder electrode to achieve a maximum FE of 81.9% during electrolysis (η = 1.08 V) in 0.5 M of the IL by Zhang et al.[197] High selectivity for FA production has been demonstrated by Hardacre and co-workers using a porous and dendritic Cu-based electrode with a high surface area when assessed in [EMIM](BF$_4$)/H_2O (92/8 v/v) electrolyte.[198] This system produces formate with moderate activity (j = 6.5 mA cm^{-2}) and selectivity (FE = 87%) at moderate operational potential, sustained for 8 h without electrode deactivation. Increasing the concentration of water decreased the yield of formate with a concomitant increase in H_2 production. Although Cu, being a versatile electrode, generally produces multiple CO_2RR products in aqueous electrolytes, ILs particularly favor the CO_2RR to formate over H_2, highlighting the importance of the electrolyte to orient the reaction. Hollingsworth and co-workers performed selective conversion of CO_2 to formate and syngas by an anion assisted electrochemical process.[199] The IL, consisting of a superbasic tetraalkylphosphonium cation and 1,2,4-triazolate anion [$P_{66\,614}$][1,2,4Triz], absorbed an equimolar amount of CO_2 and assisted in the selective conversion of CO_2 to formate at Ag electrodes under an extremely low applied electrode potential of -0.7 V vs. Ag/Ag^+. Zhu et al. reported an efficient eCO_2RR into FA on a Pb or Sn electrode using ([BMIM]X)/H_2O/MeCN (BMIM = 1-butyl-3-methylimidazolium; X = PF_6^- or BF_4^-), an IL catholyte mixture, and the PCD reached 37.6 mA cm^{-2} at an FE of 91.6%.[183] Similarly, Wu et al. found 1-benzyl-3-methylimidazolium tetrafluoroborate ([BzMIM]BF$_4$) to be the best IL to enhance the efficiency of the PbO_2 electrode in the eCO_2RR for FA production under the same combination ternary electrolyte (IL/H_2O/MeCN).[184] A very high CD of 40.8 mA cm^{-2} was achieved with an FE of 95.5%. A speculative reaction mechanism has been proposed for the eCO_2RR to FA over the PbO_2 electrode assisted by [BzMIM]BF$_4$ (Fig. 34a). Rosenthal and co-workers demonstrated that protic ILs derived from protonated 1,8-diazabicyclo[5.4.0]undec-7-ene (DBU), [DBU-H$^+$], efficiently catalyzed the reduction of CO_2 of $HCOO^-$ ($FE_{FA} \approx 80\%$) with significant suppression of CO production in MeCN or MeCN/H_2O solution using Bi cathodes.[200] On the
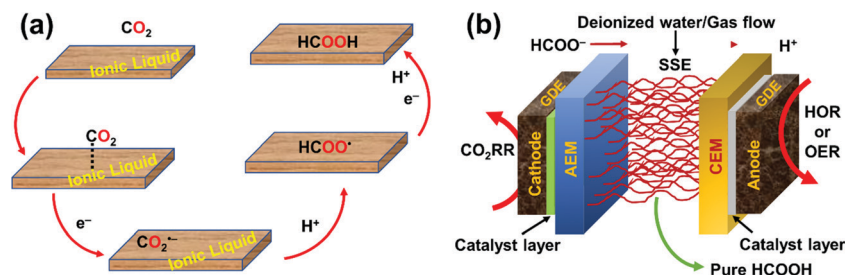

Fig. 34 (a) Possible reaction mechanism for the eCO_2RR towards FA formation in IL containing catholytes on the electrode surface.[184] (b) Schematic illustration of an all solid–state reactor containing solid electrolyte for the eCO_2RR to pure FA.[185,186]

This journal is © The Royal Society of Chemistry 2021

Energy Environ. Sci., 2021, 14, 1194–1246 | 1217

other hand, [Im]⁺-based ILs such as [BMIM]⁺ gave CO as the major product ($FE_{CO} \approx 85\%$) under the same reaction conditions. These observations indicated the crucial role of the IL cation in the product selectivity. Although the detailed role of ILs is not fully understood, Matsubara, Nakamura, and co-workers have proposed the formation of an [IL–COOH] adduct as the intermediate upon the transfer of e^-/H^+ to CO_2 (Fig. 34a).[195,201] Additional e^-/H^+ transfer to this bent CO_2 species releases FA and regenerates the original IL.

Since the eCO_2RR is often carried out in aqueous solution to facilitate ion conduction between electrodes, it is inconvenient and energy-intensive to separate a liquid product like FA from dissolved salts. To overcome this difficulty, very recently, Wang and co-workers sought to employ a porous solid-state electrolyte (PSE/SSE) in an eCO_2RR cell to produce neat FA (Fig. 34b).[185] The implementation of a novel PSE idea was inspired by battery chemistry where ions are shuttled between electrodes via ion-conducting solid polymers. The continuous production of pure FA solutions up to 12 M was successfully demonstrated with negligible degradation and high selectivity using the 2D-Bi//SSE-50//IrO₂-C cell with an average domain size of SSE of 50 μm. Furthermore, insoluble inorganic proton conductors, such as $Cs_xH_{3-x}PW_{12}O_{40}$, were also employed for pure FA generation, significantly expanding the application range. As the solid electrolyte is insoluble, those FA molecules can be collected in a deionized water flow, which makes the product concentration limited in the PSE layer, impeding its practical applications. Due to the presence of a significant amount of water, the product generation rate was not sufficiently high for industrial applications. It also involved the use of liquid electrolyte on the anode side for water oxidation. With further advancement in the field of PSE, an all-solid-state eCO_2RR system was introduced for continuous generation of high-purity and high-concentration FA vapors and solutions which can be efficiently removed in the form of vapors via inert N₂ gas flowing through the PSE layer.[186] As a result, concentrated FA could be achieved without sacrificing much selectivity compared with the deionized water flow design. Coupling with a high activity ($j_{FA} \sim 450$ mA cm⁻²), selectivity ($FE_{max} \sim 97\%$) and stability (100 h) grain boundary-enriched Bi catalyst, ultra-high concentrations of pure FA solutions (up to ~100 wt%) were achieved, condensed from generated

vapors via flexible tuning of the carrier gas stream through PSE. This new set-up distinctly represents a superior catalytic performance compared with the existing systems.

3.2. Effects of pH and pressure

The selectivity as well as the reaction rate of the eCO_2RR system can be directly influenced by the pH to avoid the inhibition of the undesired and competitive HER, which is more pronounced in acidic media. 0.1–0.5 M NaHCO₃ or KHCO₃ was found to be a suitable choice for the aqueous eCO_2RR because HCO_3^- ions can serve as a buffer to maintain the pH within 7.25 ± 0.05 although the local pH near the electrode surface may vary.[202] For sp group metal cathodes, e.g. Hg, In, Sn and Pb, the production of FA is more favored in neutral solution, and formate is produced exclusively in weak alkaline solution.[203] In this context, the relationship between the pH values and potentials of CO_2 as well as other related substances was established by Hori in a Pourbaix diagram (Fig. 35a).[204] It has been disseminated that in order to obtain formate or FA, medium potentials are required and an acidic environment is advisable regarding CD, selectivity and η. Bumroongsakulsawat and co-workers have shown that by increasing the pH of the aqueous solution from 2.9 to 7.8, the molar ratio of CO : formate decreased from 1 to 0.15 during the eCO_2RR at Sn electrodes.[205] Vlugt and co-workers have recently reported a high-pressure semi-continuous batch electrolyzer with a Sn-based cathode to convert CO_2 to FA at low pH conditions.[206] Although the FE of FA in alkaline media was higher by 10%, it produced formate that required downstream separation. As FA (with concentration > 85% of FA) is a more attractive chemical compared to formate from an economic perspective, the development of a better electrolyzer that can operate at low pH is needed (without sacrificing the product selectivity and final product concentration after downstream separation).

Apart from solution pH, the influence of elevated pressure in the electrochemical reactor has also been evaluated. Hara et al. investigated the eCO_2RR activity at a pressure of 30 atm on various electrodes at large j (163–700 mA cm⁻²) in an aq. KHCO₃ solution using a high pressure glass cell reactor enclosed in a stainless steel autoclave (Fig. 35b).[207] While j for FA and/or CO production increased with increasing CO_2

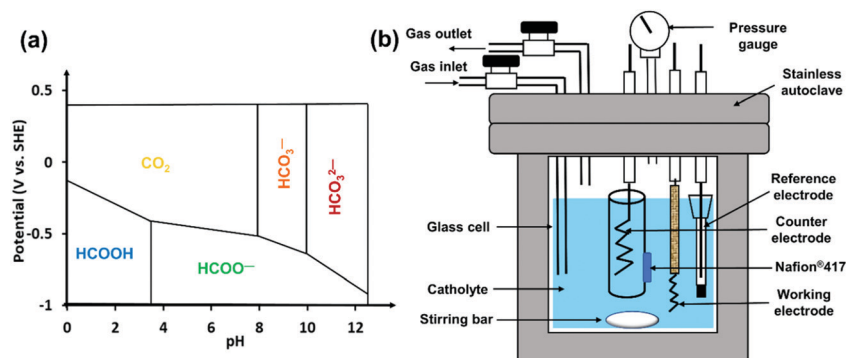**Fig. 35** (a) Potential versus pH value of CO_2 and related substances.[204] (b) High pressure reactor for CO_2 electroreduction.[207]

1218 | Energy Environ. Sci., 2021, **14**, 1194–1246

This journal is © The Royal Society of Chemistry 2021

Table 9 Effect of elevated pressure in CO_2 electroreduction to formate/FA[a]

Pressure [atm]	Electrode material	Observations	Ref.
1–5	Sn	FE_{FA} increases from 15% (1 atm) to 39% (5 atm) at a CD of 20 mA cm^{-2}	208
5–15		FE_{FA} increases 39% (5 atm) to 64% (15 atm) at a CD of 20 mA cm^{-2}	
10	Cu	FE_{FA} reaches 15%[b] at −3.0 V (*vs.* Ag quasi-reference electrode)	212
20	Cu	FE_{FA} reaches 27.8%[b] at −1.27 V (*vs.* Ag/AgCl)	213
	Hg	FE_{FA} reaches 100% at a PCD of 201.8 mA cm^{-2}	
30	Pb, In	FE_{FA} reaches 96.3% and 90.1% at a PCD of 192.6 and 180.2 mA cm^{-2}, respectively	213
40–50	Sn	FE_{FA} reaches ∼90% at a cell potential of 3.5 V and CD of ∼30 mA cm^{-2}	210
45	Cu$_2$O/Cu	FE_{FA} reaches 97.7% at a PCD of 5.2 mA cm^{-2}	211
60		FE_{FA} reaches 98.2% at a PCD of 5.7 mA cm^{-2}	
60	In, Sn, Pb	FE_{FA} reaches ∼100% for In at 20–60 °C; 99.2% for Sn at 20 °C; and 91.2% for Pb at 60 °C	214

[a] Non-selective formation of FA/formate has also been considered in this table. [b] FA forms along with other hydrocarbons, CO and H$_2$.

pressure from 1 atm to 30 atm on Ag, Au, Zn, Pb and In metals, on group 8–10 metals, the total j changed only slightly upon increasing the CO_2 pressure. Interestingly, a decrease of the CO_2 pressure to 1 atm resulted in the formation of H$_2$ for group 8–10 metals, indicating the vital role of the cell pressure during the eCO$_2$RR. Very recently, Proietto *et al.* employed an undivided filter-press cell with continuous recirculation of the electrolytic solution at a Sn cathode to convert CO_2 to FA/formate under high CO_2 pressures.[208] FE_{FA} and the final product concentrations were significantly improved from 15% and 2.0 mM to 39% and 5.8 mM to 64% and 9.6 M by increasing the CO_2 pressure from 1 to 5 bar to 15 bar, respectively. However, a further increase in the pressure did not show any significant improvement. Finally, this new system was found to be stable with time and could generate FA of a final concentration up to 0.4 M at an elevated pressure (23 bar) and CD (∼50 mA cm^{-2}). The impact of the CO_2 pressure on j for CO_2-to-FA/formate conversion was studied by Morrison and co-workers. At pressures above 10–20 bar, the FE of ∼95% and the specific energy of formation of 3.7 kW h kg^{-1} were found to be the highest.[209] The Vlugt group has also designed a unique CO_2 electrolyzer for CO_2 electrolysis to FA/formate at high pressure (up to 50 bar) using bipolar membranes (BPMs).[210] It was observed that the concentration of formate, the FE and CD sharply increased as the CO_2 pressure increased. The FE showed a maximum of ∼90% under 40 bar CO_2 with a slight decrease thereafter, likely due to formate crossover through the membrane and a pH drop caused by CO_2 dissolution. More recently, Dai *et al.* employed Cu$_2$O nanoparticle (NP) films as cathode materials for the eCO$_2$RR to HCO$_2^-$ under ≥45 atm CO_2 in bicarbonate catholytes to reach an FE of ∼98% at −0.64 V *vs.* RHE.[211] More importantly, when this cathode was paired with a newly developed NiFe hydroxide carbonate anode in KOH/H$_3$BO$_3$ anolyte, the resulting high-pressure cell could achieve an energy conversion efficiency of up to 55.8% for long-term formate production. Relevant studies and experimental results related to FA/formate formation (FE and j), aided by an elevation in partial CO_2 pressure, have been summarized in Table 9.[164]

3.3. Electrode materials

Traditional electrodes are metals that play a dual role as the support and catalyst. For example, Pd, In, Bi and Sn are active

for FA production.[215–217] However, the poor product selectivity and durability limit their practical application. With extensive inspection of eCO$_2$RR mechanisms, it emerges that electrocatalytic CO_2 reduction is highly governed by the electronic structure of the electrode materials, morphological and interfacial properties, and reaction conditions. Other than the expensive and less abundant pure metal electrodes, an electrode is commonly comprised of a cheap substrate and a catalyst layer (CL) which usually provides active catalytic sites by adhering the catalysts on its surface and facilitates electron transport with low resistance. GDEs are now often utilized in the modern fuel cell design. Highly conductive carbon black (CB) is usually used to support catalyst particles as a conventional CL, and highly porous carbon paper (CP) or carbon cloth is employed as the gas diffusion layer (GDL) (Fig. 36).[218] GDEs are found to be more advantageous due to: (1) enhanced passage and transport of gaseous CO_2 towards the active site (through the substrate and CL) and removal of gaseous by-products preventing cathode flooding, (2) easy release of the liquid product like FA into the electrolyte, (3) providing mechanical support and protection from corrosion or erosion, (4) acting as a medium for heat
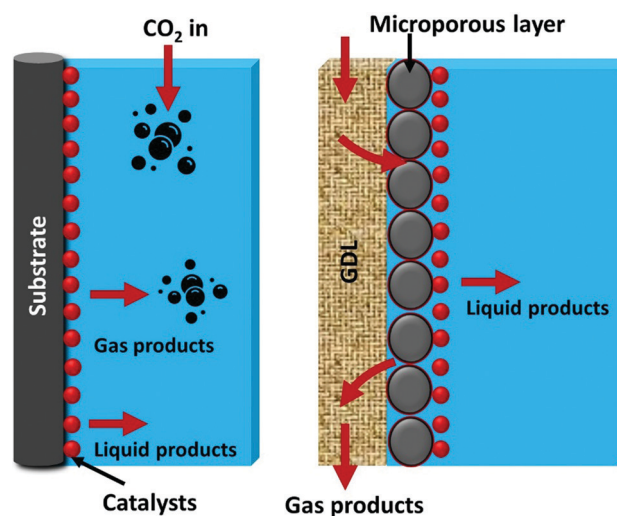

Fig. 36 Schematic representations comparing the concept of the (a) liquid-phase and (b) gas-phase CO_2RR occurring in conventional and GDEs, respectively.[218]

This journal is © The Royal Society of Chemistry 2021

Energy Environ. Sci., 2021, **14**, 1194–1246 | **1219**

transfer, and (5) avoiding the mass transport limit that prevails in liquid-phase systems due to low solubility of CO_2. Liquid-phase reactors have thus been transformed to gas-phase systems in recent years to make the eCO_2RR more feasible for practical applications. Gaseous CO_2 can be supplied directly, circumventing the major challenges associated with conventional electrodes for providing an incentive for the development of an advanced industrial process (Fig. 36). GDEs manifest a high electroactive surface for working at higher current densities than those used with conventional plate electrodes. GDEs enhance the three-phase boundary area, ultimately increasing the FE, CD and concentration of FA/formate produced.

Utilizing the advantages of GDEs, Furuya *et al.* have examined the performance of Ru, Pd and a Ru–Pd alloy (1:1) on GDEs for the eCO_2RR in 0.5 M $KHCO_3$ aqueous solution.[203] The reactivity of the Ru—Pd GDE was the highest among the others, offering high FA selectivity without CO formation and a current efficiency of 90% at -1.1 V *vs.* NHE ($j = 80$ mA cm^{-2}). Lee *et al.* fabricated a compact zero-gap electrolytic cell for a direct eCO_2RR to FA utilizing a Sn nanostructure catalyst layered onto carbon diffusion paper with 30 wt% Nafion to prepare a GDE.[219] This catalytic system showed an initial FE_{FA} of $\sim12.5\%$ at -0.7 v *vs.* RHE. While FE_{FA} decreased to 7% after 3 h of electrolysis, it remained above 5% for over 10 h of electrolysis. Recent reports that have applied this strategy with Sn catalysts for CO_2-to-formate conversion are summarized in Table 10.

A 2D-metal derived catalyst, BiOBr, was reported by Sargent and co-workers for formate production.[227] The BiOBr-templated catalyst was prepared by coating BiOBr in DMSO solution onto CP followed by annealing in an inert atmosphere. The eCO_2RR activity of the BiOBr-templated catalysts was tested in an aqueous H-cell set-up which reached CO_2 mass-transport limitations, having a CD of ~80 mA cm^{-2} and an FE of 99% (at -1 V *vs.* RHE). The PCD increases significantly (*ca.* 2.5 times) without compromising the formate selectivity when BiOBr was subsequently deposited on top of a GDE (*vide infra*).

The Huang group has demonstrated an optimized annealed Cu foam electrode with a high electroactive surface area and lower η for the eCO_2RR, taking advantage of the good conductivity and high specific surface area of the Cu-electrode.[228] While good selectivity towards the eCO_2RR was observed, the formate selectivity was low with an FE_{FA} of $\sim23\%$ at -0.45 V *vs.* RHE. Wang *et al.* deposited Sn on a Cu foam substrate (Sn/*f*-Cu) by electrodeposition in an aqueous plating solution in an effort to combine the strength of both metals through synergistic

effects. Indeed, the resulting Sn/*f*-Cu electrode exhibited excellent and superior catalytic activity compared to the individual Cu foam and Sn plate with an FE reaching a maximum value of 83.5% at -1.8 V *vs.* Ag/AgCl and PCD = 8 mA cm^{-2}.[229] The Guan group prepared Bi-doped SnO nanosheets on Cu foam (Bi–SnO/f-Cu) by a one-step hydrothermal reaction as a cathode material for the eCO_2RR to FA.[230] This material was found to be a better electrocatalyst than Sn/f-Cu with an FE of 93% at -1.7 V *vs.* Ag/AgCl, a PCD of 12 mA cm^{-2}, and good stability for 30 h of operation. Comprehensive studies revealed the role of Bi doping in stabilizing the Sn^{2+} on the surface against being reduced to Sn^0 during the electrochemical reduction process. Furthermore, DFT calculations supported the fact that, while Bi doping escalated the adsorption ability of the SnO(001) facet for OOCH* intermediates, the additional inclusion of Cu foam on Bi–SnO helped maintain Sn in a^{+ve} oxidation state, and favored the adsorption of *OOCH intermediates, thereby increasing the selectivity towards FA appreciably. To overcome the difficulties from the requirement of relatively high η and j (to reach a high FE) for metallic Bi, the Zhang group has designed lattice-dislocated Bi nanowires (NWs) on Cu foam (BiNW/f-Cu) through an *in situ* electrochemical transformation.[231] BiNW/f-Cu was proved to be an active electrocatalyst for CO_2-to-formate conversion with an FE of 95% at low η and PCD of ~15 mA cm^{-2} at -0.69 V *vs.* RHE. The great catalytic performance of the BiNW/f-Cu cathode may originate from the presence of crystal lattice dislocations and the large catalytic surface area of the porous structure of the electrode. These observations open the direction for the use of crystal defect engineering to improve the efficiency for large scale electroreduction but this is currently beyond the discussion of this review.[232]

3.4. Catalysts

Exclusive electrochemical conversion of CO_2-to-FA/formate is only achievable with highly selective catalysts that can lower the overpotential and suppress the competing HER process. The product distribution and conversion efficiency during the eCO_2RR largely depend on the cathodic catalysts. In order to obtain the best performance and maximum efficiency during electrocatalysis, it would be the ideal case if an electrocatalyst can produce a single targeted product with 100% FE at a low η with a large CD and long-term stability. The electronic structure along with a tri-phasic interface and the local morphology of the cathodic materials/catalysts have important roles to play in controlling the activity, selectivity, and durability of the catalytic

Table 10 Results of the eCO_2RR towards production of formate using GDEs with a Sn catalyst layer

Catalyst layer	Carbon support	FE (%)	PCD (mA cm^{-2})	Applied potential^a	Ref.
Sn-loaded Cu mesh	CB	78.6 ± 0.11	17.43 ± 2.60	-1.8 V (*vs.* Ag/AgCl)	220
Reduced Sn particles	PTFE^b	72.99 ± 1.91	13.45 ± 0.72	-1.8 V (*vs.* Ag/AgCl)	221
Sn nanopowder	Acetylene black + graphite + PTFE^b	~90	200	-1.57 V (*vs.* SHE)	222
Sn powder (150 nm)	CP	68.8	90	-2 V (*vs.* Ag/AgCl)	223
SnO_2 microspheres	CP	62	12.5	-1.7 V (*vs.* SHE)	224
Sn NPs	Vulcan XC72R	70	150	-1.5 V (*vs.* Ag/AgCl)	225
SnO_2	Vulcan XC72R	80	251	-1.43 V (*vs.* RHE)	226

^{a} Applied potential values are taken as reported in the literature and not adjusted. ^{b} PTFE = polytetrafluoroethylene.
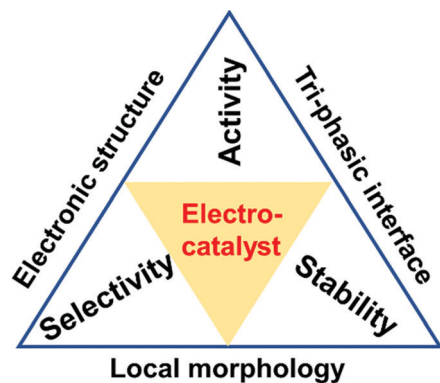
1220 | *Energy Environ. Sci.*, 2021, **14**, 1194–1246

This journal is © The Royal Society of Chemistry 2021

Fig. 37 Representations of the basic requirements for an ideal CO_2RR catalyst.[232]

Table 11 Formate production on metal electrodes in aqueous media

Electrode	Potential (vs. NHE)	PCD (mA cm^{-2})	FE (%)	Electrolyte
Pb	−1.63	5.0	97.4	0.1 M KHCO$_3$
Pb^a	−2.76	115	97.0	0.35 M Na$_2$SO$_4$ (pH 2.0)
Pb	−1.59	2.5	90	0.5 M NaOH
Hg	−1.51	0.5	99.5	0.1 M KHCO$_3$
In	−1.55	5.0	94.9	0.1 M KHCO$_3$
Sn	−1.48	5.0	88.4	0.1 M KHCO$_3$
Sn	−1.60	27	70	0.5 M NaHCO$_3$
Cd	−1.63	5.0	78.4	0.1 M KHCO$_3$
Tl	−1.60	5.0	95.1	0.1 M KHCO$_3$
Cu^b	−0.92	2.5	82.3	0.5 M KHCO$_3$

^{a} The authors report an exceedingly high FE towards formate in acidic media, which is rare. ^{b} An additive CTAB has been added to the electrolyte with an unmodified Cu electrode.

system (Fig. 37).[232] But it has been recognized that optimizing the activity and stability without compromising the selectivity of the electrocatalysts is one of the biggest challenges to be addressed before practical implementation can be realized. Importantly, the catalysts should be economical for large-scale industrial applications. In this section, the development of catalysts will be summarized in four categories.

3.4.1. Metals and metal oxides. The formation of formate by the eCO$_2$RR on metal electrodes has been known since half a century ago.[233] The most commonly explored electrocatalysts for the eCO$_2$RR are transition metal-based complexes, likely owing to the presence of vacant orbitals and active d-electrons that can energetically facilitate both the initial binding of CO$_2$ and desorption of reduced product(s). Various metals such as Pd, Pb, Hg, In, Bi, Sn, Cd and Tl primarily generate either FA or formate in an aqueous solution due to their high overpotentials for the HER and weak CO affinity.[234] Lee and Kanan developed a nanocrystalline Pb film by reducing PbO$_2$ precursors, obtaining H$^+$ reduction activity up to 700-fold lower than that of polycrystalline Pb foil electrodes without sacrificing the ability to reduce CO$_2$ to formate in aqueous solutions.[235] Even with very low CO$_2$ concentrations in an N$_2$-saturated NaHCO$_3$ solution, oxide derived Pb converted CO$_2$ from HCO$_3^-$ decomposition to formate with an FE almost close to unity while Pb foils showed less than 10% efficiency. Electrokinetic data suggested that the difference in selectivity between the two electrodes was likely caused by a difference in the coverage of a surface metastable Pb oxide layer that was passivating for H$^+$ reduction but active for CO$_2$ reduction. Other sp metals, such as Zn, Cu and Cd, typically only offer poor FEs and PCDs for the eCO$_2$RR to FA, but sometimes modifying the reaction conditions may promote high FEs and PCDs with better cell performances. Very recently, Wang and co-workers established that an additive, such as cetyltrimethylammonium bromide (CTAB), to the electrolyte can make unmodified Cu a highly active and selective catalyst for formate production from the eCO$_2$RR, reaching an FE of 82.3% in addition to a 56-fold increase in PCD at −0.5 V vs. RHE in a near-neutral aqueous electrolyte.[236] This dramatic improvement originates from the Cu–CTAB molecular interactions, which facilitate the rate-limiting HCOO* desorption step, detected through in situ Raman spectroscopy. Table 11

provides a summary of results for FA/formate production on sp-metal-based electrodes in aqueous media.[163,237]

While Pd is a very promising and commonly used d-group metal reaching high FEs at high j,[238] Rh and Ir produce mainly H$_2$ and CO with poor selectivity towards FA.[207] Surprisingly, bulk Pd is not an efficient CO$_2$RR electrocatalyst for FA production, but Pd NPs, either dispersed on carbon or embedded in conductive polymers, exhibit high efficiency and selectivity at low overpotentials but also at low j. The Wrighton group reported that a Pd-impregnated polymer on a semiconductor or metallic electrode produced formate from HCO$_3^-$ and H$_2$ with up to 85% FE and a maximum PCD of 100 μA cm^{-2} at −0.8 V (vs. SCE).[239] Similarly, an electrochemically deposited Pd on Pt electrode produced formate with an FE close to 100% near thermodynamic potentials between pH 8–10 but with a low PCD.[238] An increase in the PCD was attempted by applying η but resulted in an exclusive HER, presumably due to the faster protonation of the adsorbed H atoms. Employing dispersed Pd NPs on a carbon support, Min and Kanan were able to achieve high reaction rates, reaching an average FE of 95% with the geometric CD as high as 10 mA cm^{-2} at −0.2 V vs. RHE towards formate production (Fig. 38a).[240] Electrokinetic measurements are consistent with a mechanism where the rate-determining step is the addition of electrochemically generated surface adsorbed hydrogen to CO$_2$ (i.e., electrohydrogenation). The Pd electrodes deactivate over the course of several hours because of CO formation in a minor pathway. However, the activity is recovered by removing CO with brief air exposure (Fig. 38a). Thereafter, three different sizes of Pd NPs ranging from 3.8–10.7 nm capped with polyvinylpyrrolidone (PVP) were prepared by Broekmann and co-workers to provide insights on the size-dependent activity at low η.[241] The FE of 98% for Pd NPs (6.5 nm) was found to be the highest, followed by an FE of 86% for Pd NPs (3.8 nm) at −0.1 V vs RHE. The FE then dropped when the size of the NPs became larger. The superior efficiency towards formate production at low overpotentials for both examples was rationalized in terms of a changed catalytic pathway through a hydrogenated Pd phase (β-PdH) in situ generated electrochemically close to 0 V vs. RHE and not pure Pd as observed in bulk Pd. Later, the Sargent group designed Pd nanoneedles for the eCO$_2$RR
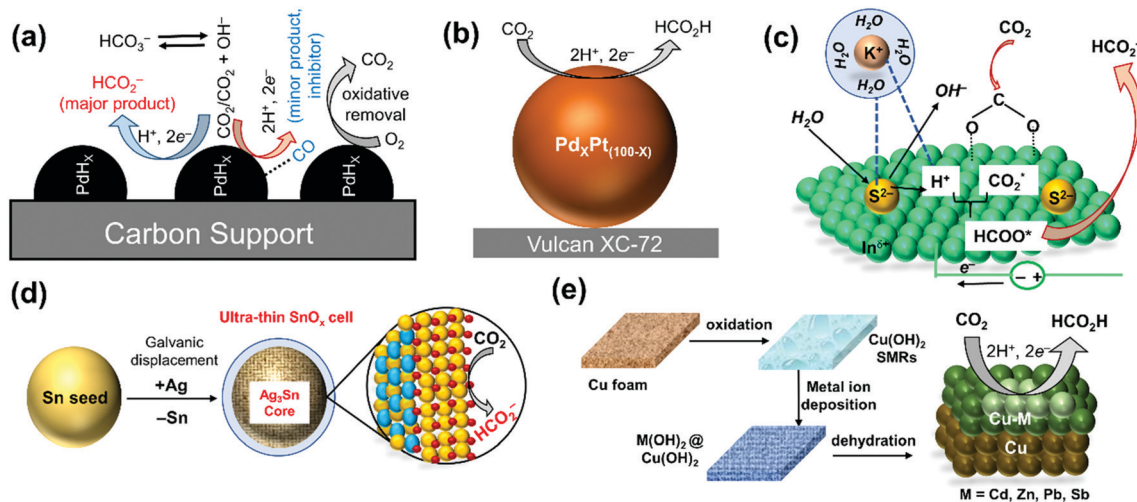
Fig. 38 Schematic representations towards formate production during the eCO₂RR by (a) PdHₓ species on the Pd/C surface *via* the electro-hydrogenation mechanism[240] and (b) PdₓPt(100−x) on a carbon support[247] in aqueous buffer. (c) Schematic illustration of the role of S²⁻ in promoting water dissociation and H* formation for the reduction of CO₂ to formate by S-doped In surfaces.[248] (d) Synthesis of an ultrathin partially oxidized tin oxide catalyst with an Ag–Sn core for the eCO₂RR towards formate production.[249] (e) Graphic illustration of the synthetic procedure of Cu–M (M = Cd, Zn, Pb, Sb) alloys from their hydroxide precursors on a Cu-foam electrode and electrocatalytic FA production.[250]

to formate and obtained an FE > 90% with an unprecedented geometric CD of 10 mA cm⁻² during controlled potential electrolysis (CPE) at −0.2 V (*vs.* RHE) over 20 h.[242] The performance and reactivity of this Pd material surpassed those of Pd nanorods, Pd particles and other previously reported Pd needles. In this study, high electric fields have been applied locally to increase the local CO₂ concentration close to the active surface. These results were supported by simulations that revealed ten-fold higher electric fields associated with metallic nanometer-sized tips compared to quasi-planar electrodes, as observed in the case of electrocatalytic CO₂-to-CO conversion as well.[243]

Realizing the advantages of using nanostructured materials over bulk materials because of their enhanced surface area arising from more surface-active sites and sharpness, Bi, located close to traditional formate-producing metals in the periodic table, has been recently considered as a promising electrocatalyst. Based on these ideas, Kim *et al.* designed an electrode of Bi nanoflakes on a Cu film by a pulse current electrodeposition method to facilitate selective CO₂ reduction to formate with an FE of 79.5% at −0.4 V *vs.* RHE for over 10 h of stability. This FE could be maximized to 100% at −0.6 V *vs.* RHE.[244] Later, the Li group reported an ultrathin Bi nanosheet (NS), derived from BiOI, to be a high-performance cathodic material for the eCO₂RR to formate with an FE > 90%, a PCD of 24 mA cm⁻² at −1.74 V *vs.* SCE, and durability for > 10 h.[217] The high performance of the Bi NS can be attributed to the enlarged surface area and abundant under-coordinated Bi sites. To gain further insights into the outstanding eCO₂RR performance, DFT calculations were carried out using the computational hydrogen electrode methodology. The energy profiles suggest that CO₂ reduction is initiated with a PCET step, leading to the protonation of a C or O atom. It was found that, while the protonation of the C atom to form the OCHO* intermediate was mildly endothermic (+0.49 eV), the 2nd PCET

was exothermic (−0.17 eV), and it finally transformed to HCOO⁻ and spontaneously releases from the catalytic surface as formate. In contrast, not only was the protonation of the O atom in CO₂ to COOH*, an intermediate to CO, significantly uphill in energy (+1.16 eV), but also the free energy of H adsorption on Bi(001) was similarly too positive (+0.95 eV) to allow an active HER. Thus, DFT calculations suggested that the high reaction selectivity is a result of its stabilized intermediate (OCHO*) on Bi(001) relative to COOH* or H*. The same group continued to fabricate a mesoporous Bi NS from Bi₂O₂CO₃ which was also very selective and stable with an FE of ∼100%, a PCD of 18 mA cm⁻² at −1.1 V *vs.* RHE, and stability > 12 h during the course of the eCO₂RR to formate.[245] Interestingly, when these Bi and mesoporous Bi NS catalysts were coupled with an oxygen evolving Ir/C catalyst to achieve full-cell electrolysis, it exhibited an impressive FE and electricity-to-formate conversion efficiency. Wu *et al.* prepared a phase-pure 2D Bi NS with a few layers from bulk solid crystals by rapid electrochemical cathodic exfoliation.[246] A cost-effective and commonly used industrial Bi ingot chunk was employed, making the catalyst preparation a greener, accessible, and up-scalable method. This cathode material maintained an FE over 80% for CO₂-to-formate conversion from −0.77 to −1.17 V *vs.* RHE, likely due to the remarkably enhanced adsorption ability of CO₂ and the corresponding intermediates. This Bi NS also displayed long-term stability for 17 h without any significant decay, stabilizing the total CD at 25 mA cm⁻² at −0.97 V *vs.* RHE. These reports strongly suggest that judicious tailoring of the nanostructure plays a key role in developing a high performance noble-metal-free catalyst for the eCO₂RR in aqueous solution.

Besides single metal materials, the use of alloys is often found to be very effective in enhancing both the activity and selectivity for the eCO₂RR to FA. A significant amount of evidence supports that the combination of different types of

1222 | *Energy Environ. Sci.*, 2021, **14**, 1194–1246

This journal is © The Royal Society of Chemistry 2021

metals can favorably control the surface chemical environment and relative binding energy with different intermediates, ultimately producing products that could not be achieved by either metal alone. Koper and co-workers prepared a Pd/Pt alloy by electrodeposition of Pd on Pt to reduce CO_2 to FA starting from -0.5 V vs. RHE at pH 6.7. This onset potential was significantly lower than -1.2 V vs. RHE for a bare Pd electrode under the same conditions.[251] Unfortunately, the formation of CO on the surface rapidly poisoned the catalyst with slow deactivation, resulting in diminished catalytic activity. Later on, the synthesis of $Pd_xPt_{(100-x)}$/C NPs was also reported, which can reduce CO_2 to FA at an even lower onset potential of 0 V vs. RHE (Fig. 38b).[247] After screening the ratios of Pd to Pt to further evaluate the effects of Pd and/or Pt in PdPt/C during catalysis, $Pd_{70}Pt_{30}$/C was found to be the best among the others towards FA production with $CD_{avg} = \sim 5$ mA cm^{-2} and an FE of 88% at -0.4 V vs. RHE. Therefore, after hybridization of Pd and Pt at a certain ratio, the CO poisoning rate could be reduced drastically without significantly affecting the kinetic parameters. It was hypothesized that, while fine-tuning of the d-band center by mixing Pt and Pd was important for enhancing the activity, lattice strain effects in the NPs induced by bigger Pt atoms were also beneficial.

The Sargent group introduced a sulfur-modulated Sn (Sn(S)) catalyst on an Au electrode by atomic layer deposition of SnS_x and subsequent reduction.[252] This modified Sn(S)/Au electrode enhanced formate generation with an FE of 93% at a geometric CD of 55 mA cm^{-2} at -0.75 V vs. RHE for over 40 h without deactivation, outperforming Sn NP/Au with an FE of 30.2% at a CD of 42 mA cm^{-2} at the same potential. This improvement in activity may come from the undercoordinated Sn sites due to the incorporation of S-atoms. Similarly, Wang and co-workers discovered a unique S-doped In catalyst, obtained by electro-reduction of S-containing In_2O_3 precursors which grew on carbon fibers, for the eCO_2RR to formate with high selectivity (FE $> 85\%$) at a high CD (25–100 mA cm^{-2}) in aqueous alkaline media.[248] When $KHCO_3$ was replaced with $CsHCO_3$, the formation rate of formate increased to a record high 1449 μmol h^{-1} cm^{-2} from 1002 μmol h^{-1} cm^{-2} with a CD of 84 mA cm^{-2} and an FE of 93%, arguably the highest formation rate of formate reported to date for the eCO_2RR. In this study, unique surface adsorbed sulfur boosting water activation was revealed where S^{-2} was proposed to interact with the hydrated K$^+$/Cs$^+$ in the double layer, contributing to the dissociation of H_2O to form adsorbed H* species. This H* could form the HCOO* intermediate, the precursor for formate (Fig. 38c).

The Jiao group synthesized an Ag–Sn/SnO$_x$ core–shell nanostructure by initiating the formation of Sn seeds in the presence of PVP, followed by galvanic displacement of Sn with Ag (Fig. 38d).[249] The SnO$_x$ shell thickness of 1.7 nm was identified to offer the best selectivity and activity with an FE of $\sim 80\%$ and a PCD of ~ 16 mA cm^{-2} at -0.8 V vs. RHE. CO_2 activation and conversion were promoted by the high electronic conductivity and oxygen vacancies in the bimetallic Ag–Sn core. Similar to the work of Jiao, Cuenya and co-workers also reported the efficacy of the SnO$_x$ layer by fabricating SnO$_x$/AgO$_x$ electro-

catalysts through electrodepositing Sn on O_2-plasma-treated Ag surfaces.[253] While SnO$_x$/AgO$_x$ displayed an enhanced CD and C$_1$ product (CO/FA) selectivity ($\geq 95\%$ at -0.8 V vs. RHE) suppressing the HER below 5% after 20 h, for Sn-free AgO$_x$ the HER selectivity was increased by $\sim 40\%$. It was proposed that the Sn electrodeposition may form stable Sn$^{\delta+}$/Sn species on the rough AgO$_x$ surface and preserve the surface roughness under the reaction conditions better than that of the uncoated AgO$_x$ surface. Bai et al. took advantage of a modified wetting chemistry reduction method to prepare activated carbon supported Pd–Sn alloy Pd$_x$Sn/C and the catalyst exhibited a nearly 100% FE at the lowest overpotential of 0.26 V, outperforming the above-mentioned Ag–Sn core–shell bimetallic catalyst.[254] The largest amount of PdO$_x$ species was formed on the surface of the catalyst by virtue of tuning the electronic state, resulting in superior performance for CO_2-to-formate conversion. While an improved FE$_{formate}$ has been observed with binary Sn-based catalysts containing Au, Ag, Pd etc., their use for large-scale CO_2 reduction systems may be limited because of the comparatively expensive materials used.

To make CO_2-to-FA conversion more economic and practical, researchers were motivated to replace more expensive and low abundance metal catalysts. Wen et al. have designed and synthesized a bimetallic Bi–Sn catalyst with unique morphology control that converted CO_2-to-formate with a remarkably high FE of 96% and a production rate of 0.74 mmol h^{-1} cm^{-2} at -1.14 V vs. RHE. The catalyst stability was maintained for over 100 h in continuous operation.[245] This excellent performance can be attributed to the sub-atomic orbital interactions between Bi NPs and the underlying Sn NS, resulting in p and d orbitals of Sn electronic states being upshifted away from the Fermi level for the electron density to shift from Sn to the more electronegative Bi. These orbital interactions can also stabilize the HCOO* intermediate, thus boosting the selectivity of formate over CO and H$_2$. Moreover, the Bi–Sn NS structure was found to be very robust with enhanced edge site exposure and could promote mass transport of CO_2 and formate during the reactions. Cui and co-workers investigated the thermochemical reaction energetics of the CO_2RR and the competing HER on Sn, CuSn, CuSn$_3$ and Cu using DFT calculations.[255] The corresponding free energy diagrams (FEDs) for these systems are presented in Fig. 39. In the case of CO and H$_2$ production, COOH* and H* are the relevant intermediates, respectively. On the other hand, while the formation of COOH* has been suggested to be the potential limiting step on Cu and Sn for formate production, it is suggested to be OCHO* on CuSn and CuSn$_3$. Both CuSn and CuSn$_3$ show higher thermodynamic limiting potential values than Cu and Sn, suggesting that the alloying of Cu with Sn significantly enhances the formate selectivity, with CuSn$_3$ having the lowest activity towards both CO and H$_2$. In addition, the structures of the alloys are markedly different from those of both Cu and Sn. Hence, it was concluded that the improved selectivity of CuSn and CuSn$_3$ alloys originates from a combination of geometric and electronic effects. Finally, this theory-guided discovery predicted Cu$_x$Sn$_y$ to be active electrocatalysts, among which the CuSn$_3$ variant is suggested to be the most promising
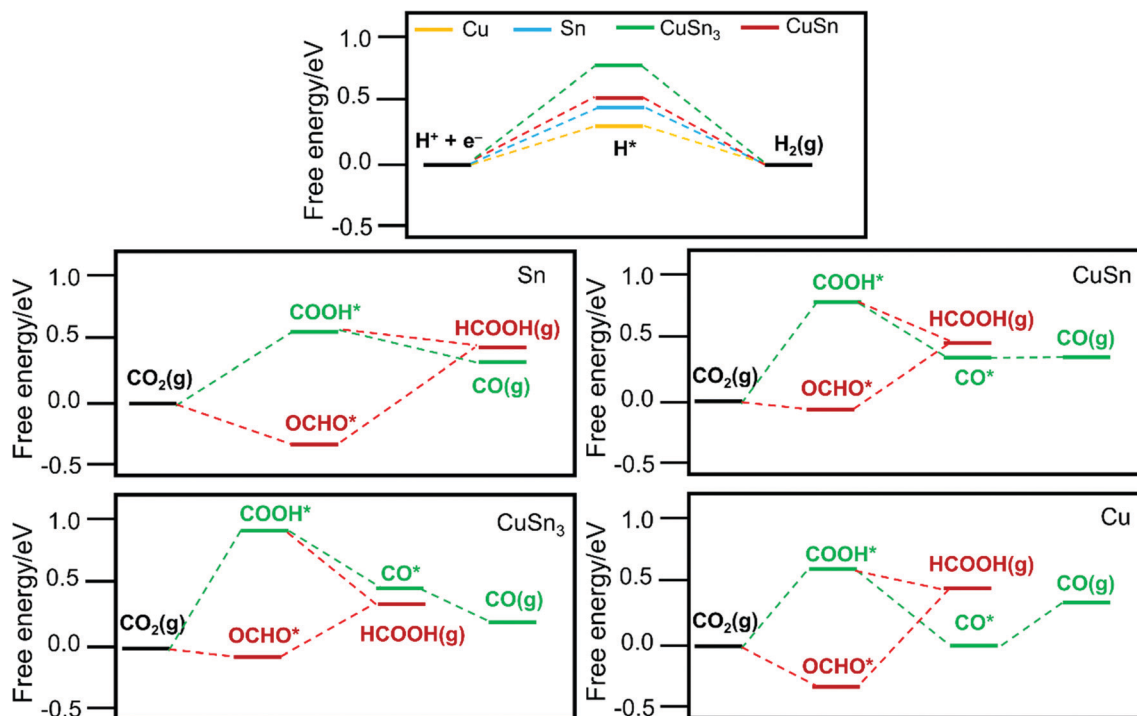
This journal is © The Royal Society of Chemistry 2021

Energy Environ. Sci., 2021, 14, 1194–1246 | 1223

Fig. 39 FEDs for CO, HCOOH and H_2 production on Sn, CuSn, $CuSn_3$ and Cu, respectively.[255]

candidate, which catalyzes the eCO_2RR to formate with a high selectivity of 95% at −0.5 V vs. RHE and excellent stability for over 50 h. It was observed that the incorporation of Cu into Sn facilitated the transfer of electrons from Sn to Cu, making Sn stay in the 0 and +2 oxidation state under the operating conditions for formate generation. On the same front, Ye et al. reconstructed a $Sn_{2.7}Cu$ catalyst and achieved a CD as high as 406.7 mA cm^{-2} with an FE of 98.0% at −0.70 V vs. RHE, and stability at 243.1 mA cm^{-2} with an FE of 99.0% over 40 h of electrolysis at −0.55 V vs. RHE.[256] The in situ reconstructed Sn/SnO_x interface may promote formate production by optimizing the binding of the reaction intermediate HCOO* to suppress the HER.

It is well-known that alloying Cu with other metals provides a useful strategy to alter the product selectivity. Mosali et al. deposited M-hydroxides (M = Cd, Sb, Pb, Zn) onto $Cu(OH)_2$ sub-micron-sized rods (SMRs), grown on Cu foam, followed by dehydration and electrochemical reduction to form MCu on the Cu SMR surface (Fig. 38e).[250] Under bulk electrolysis (BE) conditions in the presence of CO_2, CdCu@Cu exhibited the highest selectivity towards formate production with an FE of 70.5% and a PCD of 30.5 mA cm^{-2}, while ZnCu@Cu and PbCu@Cu only showed moderate selectivity with SbCu@Cu being the least. Irrespective of the composition, all alloyed structures were stable over 12 h of BE experiments.

Among various laboratory-scale metal-oxide catalysts for catalytic CO_2-to-FA conversion, Sn-oxides have attracted considerable attention because their structures and chemical compositions could be strategically modified to achieve desirable catalytic performance for formate/FA formation.[176] The Chen

group employed a thin-film catalyst by simultaneous electrodeposition of Sn^0 and SnO_x on a Ti electrode and achieved an up to 8-fold higher PCD and 3-fold higher FE for CO_2 conversion to FA than those of the Sn foil counterparts.[257] Meyer and co-workers used SnO_2 nanocrystals with a high surface area to carry out the eCO_2RR to formate at η as low as ∼340 mV in aqueous $NaHCO_3$ solution.[258] The size of the SnO_2 NPs could significantly influence the FE and CD. When the CB support was replaced by graphene with a higher surface area, an FE of >93% and a CD of 10.2 mA cm^{-2} at −1.8 V vs. SCE were achieved with good stability for 18 h. Won and co-workers investigated how the native O-content can be used as a selectivity descriptor in the eCO_2RR and hence a hierarchical Sn dendrite electrode (SnO_x/Sn) was synthesized with high O-content, consisting of a multi-branched conifer-like structure with an enlarged surface area.[259] The reduced Sn electrode with abundant O-species, which survived under highly reductive conditions, effectively stabilizes a $CO_2^{\bullet-}$ intermediate rather than a bare Sn surface and exhibited a superior formate production rate of 228.6 μmol h^{-1} cm^{-2} at −1.36 V vs. RHE without any considerable catalytic degradation over 18 h of operation. Finally, in order to explain the importance of oxide layers on top of the Sn electrode, Zhang et al. deliberately removed the oxide layer via etching followed by exposing the etched Sn electrode to the air over 24 h as a control.[260] The electrochemical results indicated that, while the Sn electrode with a native oxide layer exhibited a higher CO_2 reduction activity towards formate (FE ∼84% and CD ∼3.8 mA cm^{-2}), the activity decreased for the etched Sn electrode (FE ∼43% and CD ∼5.2 mA cm^{-2}). Meanwhile, it has been observed that

1224 | Energy Environ. Sci., 2021, **14**, 1194–1246

This journal is © The Royal Society of Chemistry 2021

the catalytic performance of the SnO_x electrode was restored with an enhancement of 1.5-fold in the CD (FE $\sim 85\%$ and CD ~ 5.5 mA cm^{-2}) when exposed to air compared to that for an untreated Sn electrode because the etching treatment made the electrode surface rough, thus creating a larger active surface area. To further justify the role of metal oxides in improving the performance of the eCO$_2$RR for practical applications, Broekmann and co-workers utilized potential and time-dependent *operando* Raman spectroscopy to monitor the structural change involving reduction of a SnO_2 NP catalyst to metallic tin.[261] This reduction, in fact, resulted in a decreased FE for the production of formate at cathodic potentials where Sn^{IV} was reduced to metallic Sn^0. Subsequently, to obtain detailed mechanistic insight into the electrochemical reduction of CO$_2$ on Sn electrodes in real time, Baruch *et al.* employed *in situ* attenuated total reflectance infrared (ATR-IR) spectroscopy.[262] The working electrode was a Sn film deposited onto a ZnSe crystal using ion beam sputtering and the crystal was mounted into a custom-made three-electrode cell. Using the IR spectro-electrochemical (IR-SEC) technique, 2e$^-$ reduction of the electrode from a native SnO_2 NP layer to a meta-stable Sn^{II}-oxyhydroxide ($Sn_6O_4(OH)_4$) species occurred under electrolysis conditions. The IR-SEC data indicated that this species then reacted with CO$_2$ to form a surface-bound carbonate, followed by transfer of 2e$^-$/1H$^+$ to form formate, which was then released from the surface to regenerate the Sn^{II}-oxyhydroxide (Fig. 40).

From the discussions thus far, the potential of SnO_x materials is clear for the selective production of FA. Metals in the liquid state can form a thin oxide layer when exposed to air. Although room temperature fabrication of 2D metal-oxides through gas-injection and water dispersion has been demonstrated, analogous processes in non-aqueous solvents at elevated temperatures remain challenging. The Hu group reported the mass-production of free-standing amorphous 2D SnO_x nanoflakes with Bi decoration from a liquid Sn–Bi alloy by controlled exposure to oxygen in well-selected hydroxyl-rich non-aqueous solvents.[263] The resulting 2D SnO_x offered a high FE of $>99\%$ for the eCO$_2$RR to FA and stable performance over 10 h. This work demonstrated how a liquid metal can form a thin layer of oxide skin *via* exposure to oxygen and the hydroxyl-rich solvents exhibit the best morphology
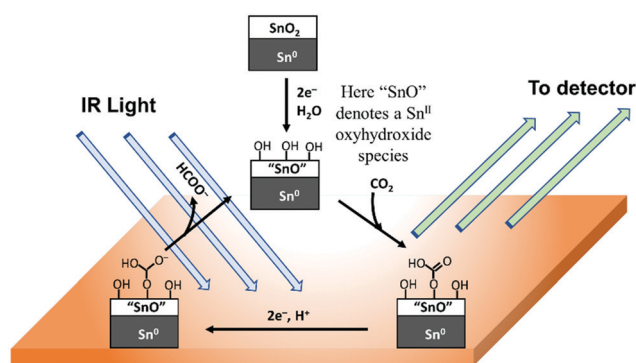
control toward 2D SnO_x through strong and stabilizing solvent–oxide interactions with the liquid metal-oxide surface of the nanoflakes. After the success of hierarchical 2D SnO_x electrodes with high surface area for selective formation of formate with high performance, Li *et al.* extended this idea to synthesize 3D hierarchical mesoporous SnO_2 NSs on carbon cloth (CC) to efficiently carry out CO$_2$-to-FA conversion in aqueous media.[264] The electrode, fabricated by a facile combination of hydrothermal reaction and calcination, exhibited an unprecedented PCD of ~ 45 mA cm^{-2} at η close to 880 mV with an FE of 87% and long-term stability. This superior performance may be attributed to the robust and highly porous hierarchical structures, providing a large surface area to facilitate charge and mass transfer.

While the influence of oxide layers and/or the oxide content on Sn electrodes has been discussed thoroughly in ameliorating the performance as well as selectivity of formate production during the eCO$_2$RR, other metals and/or their corresponding oxides remain relatively unexplored. To elucidate the roles of non-Sn metals and metal-oxides, Xie *et al.* fabricated two different Co materials of 4-atom-thick layers; one consisting of pure Co and the other with the co-existence of Co and CoO.[265] The surface Co atoms of the atomically thin layers were found to be more reactive than those on the bulk samples for formate production by the eCO$_2$RR at low η. Thus, the exceptional increase of the intrinsic activity by 10 times was observed by the partial oxidation of the atomic layers with a CD of 10.59 mA cm^{-2} over 40 h and 90.1% formate selectivity at $\eta = 240$ mV. These results strongly suggested the importance of the morphology and oxidation state(s) to the catalytic activities. Liu and co-workers recently reported the preparation of and eCO$_2$RR to FA using an In-oxide based catalyst (In_2O_3@C) which was grown on CB by a two-step process of coprecipitation and pyrolysis.[266] In_2O_3@C achieved a maximum FE of 87.6% at -0.9 V *vs.* RHE in aqueous electrolyte and was stable for up to 12 h, outperforming most In-based electrocatalysts.

A new sub-class of metal/metal-oxide based catalysts, termed as oxide-derived (OD) materials, has recently emerged with enhanced activity and selectivity compared to those of the parent bulk materials or NPs, presumably because of the formation of a greater number of highly active grain boundaries. These OD-materials were generally obtained after formation of thick oxide layers, formed through electrochemical oxidation.[235] When OD-Bi films were prepared on Ti substrates *via* electrochemical and thermal oxidation from metallic Bi films by the Bertin group, a significantly higher geometric CD could be observed for OD-Bi ($j = 8.3$ mA cm^{-2}) than that of Bi metal ($j = 1.6$ mA cm^{-2}) only at a 100 mV larger η, although the FEs for both films were almost identical.[267] Lee *et al.* later identified carbon supported BiO_x (BiO_x/C) as a promising and environmentally benign and more economic catalyst for the eCO$_2$RR to formate with an average FE of 93.4% at potentials from -1.37 to -1.70 V (*vs.* Ag/AgCl). A PCD of 16.1 mA cm^{-2} at -1.75 V *vs.* Ag/AgCl could be achieved with a formate production rate of 300 μmol cm^{-2} h^{-1}.[268] Notably, this was the first report where dual mechanisms at different potentials were believed to be operative on BiO_x/C. Specifically, a 2e$^-$/1H$^+$ transfer reaction to adsorbed

Fig. 40 Proposed mechanism for the electrochemical reduction of CO$_2$ to formate on Sn/SnO_x cathodes along with an *in situ* ATR-IR study on the cathode film deposited on a ZnSe ATR crystal *via* the IR-SEC technique.[262]

This journal is © The Royal Society of Chemistry 2021

Energy Environ. Sci., 2021, **14**, 1194–1246 | 1225

CO_2 or a chemical H^+ transfer reaction to CO_2^- anions are the possible RDSs at low potentials, whereas a $1e^-$ transfer reaction to CO_2 is the RDS at high potentials. Recently, Rasul *et al.* prepared OD-Sn and an OD-Sn–Pb–Sn composite for formate production by the eCO_2RR and compared their reactivity to that of the pristine compounds.[269] Their results demonstrate that the pristine Sn electrodes show a higher FE for formate compared to that of the pristine Sn–Pb–Sn alloy (80% *vs.* 66%) at -1.4 V *vs.* RHE. Upon oxidation treatment of pristine Sn and the Sn–Pb–Sn composite, the FEs were improved to 84% and 91%, respectively. This improved performance can be attributed to the presence of a composite metal/metal oxide structure arising from synergistic local geometric and electronic effects of the multi-metallic centers.

3.4.2. Biological and bio-inspired electrocatalysts. Metallo-enzymes found in biological systems are believed to be an ideal model that may inspire catalyst design and CO_2 interconversion to FA/formate is no exception.[270,271] The tungsten (W)-containing formate dehydrogenase 1 (*Sf*FDH1) enzyme from *Syntrophobacter fumaroxidans (Sf)* allows a rapid, reversible and specific eCO_2RR to formate to take place on a freshly polished pyrolytic graphite edge electrode surface (Fig. 41a).[272] *Sf*FDH1 catalyzes this interconversion at thermodynamic potential by the W-center.[273] While thorough mechanistic studies may provide valuable information to aid the design of synthetic analogs, issues in protein handling, their expressions and structural limitations make the W-containing *Sf*FDH1 enzyme intractable for mechanistic studies. Hence, Hirst, Reisner, and co-workers adopted a more versatile and robust experimental set-up by adsorbing the Mo-containing formate dehydrogenase H (*Ec*FDH-H) from the model organism *Escherichia coli (Ec)* on a graphite–epoxy electrode to investigate the catalytic properties (Fig. 41b and c).[274] Under pH 6 at 23 °C, *Ec*FDH-H is a highly active and reversible electrocatalyst with an FE of $\sim100\%$ towards formate formation. This state-of-the-art finding with the Mo-containing enzyme may offer a new paradigm for synthetic catalyst design. With further progress in the field of the bioelectrocatalytic CO_2RR, Sakai *et al.* constructed a gas-diffusion-type biocathode with W-containing FDH, immobilized on a Ketjen black (KB)-modified CC electrode.[275] Since the control
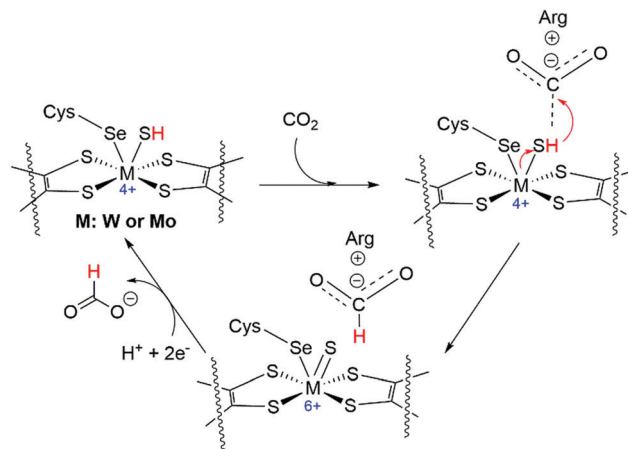

Fig. 42 Plausible reaction mechanism for CO_2 reduction to formate catalyzed by a selenocysteine-containing FDH.[276] The mechanism should be similar for a cysteine-containing FDH.

of the hydrophobicity of the FDH1-absorbed electrode is an important factor in fabricating the gas-diffusion-type cathode system, the hydrophobicity was optimized according to the weight ratio of the PTFE binder to KB. By using the FDH-immobilized KB-modified electrode, cathodic current densities of ~20 mA cm^{-2} could be achieved under mild and quiescent conditions (neutral pH, atmospheric pressure, and RT).

Several review articles have already discussed Mo- and W-containing formate dehydrogenase (FDH) enzymes as a model to understand the mechanistic strategies and vital chemical attributes to design new efficient catalysts.[270,276] For M-containing (M = W, Mo) FDHs, the possible mechanism for CO_2-to-formate was proposed by Moura and co-workers where CO_2 is first trapped by a suitably positioned and positively charged arginine (Arg) residue followed by the attack of an H atom from M–SH to the Arg-trapped CO_2 (Fig. 42).[276] In the 2nd step, the metal is oxidized from +4 to +6 and finally, upon accepting proton and electron equivalents, the active site releases formate and returns to the original state with a +4 oxidation state.
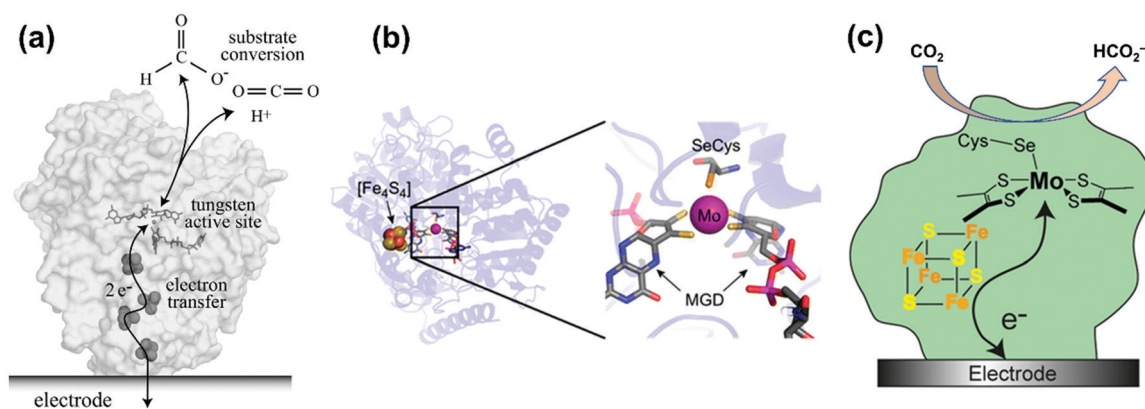

Fig. 41 Schematic representations of the eCO_2RR to formate by (a) W-containing[272] and (c) Mo-containing[274] FDH adsorbed on an electrode surface. (b) Structure of *Ec*FDH-H showing the active site and the [4Fe–4S] cluster that transports electrons to and from the active site in biology.[274]

1226 | *Energy Environ. Sci.*, 2021, **14**, 1194–1246

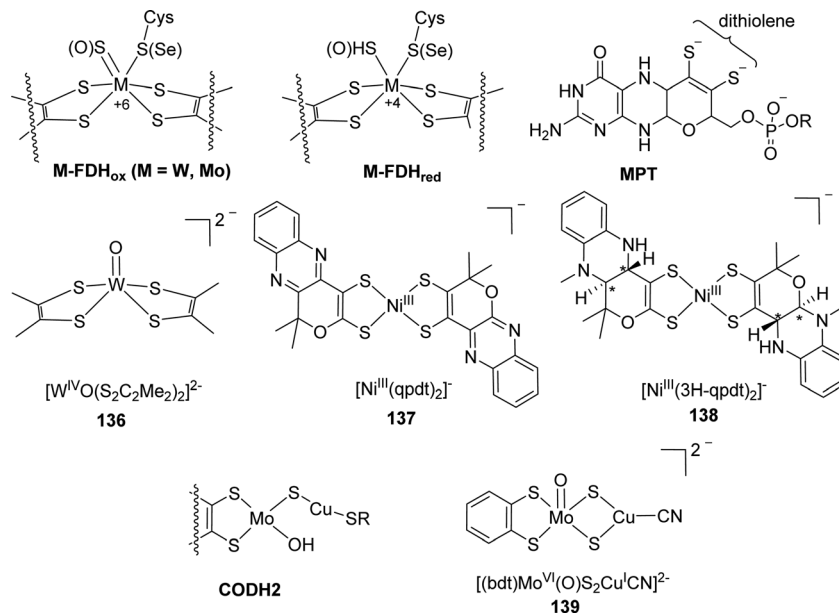This journal is © The Royal Society of Chemistry 2021

Fig. 43 Chemical structures of the biological enzyme active sites and bio-inspired electrocatalysts.

Inspired by the FDH models (Fig. 41b and 43), several dithiolate-based ligands were developed for the development of biomimetic catalysts, as the metal center is stabilized by two redox non-innocent pyranopterin dithiolate groups (MPT) (Fig. 43). Kim and co-workers prepared a biomimetic $W^{IV}=O$ bis-dithiolene complex (**136**) for the gaseous CO_2RR to formate at 90 °C in MeCN (Fig. 43).[277] Although the formate production was not stoichiometric, these results were beneficial for providing insights into the importance of the secondary coordination environment and strategies for synthetic modifications. Li, Fontecave, and co-workers synthesized a Ni-complex $[Ni^{III}(qpdt)_2]^-$ (**137**) containing a NiS_4 motif with two dithiolene ligands mimicking the MPT framework (Fig. 43).[278] The catalytic eCO_2RR to formate as the major product was achieved with small amounts of CO and H_2 on the Hg/Au electrode (not on a GCE (glassy carbon electrode)) and remarkable stability was observed over 23 h of electrolysis with a good overall FE ($\sim 90\%$; $FE_{FA} = 60\%$). Although **137** performs reasonably well, $qpdt^{2-}$ has two major drawbacks. First, it is not fully biomimetic because the central pyrazine ring is oxidized while it is reduced in MPT. Second, the imines of the $qpdt^{2-}$ ligand are prone to hydrogenation. To rectify these issues, the same team thus synthesized hydrogenated models, more biologically relevant to MPT and more stable.[279] The best catalytic performance was obtained for derivative **138** with the reduced imine bond after hydrogenation (Fig. 43). **138** served as the active catalyst for the eCO_2RR to formate with an FE of 70% and 300 mV overpotential with negligible H_2 generation.

To mimic the active site of CO-dehydrogenase (CODH2) (Fig. 43) to catalyze CO oxidation to CO_2 with three sulfur coordination instead of four (as seen in FDH) around the central metal (Mo) of the active site along with 2nd metal Cu, the Mougel and the Fontecave groups prepared a heterobimetallic Mo–Cu active site, $[(bdt)Mo^{VI}(O)S_2Cu^ICN]^{2-}$ (**139**; Fig. 43). Mo and

Cu are bridged *via* two μ_2-sulfides with the MPT fragment to mimic the benzenedithiolate (bdt) ligand to chelate Mo (Fig. 41).[280] The reactivity of complex **139** has a close resemblance with FDH to catalyze the eCO_2RR with an FE of 75% for formate generation. IR-SEC and DFT studies revealed a plausible mechanism where the catalytic species is generated *via* $2e^-$ reduction of **139** in the presence of CO_2, triggering the transfer of the oxo moiety to CO_2 to give CO_3^{2-}, and another $1e^-$ reduction. Even though this work established the crucial role of the presence of Cu^I for the catalytic activity, the detailed functions and interactions between the two metal centers are awaiting further investigation.

3.4.3. Molecular complexes. Metal alloys and oxides have shown remarkable activities towards FA formation, but they suffer in most cases due to the initial formation of $CO_2^{\bullet-}$ at very large negative potentials. While the use of bio(inspired)-catalysts is sometimes advantageous because of their low thermodynamic potentials for catalytic turnover, they are difficult to express, purify and handle. Therefore, molecular catalysts might be logical alternatives because of their propensity to act as a bridge between these systems. Highly active transition metal complexes are promising candidates to overcome challenges associated with metal, oxide, and bio(inspired)-catalysts.[166,170,180,281,282] Because of the well-defined structures of molecular complexes, fine-tuning of the chelating abilities as well as the steric, electronic and electrostatic effects of the ligand framework is conceivable, thus opening opportunities towards further mechanistic and spectroscopic studies. In analogy to CO_2 hydrogenation catalysts, in some cases, metal hydride intermediates may play an essential role during CO_2 insertion to produce formate/FA selectively. Such metal hydride species should not readily react with protons to produce H_2 and/or polarize the C–O bond toward C–O bond cleavage, ultimately producing CO as the end-product, under electrochemical conditions.

This journal is © The Royal Society of Chemistry 2021

Energy Environ. Sci., 2021, **14**, 1194–1246 | 1227

The Yang group has demonstrated that Pt-complexes [Pt(dmpe)$_2^{2+}$] (**140**) and [Pt(depe)$_2^{2+}$] (**141**) (depe: 1,2-bis(diethylphosphino)-ethane) showed both thermodynamic and kinetic control over metal hydrides for the eCO$_2$RR to formate with high selectivity.[172,283] A rapid protonation pathway followed by the exergonic C–H bond forming reaction of the hydride with CO$_2$ may be responsible for the high selectivity. This reasoning was validated experimentally when these catalysts were shown to produce formate selectively upon the eCO$_2$RR in MeCN with an FE of >90% at η < 100 mV without catalyst degradation.

In homogeneous CO$_2$ hydrogenation, various Ir pincer-based complexes have been reported to undergo CO$_2$ insertion into the Ir–H bond to afford Ir–formate complexes/intermediates. Two dihydrido Ir(III) pincer complexes were employed as electrocatalysts by Meyer, Brookhart and co-workers for a homogeneous eCO$_2$RR (Fig. 44).[284] (POCOP)IrH$_2$(MeCN) (**142**) gave an FE of 85% for formate in a MeCN/H$_2$O (95:5) mixture at −1.45 V vs. NHE with a rate constant (k_{cat}) of 20 s^{-1} without CO. Only a small amount of H$_2$ evolution was observed from the background reduction of water as this active complex was unreactive towards water. However, the role of water was very pronounced in this system to serve as a proton donor to generate OH$^-$ to further react with CO$_2$ to form HCO$_3^-$. With a slight modification, another Ir complex, (POC′OP)IrH$_2$(MeCN) (**143**), with an ammonium functional group was designed (Fig. 44).[285] **143** was shown to limit the HER to ca. 7% and thus to allow the use of water as the solvent. Surprisingly, upon addition of 1% MeCN into the aqueous buffer, the over-potential was reduced, and **143** achieved an FE of 93% for formate production at −1.41 V vs. NHE with a CD of 0.6 mA cm^{-2} for 24 h of the CPE experiment. Mechanistic studies suggested MeCN to be an essential ancillary ligand that ionizes formate effectively to prevent catalyst deactivation. It was also noted that the catalytically active Ir–H intermediates exhibited only modest hydricity to prevent the reaction with water to give H$_2$. Hazari, Palmore, and co-workers further used their hydrogenation catalyst **44** for the eCO$_2$RR in 12% H$_2$O–MeCN under 1 atm CO$_2$ (Fig. 44).[286] An FE of >99% to formate was obtained at an onset potential of −1.5 V vs. Fc/Fc$^+$. However, the observed k_{cat} of 0.56 s^{-1} was much lower than that of **142** (k_{cat} = 20 s^{-1}). Mechanistic studies revealed that the formate elimination from the metal–formate adduct is kinetically difficult, although the CO$_2$ insertion into the Ir–H bond occurs readily.

Unlike Ir, there were hardly any rhodium-based electrocatalysts reported to date that can selectively reduce CO$_2$ to HCOOH until the work reported by Turro and co-workers.[287] The reported Rh$_2$(II,II) complexes contained two electron-rich deprotonated 6-methyl-2-hydroxypyridine (mhp) bridging ligands and two electron-accepting diamine chelating ligands made of either 1,10-phenanthroline (phen) or dipyrido[3,2-f:2′,3′-h]quinoxaline (dpq) for **144** and **145**, respectively (Fig. 44). Electrochemical results showed that selective CO$_2$-to-FA conversion was achieved with **144** but not **145**, for which a small amount of H$_2$ was observed under similar experimental conditions. In spite of their nearly identical electronic and atomic structures around the Rh$_2$ core, these two complexes exhibited strikingly different reductive catalysis. These findings highlighted the importance of ligand-based reduction events close to the active metal center(s) to either serve as an electron reservoir and/or to tune the hydricity of the Rh$_2$–H (formed as an intermediate) bond to promote CO$_2$ insertion. Moreover, the protonation of the dpq ligand after its reduction may make that electron unavailable for subsequent catalysis at the metal center. Other than Rh, another 2nd row transition metal complex, PN^3-Ru (**146**), was investigated for the eCO$_2$RR in a 3% H$_2$O–MeCN mixture (Fig. 44). However, unlike Ir-pincer complexes, even though the HER was suppressed, the selectivity for FA was moderate (FE$_{FA}$ = 37.3%) with substantial formation of CO (FE$_{CO}$ = 60.7%) at −1.28 V (vs. SHE).[288]

Development of molecular catalysts based on 1st row earth-abundant transition metals for CO$_2$ electroreduction has been a thriving area since the discovery that [Ni(cyclam)]$^{2+}$ (cyclam: 1,4,8,11-tetraazacyclotetradecane) (**147**) catalyzed the eCO$_2$RR-to-formate in DMF in the late 80s by Collin et al.[289] These studies have revived enormously in recent years and stimulated new results.[170] The Berben group has investigated metal–metal clusters with delocalized bonding within the metal core and electron delocalization extending out to electron withdrawing CO ligands for the eCO$_2$RR.[290] An Fe-carbonyl cluster containing an interstitial nitride, [Fe$_4$N(CO)$_{11}$L]$^-$ (**148**), was found to show poor selectivity towards formate in the presence of a weak acid in MeCN, but good formate selectivity over H$_2$ at a pH of 5–13 in aqueous buffer and in MeCN/H$_2$O (95/5 v/v) (Fig. 45).[291,292] The highest efficiency was observed in the neutral buffer reaching a CD up to 4 mA cm^{-2} with an FE of 96% and a TOF of 106 h^{-1}. Electrolysis experiments as long as 27 h were realized without CO formation,
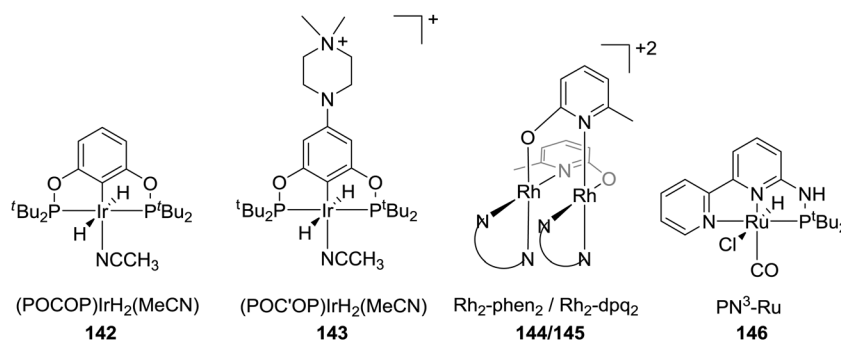

Fig. 44 Various electrocatalysts for selective electrochemical reduction of gaseous CO$_2$ to formate.

1228 | Energy Environ. Sci., 2021, **14**, 1194–1246

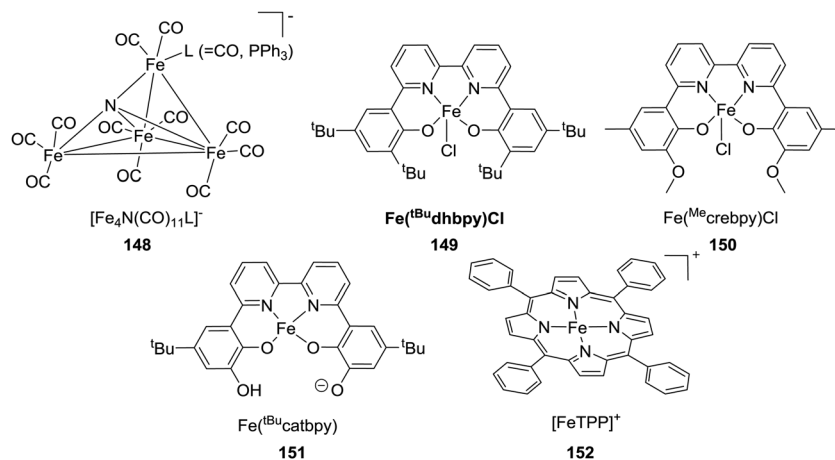This journal is © The Royal Society of Chemistry 2021

Fig. 45 Fe-based molecular electrocatalysts for selective reduction of CO_2 to formate.

decay in the CD or decomposition of the electrocatalyst, indicative of the exceptional stability. Interestingly, replacing one of the CO ligands with a weaker π-accepting PPh_3 group resulted in a significant drop in formate selectivity from 96% to 61%.[290]

Non-innocent redox-active ligands were often employed to achieve exceptional reactivities. Schiff base ligands with a tetradentate κ^4-N_2O_2 coordination framework have been commonly used as catalyst platforms because they are electron-rich, synthetically accessible, and amenable to chirality at the metal center with a judicious ligand design. Machan and co-workers synthesized Fe complex **149** (Fig. 45), utilizing a 6,6′-di(3,5-di-*tert*-butyl-2-hydroxybenzene)-2,2′-bipyridine (^{tBu}dhbpy[H]$_2$) ligand framework. **149** was found to be catalytically competent for the eCO_2RR to formate with an FE of 68% for up to 10 h of electrolysis in the presence of 0.5 M phenol (PhOH) as a proton source at -2.5 V *vs.* Fc/Fc$^+$.[293] A small amount of H_2 (FE$_{H_2}$ = 30%) along with only trace CO (FE$_{CO}$ = 1.1%) was detected to reach mass balance. Mechanistic studies indicated that the phenoxide (PhO$^-$) moieties coordinated to Fe were sensitive to protonation in the reduced state, suggesting the possibility of cooperative pendent proton interactions being involved in the CO_2 reduction. Intrigued by these observations, other ligand derivatives, (^{Me}crebpy[H]$_2$) and (^{tBu}catbpy[H]$_4$), containing pendant 2nd sphere H-bond donor (–OMe) and acceptor (–O$^-$) groups were employed for complexes **150** and **151**, respectively (Fig. 45).[294] By tuning the ability of the secondary sphere moiety to direct the exogenous sacrificial proton donor PhOH to the proton-sensitive Fe-bound O atom, an increased CD for formate production ($j_{HCO_2^-}$) and selectivity for formate were achieved. While a 3.3-fold enhancement of the CD with an FE of 85% was observed for **150** in comparison to that of **149**, for **151**, the CD increment was only 1.2-fold with no significant increase in FE (*ca.* 71%), suggesting that the strength of interaction between the external proton donor and the pendant relay site has a nuanced effect on the reaction control. Overall, these results indicated that the improved performance in both activity and selectivity for the –OMe derivative arises from the beneficial interactions between the secondary sphere moieties, exogenous H$^+$ donor, and inner-

sphere Fe-bound O atom, which collaboratively contribute to the preconcentration of the H$^+$ donor and kinetic selectivity.

Fe porphyrin (Fe-porp) complexes have been extensively studied in the field of the homogeneous eCO_2RR as they are efficient and robust in the low-oxidation state. However, it is noteworthy that these complexes are prone to produce CO as the only product in organic medium.[295,296] Nocera and co-workers judiciously adopted an approach to introduce an external tertiary amine ligand to FeTPP (TPP = tetraphenyl-porphyrin) (**152**) in the presence of a weak proton donor to drive the reduction of CO_2 to formate from Fe(0)TPP with a moderate selectivity of *ca.* 70% (Fig. 45). In contrast to those conventional CO_2-to-formate generating organometallic systems that involve the initial formation of M–H species followed by CO_2 insertion, this system preferentially forms an initial Fe–CO_2 adduct followed by subsequent protonation. The advantage of such a protonation mechanism is to avoid the HER and produce formate with enhanced selectivity. The presence of the tertiary amine appears to increase the basicity of CO_2 bound to the Fe center, allowing for its protonation, and facilitated dissociation of formate, consistent with a *trans* effect. Thus, the results open an alternative route for an unexplored CO_2-to-formate conversion mechanism and shed light on the role of the *trans* effect in redirecting the eCO_2RR from CO to formate.

Robert, Lau and co-workers studied the eCO_2RR with $[CoN_5]^{2+}$ (N_5 = 2,13-dimethyl-3,6,9,12,18-pentaazabicyclo-[12.3.1]octadeca-1(18),2,12,14,16-pentaene) (**153**) and obtained exclusive CO formation in DMF (Fig. 46).[297] Intriguingly, the selectivity was completely changed to FA without CO when the central metal Co was replaced by Fe in $[FeN_5Cl_2]^2$ (**154**). Experimental results along with DFT calculations revealed that, in the case of the Co–CO_2H intermediate, π-back-bonding from the electron-rich, formally Co^{II} center to π^* orbitals of CO_2 would weaken the C–O bond and hence facilitate its cleavage to give the CO product.

Roy *et al.* designed a family of Co-based catalysts, $[CpCo(N^R_2P^{R'}_2)L]^{n+}$ (L = I, MeCN; $N^R_2P^{R'}_2$: 1,5-diaza-3,7-diphosphacyclooctane) possessing four different $N^R_2P^{R'}_2$ ligands with cyclohexyl or phenyl substituents on phosphorus

This journal is © The Royal Society of Chemistry 2021

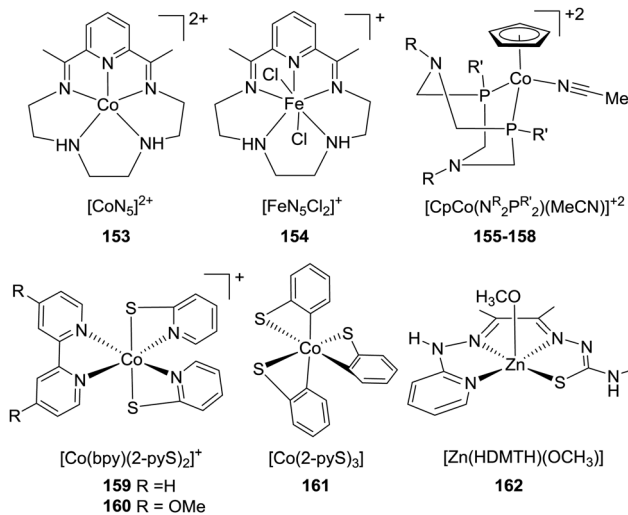*Energy Environ. Sci.*, 2021, **14**, 1194–1246 | 1229

Fig. 46 1st row transition metal-based electrocatalysts for selective reduction of gaseous CO_2 to formate.

(P^{Cy} or P^{Ph}) and benzyl or phenyl substituents on nitrogen (N^{Bn} or N^{Ph}) (**155**: R=Ph, R'=Cy; **156**: R=Ph, R'=Ph; **157**: R=Bn, R'=Cy; **158**: R=Bn, R'=Ph) (Fig. 46).[298] These complexes were found to be very efficient for the eCO_2RR towards FA with very high selectivity (FE = 90 ± 10%) at moderate overpotentials of 400–600 mV in DMF. An outstanding TOF of >1000 s^{-1} was observed for **157**, likely due to the presence of the most electron-donating phosphine and basic amine groups among all 4 complexes. Mechanistic studies suggested that while the intramolecular pendant amines were not involved in the direct proton transfer to CO_2, they help to stabilize key intermediates through H-bonding interactions with water molecules in the hydride transfer step.

With an idea of making the eCO_2RR more energy efficient by reducing the overpotential, Fontecave, Mougel, and co-workers synthesized two variants of (bpy)bis(2-pyridinethiolato)Co(III) complexes (**159–160**) which were identified as highly active and selective catalysts for formate production (Fig. 46).[299] The selectivity for formate production reached 57% with a TOF of 27.5 s^{-1} for **159** at −1.83 V *vs.* Fc/Fc^+, and 64% with a TOF of 29.5 s^{-1} for **160** at −1.98 V *vs.* Fc/Fc^+, respectively. These results indicate that the introduction of the electron-donating −OMe group on the bpy moiety does not significantly increase the rate and selectivity of the reaction despite driving the operating potential to more negative values. Furthermore, when the bpy ligand was replaced by 2-pyridinethiolate (**161**), a TOF of 178 s^{-1} was achieved but at the cost of a highly negative cathodic potential, making the overall reaction less energy efficient (Fig. 46). Benchmarking of these complexes including previously reported molecular catalysts allowed complex **159** to stand among the best reported CO_2-to-FA catalysts, achieving a TOF of 10 s^{-1} at an η of 110 mV only, which is the lowest value reported so far.

Reduction of the metal center in the 1st step of the catalytic cycle and subsequent formation of catalytically active metal-hydride species are the common steps found within almost all the molecular electrocatalysts discussed here during the eCO_2RR where metal centered catalysis is considered. Furthermore, saturated CO_2 solutions are required for these complexes to obtain meaningful catalysis, which may prevent them from being used for practical purposes. Grapperhaus and co-workers have designed a redox-inactive zinc-based complex, [Zn(HDMTH)(OCH₃)] (DMTH = diacetyl-2-(4-methyl-3-thiosemicarbazonate)-3-(2-pyridine-hydrazonato)) (**162**), for converting CO_2 from air to formate as the only C1 product, although the FE for formate production was unsatisfactory (*ca.* 15.1% based on the total charge) (Fig. 46).[300] It is noteworthy that this complex utilized metal–ligand cooperativity and redox-active ligands to sequester and activate CO_2 without being reduced and this may serve as a new strategy to mitigate the CO_2 issue if the performance can be uplifted dramatically.

3.4.4. Immobilized complexes/composites/hybrid materials/metal-free catalysts. Substantial catalytic activities of several molecular catalysts in the homogeneous phase motivated researchers to study the same reactivity under heterogeneous electrocatalytic conditions in aqueous media as an alternative and promising approach to further enhance the selectivity and stability of the catalytic system to new heights. In doing so, molecular catalysts are usually immobilized onto electrode or conductive surfaces by attaching a linker to the ligand as depicted in Fig. 47. Rational immobilization designs may also tackle several pre-existing issues, such as high η, applied voltage, and energy consumption, related to conventional electrochemical reduction processes. Isaacs *et al.* achieved the eCO_2RR to FA with electro-polymerized cobalt tetra-aminophthalocyanine (CoTAPc) at an onset potential of −1.0 V *vs.* Ag/AgCl on a GCE.[301] Zhao *et al.* later developed a composite of multi-walled carbon nanotubes (MWCNTs) and CoTAPc to give single and/or multiple layers using layer-by-layer (LBL) assembly onto positively charged indium tin oxide (ITO) or a graphite electrode (GE), ITO-(MWCNT/CoTAPc)$_n$ and GE-(MWCNT/CoTAPc)$_n$ (n = 1–5) (Fig. 47a).[302] The best performance for eCO_2R was obtained for the GE-(MWCNT/CoTAPc)₅ composite modified electrode at a peak potential of $\sim$−0.5 V *vs.* Ag/AgCl. FA was identified as the only detected product in the catholyte with a production rate of 21.0 mg L^{-1} h^{-1} and an FE of 73.5% even after 4 h of continuous electrolysis under CO_2 at the peak voltage. In contrast to the reactivity of the CoTAPc only modified electrode, both the current and FA production rate were increased by approximately 20% and 100%, respectively, for the MWCNT/CoTAPc composite modified electrode. It was proposed that the π–π interaction between the phthalocyanine ring of CoTAPc and the sidewalls of MWCNTs reduced the electron density around the Co nuclei in CoTAPc, which expanded the macrocyclic conjugated structure of CoTAPc, and further decreased η for CO_2 reduction.

Reisner *et al.* installed a pyrene unit in the bpy arm of [MnBr(2,2′-bpy)(CO)₃] (**87**) to immobilize the complex on a CNT electrode.[303] Unlike the above-mentioned multilayer formation, only single layers were generated in this case with varied catalyst concentrations. While the Mn-modified CNT electrode favored the formation of formate under fully aqueous conditions at a low Mn-catalyst loading, CO was produced upon increasing the
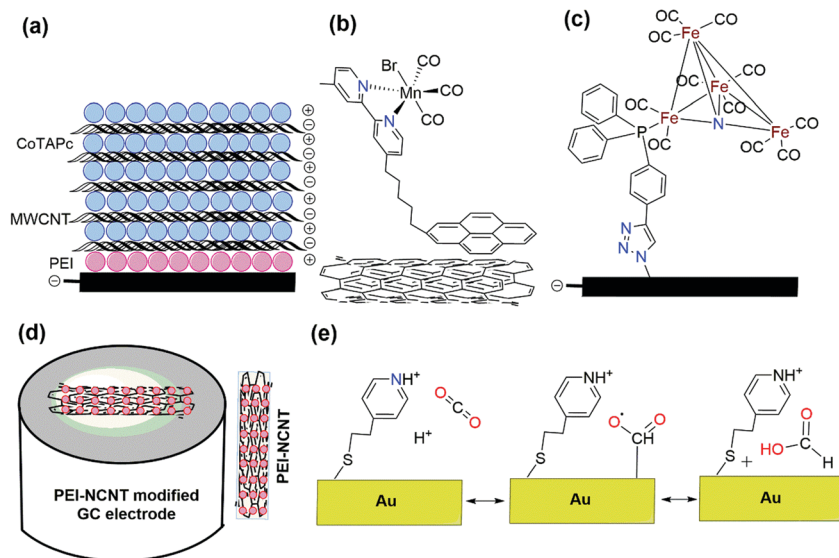
1230 | *Energy Environ. Sci.*, 2021, **14**, 1194–1246

This journal is © The Royal Society of Chemistry 2021

Fig. 47 Schematics of various catalysts immobilized on modified electrode surfaces reported for electrochemical reduction of CO_2 to FA: (a) GE–(MWCNT/CoTAPc)$_n$;[302] (b) pyrene functionalized Mn-modified CNTs;[303] (c) alkyne-terminated [Fe$_4$N(CO)$_{12}$]$^-$ on azide functionalized GC;[304] and (d) PEI–NCNT/GC.[307] (e) Proposed formate formation mechanism for the 4-PEM-modified Au electrode.[308]

catalyst loading (Fig. 47b). The TON for this hybrid electrode reached up to 3920 for formate at an overpotential of 590 mV *vs.* SHE, albeit with a low FE. These observations suggest that the selectivity of the eCO$_2$RR products is sensitive to the surface loading of the catalysts. In a similar fashion, the Berben group has modified complex **148** with a terminal alkyne to use azide alkyne cycloaddition to immobilize the complex onto an azide-terminated GC electrode to further increase the stability of the catalyst (Fig. 47c).[304] Indeed, during the CPE experiment with the modified electrode, no degradation was observed for at least 4 days. An FE of 75 ± 20% and a TON of 52 500 were achieved at −1.25 V *vs.* SCE in a pH 9 buffer.

Using the inherent surface activity of NCNT, Zhang *et al.* deposited SnO$_2$ on NCNT to form a composite, which has been further used to modify a GCE (SnO$_2$-NCNT/GCE).[305] In comparison to the electrode without SnO$_2$ (NCNT/GCE), both electrodes were capable of reducing CO$_2$ electrochemically to formate in CO$_2$ saturated 0.1 M KHCO$_3$ aqueous solution, but SnO$_2$-NCNT/GCE has much higher activity. At −0.9 V *vs.* Ag/AgCl, an FE of 46% was obtained for SnO$_2$-NCNT/GCE, but an FE of only 10% was reached for NCNT/GCE. Li *et al.* prepared a novel Bi-MWCNT-COOH/Cu catalyst *via* a facile co-electrodeposition technique on Cu foil to selectively electrocatalyze CO$_2$ reduction to produce FA.[306] The as-prepared electrodes exhibited high catalytic activity, stability and selectivity toward the production of FA. FE$_{FA}$ could reach values up to 91.7% at −0.76 V *vs.* RHE, with no obvious degradation after 12 h of continuous electrolysis. The presence of an inherently conjugated-conductive body with an H-bonded sequence served as effective catalytic centers for the eCO$_2$RR.

Similar to the work reported by Zhao *et al.* (*vide supra*) on PEI and MWCNT modified electrode surfaces,[302] the Meyer group employed PEI as a co-catalyst on top of a metal-free N-doped CNT (PEI–NCNT) to conduct the eCO$_2$RR to formate.[307] This strategy unlatches a new avenue for the metal free eCO$_2$RR.

During the stepwise electrode fabrication, the homogeneous CNT suspension was first spin coated on a GC electrode followed by nitrogen doping to afford NCNT/GC. Finally, a PEI overlayer was applied to NCNT/GC by dip-coating to procure the PEI–NCNT/GC electrode (Fig. 47d). NCNT/GC is an effective electrocatalyst for CO$_2$-to-formate, and the use of additional PEI reduced the overpotential by 200 mV with higher FE and CD for formate production. An FE of 85% for formate could be achieved with a steady-state CD of 7.2 mA cm^{-2} in CPE experiments at −1.8 V *vs.* SCE for 24 h in aqueous buffer.

Inspired by the aforementioned seminal work on metal-free catalysis, Coskum *et al.* reported an all-organic, metal-free electrocatalyst polydopamine (PDA) that, when immobilized on large-surface, sponge-type carbon felt, achieved impressive performance with a geometric CD of 18 mA cm^{-2} at a 210 mV overpotential for CO (minor) and formate production for continuous 16 h of operation with an FE of >80%.[309] In this particular conjugated polymer based electrocatalyst (PDA), hydrogen bonded motifs have been observed, similar to those in enzymes. Interestingly, PDA shows a lower η than those of state-of-the-art formate selective elcetrocatalysts (*e.g.* 0.5 V for Ag at 18 mA cm^{-2}) on the carbon-based nonmetallic carrier cathode. As the field of metal-free eCO$_2$RR catalysis is flourishing, Flake and co-workers have taken advantage of the Au–S interaction to modify a blank gold electrode with monolayers of thiol-tethered ligands such as 2-mercaptoproponic acid (2-MPA), 4-pyridylethylmercaptan (4-PEM) and cysteamine (CYS) to drive the eCO$_2$RR.[308] Remarkably, Au electrodes modified with 4-PEM showed a 2-fold increase in the FE and 3-fold increase in formate production relative to the best results with untreated Au foil in 0.1 M KHCO$_3$ buffered at pH 6.8 (Fig. 47e). Conversely, electrodes with 2-MPA showed an FE of nearly 100% towards the HER, while CYS-modified electrodes showed a 2-fold increase in both the CO and H$_2$ production. A proton-induced desorption

mechanism was proposed for the 4-PEM modified Au. At the same time, the inability of the other two electrodes to produce significant formate was believed to be associated with the pK_a of the surface-tethered functional groups. These results illustrate that the product selectivity of the eCO_2RR may not always be governed by the electrodes, and/or electrolytes.

After all these discoveries, several groups were working relentlessly in exploring high-performance composite materials containing other non-metals besides carbon. The Wang group first used 2D nonmetallic black phosphorus nanosheets (BP NSs) as a substrate for the eCO_2RR to FA with a maximum yield rate of 22.7 cmol dm^{-3} h^{-1} and an FE of 25.8% at -1.3 V $vs.$ RHE.[310] To conquer the low-performance and enlarge the electrochemical applications of BP NSs, BP NSs were prudently utilized as the catalyst support to load metals by electrodeposition to fabricate an electrodeposited Bi dendrite/BP NS composite (ED-Bi dendrite/BP NS). This composite achieved the highest FA production rate of 440 ηmol dm^{-3} h^{-1} and an FE of 92% at a lower potential of -1.0 V $vs.$ RHE, both significantly higher than those of ED-Bi dendrites without BP NSs. These observations suggest that BP NSs are a promising substrate to fabricate metal composite catalysts for improving CO_2 electroreduction.

3.5. Design of the electrolytic cell/reactor

In addition to the aforementioned factors and parameters, reactor design is another indispensable facet that often helps to improve the overall cell performance, particularly by increasing the PCDs, FEs, and stability. The reactions occur in the electrolytic cell owing to the difference between the imposed external voltage and the open-circuit potential of the cell. With the invention and subsequent progression of CO_2 reduction, different cell designs have been evolved and modified accordingly depending on the specific needs.[311,312] In this section, only those cells will be discussed in detail that primarily produce FA as the main product over other CO reduction products. In this regard, the electrolytic cells can be categorized into H-type cells, bench-scale continuous reactors, undivided fixed-bed reactors, flow cell reactors, $etc.$

To date, commercially available or customized H-type cells are still the most common and well-known lab-scale reactor for the eCO_2RR, in which the working and reference electrodes are placed in the cathodic compartment while the counter electrode is placed in the anodic compartment (Fig. 48a). These two compartments are then connected through a channel (showing a typical "H" form) and separated by an ion-exchange membrane to prevent the reduction products from getting oxidized during electrolysis. CO_2 gas is continuously flowed into the cathodic segment via a glass frit and then delivered into a gas chromatograph (GC) to detect the gas products. In contrast, liquid products are collected from the electrolyte after the electrolysis process and detected using NMR or HPLC. Compared to gaseous products, the FEs for liquid products such as FA are low. Hence, the electrolysis time at constant potential together with the volume of the cell should be increased to reach detection limits of HPLC or NMR. The Koper group has used a custom-made H-type cell with two compartments separated by Nafion 115 where $Pd_{70}Pt_{30}/C$ NPs were loaded on a carbon substrate for the eCO_2RR.[247] The maximum PCD of 5 mA cm^{-2} could be achieved with an 88% FE at a 400 mV overpotential. In 2016, Wang and coworkers investigated the eCO_2RR using a series of electrodeposited Sn catalysts on Cu film with controlled deposition current density in an H-type three-electrode cell (Fig. 48a).[313] The maximum FE_{FA} was 91.7% at -1.4 V $vs.$ SCE with an initial
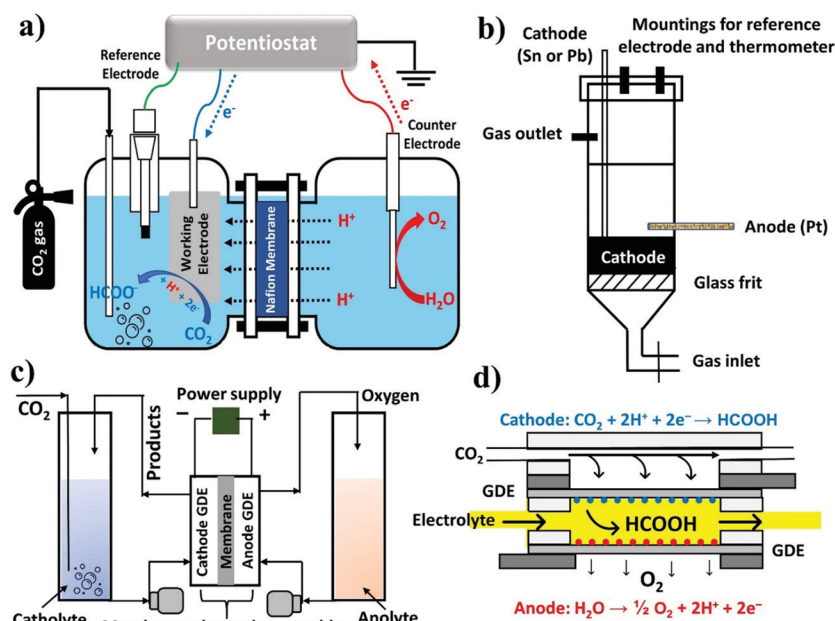

Fig. 48 Schematic diagrams of (a) the conventional H-type electrochemical cell, (b) undivided fixed-bed reactor, (c) liquid phase flow cell consisting of an MEA and (d) microfluidic reactor for CO_2 conversion to FA/formate.

CD of ~ 0.9–1.4 mA cm^{-2} in aq. KHCO$_3$ solution saturated with CO$_2$. With the progression of the electrolysis time, the reaction current exhibited a slow but continuous decrease, and the FE dropped to 81.6% after 2 h. When the experiments finished after 3 h, CD decreased to 0.7 mA cm^{-2} with an FE$_{FA}$ of 69.6%. The degradation of the Sn electrode with a concomitant decrease in performance is likely due to the formation of an alkali metal intermetallic during long period electrolysis. Despite wide utilization, H-cells with metal plate electrodes often suffer from serious drawbacks including limited surface area, large inter-electrode distance and poor cell performance and are not optimized for full-cell operation. In general, an H-type cell is a suitable batch reactor for catalyst screening and product quantification. However, for further industrial applications, efficient cells with lower resistance and higher mass transfer efficiency are essential.

To overcome these shortcomings, rectangular-type reactors were introduced that can extend the electrode surface within a small cell volume and reduce the inter-electrode gap in order to minimize ohmic losses. Initially, Yamamoto *et al.* examined the eCO$_2$RR in a rectangular cell with an increased electrode surface area (4 cm^2) and relatively small inter-electrode gap (1–2 mm).[314] Although syngas was the primary CO$_2$ reduction product at the cathode along with O$_2$ evolution at the anode, the design idea of a rectangular-type reactor was implemented for subsequent development in FA production. Oloman's group reported the eCO$_2$RR in a laboratory bench-scale continuous reactor with the co-current flow of reactant gas and catalyte liquid through a fixed-bed cathode of 30$^{\#}$ mesh tinned-copper.[315] This set-up could alleviate the CO$_2$ solubility constraint, generating formate as the primary product; however, unsatisfactory η and rapid deterioration of the cathode encouraged the development of other cell designs. While most CO$_2$ reduction to FA using metal plate electrodes has been conducted in divided H-cells, Köleli *et al.* proposed to use an undivided fixed-bed reactor to reduce CO$_2$ at Pb and Sn granules, aiming to extend the geometric surface area as much as possible within a relatively compact electrochemical cell volume with a small electrode gap and high faradaic efficiencies (Fig. 48b).[188]

For the eCO$_2$RR to become an industrially feasible and profitable process, batch electrochemical cells should be upgraded to flow cells that could attain >100 mA cm^{-2}, surmounting the mass transfer limitations of an H-cell by continuously circulating the reactants and products. Moreover, the gas-phase eCO$_2$RR is feasible within a flow cell to conquer CO$_2$ solubility issues and product recycling from the aqueous phase. Even the thermodynamics and kinetics of the eCO$_2$RR within flow cells are fundamentally different compared to H-type cells. In 2013, Wu *et al.* reported a design of a full electrochemical flow cell featuring a buffer layer of circulating liquid-phase electrolyte.[316] Incorporation of the buffer with an electrolyte significantly enhanced the formation of formate, suppressing H$_2$, which was predominant in the absence of the buffer. FE$_{max}$ toward formate was >90% at −1.7 V *vs.* SHE with a PCD of 9 mA cm^{-2} when the anode was fed with H$_2$. When H$_2$ was replaced with 1 M KOH solution, FE$_{max}$ toward formate was

85% at −2.0 V with a PCD of 6 mA cm^{-2}. This study proved that the circulating buffer enables the production of formate at an η of 200 mV regardless of the gaseous or aqueous reactants at the anode. Polymer electrolyte membrane (PEM) flow cells, closely related to proton exchange membrane fuel cells (PEMFCs), are one of the most explored class of CO$_2$ flow cells, which utilize a membrane electrode assembly (MEA), developed from fuel cell systems.[218,312,317,318] The MEA, a vital component of the cell, consists of a PEM, cathode GDE, and anode GDE where the electrodes are separated to prevent the contamination of products but are in close proximity to decrease the cell resistance (Fig. 48c).

Although formate production has been extensively studied with MEA reactors, particularly with Sn electrocatalysts, the obtained current density was inadequate for scalable technology.[225,315,316,319] Very recently, Lee *et al.* reported a facile strategy of a catalyte-free MEA flow cell using vaporized CO$_2$ gas as a reactant where a significantly high formate concentration of 41.5 g L^{-1} has been obtained at 343 K with a high PCD of 51.7 mA cm^{-2} and FEFA of 93.3% *via* continuous operation in a full flow cell at a low cell voltage of 2.2 V.[320] Interestingly, the catalyte-free eCO$_2$RR using a GDE with commercial Sn NPs showed higher activity compared to the 1.0 M KCl catalyte-added system. Meanwhile, He and co-workers realized the utility of a buffer layer in proton exchange membrane reactors (PEMRs).[321] It was suggested that a buffer layer helps to ensure sufficient cathode potential, which is essential to CO$_2$ activation. Notably, the cathode potential could not break through the threshold in the conventional PEMR without a buffer layer due to a large portion of potential consumption on the PEM. While when using commercial Sn with a GDE a PCD of 150 mA cm^{-2} with 60% current efficiency could be achieved within 0.5 h of electrolysis in 0.5 M KHCO$_3$ buffer solution, the efficiency dropped to only 5% without the buffer layer. Although the previous examples of using MEA or PEMRs for FA/formate production have been proved beneficial, the corrosive nature of FA towards the membrane during long-term electrolysis can be a major concern that ultimately impedes commercial use.[322] However, a large scale MEA cell was prepared by Oloman's group where a geometric surface of 320 cm^2 for a Sn-based GDE with a concomitant j_{FA} of 195 mA cm^{-2} could be attained.[323] For a superficial j of 0.6–3.1 kA m^{-2}, the formate current efficiencies varied from 91 to 63% for the applied reactor voltage of 2.7–4.3 V, which produced up to 1 M formate in the catalyte product from a single pass. Unfortunately, a gradual decrease of the catalytic activity was also observed after 100 min of operation, likely due to formate crossover through the Nafion 117 membrane. Moreover, additional operating costs would be required for this kind of large cell, which typically operates at 600 kPa and 325 K. The examples discussed in this review typically use CO$_2$ either as a gas or dissolved in aqueous media for cathodic reduction. Unfortunately, both the feedstocks encounter challenges when CO$_2$ electrolyzers are scaled up for pilot plant and/or industrial operations to produce chemicals and fuels. While aqueous CO$_2$ offers significantly low solubility precluding CO$_2$ from reaching the cathode for

This journal is © The Royal Society of Chemistry 2021

Energy Environ. Sci., 2021, **14**, 1194–1246 | 1233

the reaction, gaseous CO_2 feedstocks require strikingly high energy for purification and pressurization to achieve meaningful rates of product formation. To circumvent these issues, the Berlinguette group has used liquid bicarbonate feedstocks that can deliver high concentrations of CO_2 to the cathode for CO_2-to-FA conversion.[324] Although electrochemical reduction of bicarbonate into formate was firmly established by the Hori[325] and Kanan[240] groups, their activities were not noticeable. On this front, the Berlinguette group has designed a continuous flow cell fitted with a BPM and a Bi cathode electrocatalyst supported on CP where bicarbonate solutions (3.0 M $KHCO_{3(aq)}$), forming CO_2 upon reacting with H^+ at the catalyst interface, can be converted into formate at a CD of 108 mA cm^{-2} (FE $\sim$64%). This result has been benchmarked and compared with the state-of-the-art performance of gaseous-fed CO_2 electrolyzers. In spite of the significant progress in the field of flow cells, further research is necessary in ameliorating the cathode lifetime, reducing formate crossover and optimizing the reactor for the eCO_2RR to FA production.

Most of the aforementioned electrolytic cells, designed on the basis of fuel cells, utilize a PEM as the electrode (cathode and anode) separator. More recently, a state-of-the-art concept of the microfluidic flow cell (MFC) for the eCO_2RR was first modeled and propounded by the Kenis group where a flowing electrolyte stream, instead of an ion exchange membrane, is used to separate the cathodes and anodes (Fig. 48d).[326] This MFC configuration separates the oxidation and reduction products by diffusion and not by the membrane. Microfluidics is a powerful technique and offers a high surface-to-volume (S/V) ratio along with efficient heat and mass transfer rates. Hence, leveraging the benefits of microfluidics to address existing energy and environmental issues would be propitious. In 2010, Kenis reported the fabrication of an MFC as a versatile analytical tool for an efficient eCO_2RR to FA using different catalysts and operating conditions, notably different pH values (pH 4–10). Furthermore, the cell, consisting of a Sn coated GDE, serves as an effective reactor with significantly high efficiencies (FE $\sim$89% and energetic efficiency $\sim$45%) and PCDs on the order of 100 mA cm^{-2}, pH 4 being the most effective. But lower pH was deliberately avoided because Sn dissolves in a highly acidic medium. In addition to Sn catalysts, a BiOBr catalyst has already been shown by the Sargent group to exhibit good eCO_2RR activity in an H-cell configuration but limited by mass transport phenomena (*vide supra*).[227] To this end, BiOBr was deposited onto a GDE carbon electrode, which thereby achieved high formate selectivity (over 90%) with a PCD as high as 200 mA cm^{-2} in an MFC configuration, showing the distinct advantages and importance of gas-phase reactors over liquid-phase reactors.

Although it is evident from the discussions above that the design of the electrochemical cells and/or reactors for CO_2-to-FA conversion is one of the principal parameters which has seen significant surveillance in the past two decades, the application of the eCO_2RR is still in a laboratory research stage. Despite the low CO_2 solubility and mass transfer limitations causing low current densities, H-type cells (liquid phase) are being tremendously used, which provide fundamental lessons

for catalyst development in a flow cell (gas-phase) system. In order to obtain a high current density with enhanced long-term stability, further development of flow cells would be necessary, which can be a future gateway of the eCO_2RR towards industrial application at a large scale. Besides, there are still some other determining factors related to flow cells such as the channel length, flow rate of the CO_2 stream, anode materials and catalysts, easy separation of products, purity of the inlet gas, *etc.* that seek immediate attention for developing CO_2 electrolyzers, particularly for the R&D sector.

3.6. Towards practical systems for electrochemical FA production

The ultimate goal is to develop the means to construct cheap, scalable and energy efficient systems for the eCO_2RR.[327–330] This will enable the wide scale adoption of this technology and a significant contribution towards carbon utilization towards value added products such as formic acid.[331,332] Thus far, we have covered a range of significant advances in the eCO_2RR, which have been accomplished by tuning reactions conditions such as the system, solvent/electrolyte, operating pressure, pH, electrode, and catalyst. Thus far in the literature, these conditions have been independently optimized. However, in the actual system, these are likely to be coupled and have an effect on each other. It is therefore crucial that the relationship between these conditions be considered, to guide future optimization and design efforts. Of the most commonly employed configurations for the eCO_2RR as covered in the previous section, MEA systems offer the highest energy efficiencies due to the 'zero-gap' configuration, leading to lower ohmic losses.[333,334] In addition, various engineering approaches have shown that an MEA system can be used to produce pure liquid product solutions.[185,186] These factors highlight the MEA as the system of choice for future practical and large-scale application of the technology. This is analogous to proton exchange membrane (PEM) electrolyzer systems for hydrogen production,[335] which have been successfully commercialized. To enable high current density, MEA systems used for the eCO_2RR typically are catholyte-free, relying on the ion exchange membrane as the medium for ion transport to/from the catalyst.[320,333] In such systems, the choice of catholyte is thus not a reaction condition that can be optimized. As for the anolyte, aqueous media are most commonly used to facilitate water oxidation to liberate oxygen.[331] There has also been interest to replace water oxidation with organic oxidation reactions in order to reduce the energy requirements of the overall process and also to generate valuable products. Good recent examples in the literature include the partial anodic oxidation of glycerol and ethylene.[336–338] Reports involving high pressure setups involving flow cell/MEA systems for the eCO_2RR have been rare.[339,340] In theory, such systems should enable the maximum possible availability and transport of the CO_2 reactant to the catalyst. As a result, this can likely translate to unprecedented current density and selectivity. Furthermore, work by Sinton and co-workers showed that pressurization up to 10 bar enables system tolerance towards significant amounts of O_2 impurities that are expected to be present in typical

1234 | *Energy Environ. Sci.*, 2021, **14**, 1194–1246

This journal is © The Royal Society of Chemistry 2021

flue gas.[341] As a result, such high-pressure gas diffusion-based systems have strong motivation for future development and are an avenue for intense research.

Under conditions of high current density in gas-diffusion systems, it is expected that the local pH at the electrode surface will become highly alkaline.[342] However, the high concentration of OH$^-$ can react with CO$_2$ and form carbonate, which gives rise to two crucial issues. (1) Consumption of CO$_2$ feedstock, thus limiting CO$_2$ conversion yields. (2) Decreased CO$_2$ reactant available for CO$_2$ conversion. Thus, future research efforts should focus on solving the carbonate issue. Promising reaction directions to solve this include the use of an acidic electrolyte or development of efficient bipolar membranes.[343,344] As for the design of catalyst materials, the majority of studies in the literature test their catalysts predominantly in traditional H-cells rather than using gas diffusion electrodes. However, there is a concern about how readily catalysts optimized under 'H-cell' conditions translate into practical MEA device systems. For example, in the fuel cell community, catalysts designed for the oxygen reduction reaction in an H-cell do not perform as well in the actual device.[345] Thus, moving forward, catalyst testing and design should be carried out in gas diffusion systems. Finally, with regards to the electrode, it is crucial that designs can last for a long period of continuous operation (>10 000 h and beyond). An important aspect of the gas diffusion system is the three-phase region, made possible by the hydrophobic support. Thus, future research should focus on optimizing this three-phase region and prevention of flooding by maintaining the hydrophobicity of the support. It is also crucial to increase single pass efficiencies, thus increasing CO$_2$ conversion yields.[346] Finally, there should also be a focus on scaling up (Fig. 49a)[343] and developing electrolyzer cell stacks (Fig. 49b),[347] towards the future practical application of this technology.

4. Economic analysis of formic acid synthesis from CO$_2$

4.1. General background

Conventionally, FA is mainly manufactured using the following four resource-intensive and high carbon footprint methods: (1) methyl formate hydrolysis, (2) oxidation of hydrocarbons, (3) hydrolysis of formamide, and (4) preparation of free FA from formates.[348] Method 1 is the most common route, which is based on a two-stage process (eqn (8) and (9)). The carbon emission of the conventional method is around 2.2 kg$_{CO_2}$ kg$_{FA}^{-1}$.

$$CO + CH_3OH \rightarrow HCOOCH_3 \quad (8)$$

$$HCOOCH_3 + H_2O \rightarrow CH_3OH + HCOOH \quad (9)$$

FA is mainly used in textiles, pharmaceuticals and food chemicals, due to its strong acidic nature and reducing properties.[348,349] The current market price of 95% grade FA is around $600–$1000 per ton, and the global production in 2019
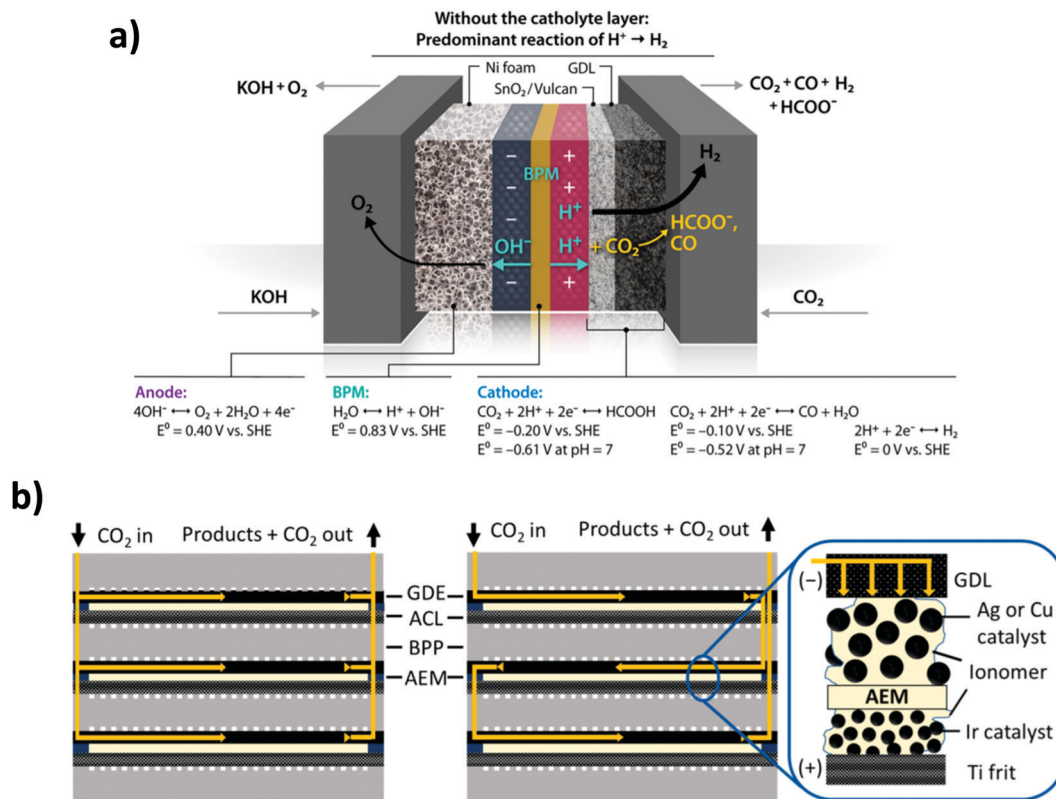

Fig. 49 (a) Schematic of a larger scale (25 cm^2 active area) CO$_2$ electrolyzer for production of formic acid.[343] (b) Illustration of an electrolzyer cell stack for electrochemical CO$_2$ conversion.[347]

This journal is © The Royal Society of Chemistry 2021
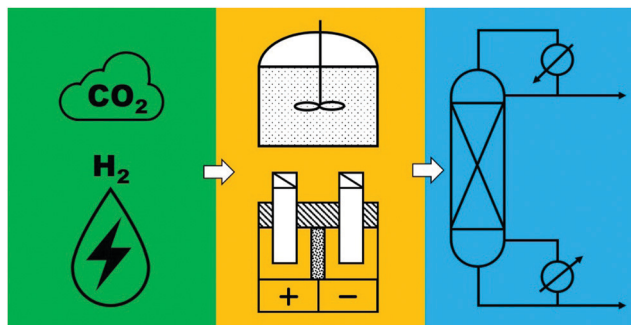
Energy Environ. Sci., 2021, 14, 1194–1246 | 1235

Fig. 50 A general CCU process for converting CO_2 to formic acid.

was estimated to reach 1.015 megatonne with a projected annual growth of 1–3%.[350] However, this market prediction has not considered the application of FA as a hydrogen energy carrier. Under such a perspective, the size of demand could reach a multi-gigatonne scale in order to achieve a meaningful capacity for renewable energy storage and utilization.[329] FA synthesis from CO_2 requires both CO_2 capture and utilization (CCU) processes, which can be split into three steps: (1) capture of CO_2 and generation of H_2 by electrolysis, (2) utilization *via* CO_2 hydrogenation or the eCO_2RR to formic acid, and (3) final FA product purification, as illustrated in Fig. 50.

For the carbon capture step, the mature technology is amine scrubbing. Many other methods are also under development, including adsorption from flue gas, direct air capture, chemical looping, membrane separation, cryogenic separation, *etc.* The cost for amine scrubbing is around \$37–121 $ton_{CO_2}^{-1}$,[351–353] but, by using membrane technologies, it has the potential to reduce to \$25 $ton_{CO_2}^{-1}$.[353,354] To achieve low carbon emission, electrolysis of water is the most common way in addition to the direct eCO_2RR. If in the utilization step the CO_2 hydrogenation approach is used, both CO_2 and H_2 may need purification to avoid catalyst poisoning, and compression to reach the reaction pressure. On the other hand, if an eCO_2RR method is employed, water can feed directly as a reactant and H_2 generation in the capture step is not necessary. Thus, as we discussed in the last two sections, for the utilization process, three synthetic routes can be employed for consideration: (1) homogeneous catalysis and (2) heterogeneous catalysis for CO_2 hydrogenation, and (3) the eCO_2RR using renewable electricity, although the maturity of all these methods is still at technology readiness levels (TRLs) of 3–5.

Comparatively, the hydrogenation process is more developed than electrochemical reduction, although two pilot-scale electrochemical reduction plants were demonstrated by Det Norske Veritas (DNV) and Mantra Venture Group.[349,355–357] Thermodynamically, FA synthesis from CO_2 and H_2 has a positive Gibbs energy of 32.9 kJ mol^{-1}. Therefore, controlled by chemical equilibrium to improve the yield, it is required to conduct the reaction either under a high pressure of more than 100 bar, and/or under basic conditions to form formate. As discussed earlier, homogeneous catalysts have high reactivity and selectivity, but the process requires one to recover the catalyst from the product stream. In this sense, heterogeneous catalysts are more

advantageous, but their reactivity and selectivity are typically lower. Electrochemical reduction can be carried out under mild conditions, and it can be further directly coupled with renewable electricity from solar and wind power plants. While the cost of renewable energy can be as low as 2 cents kW^{-1} h^{-1}, currently high FEs can only be realized under very low FA concentrations in the product stream. Therefore, a significant amount of energy may be required to purify FA to reach the application requirements. In this regard, distillation is the most common purification method. As FA has a very close boiling point to water, an amine is often used as an extraction agent and regenerated through a reactive distillation process, but it is still an energy-intensive step since the amine forms an azeotrope with FA.

4.2. Life cycle assessments

Several economic analyses and life cycle assessments (LCAs) of the CDU (carbon dioxide utilization) to FA process have been reported in the literature. As most of these studies are based on laboratory scale experimental data to estimate the process parameters, attention should be paid to the technical gaps between the laboratory and industrial processes in terms of the production scales. Nevertheless, these studies have shed light on different aspects and helped to identify the most important issues for future studies to focus on.

Pérez-Fortes *et al.* conducted the first comprehensive techno-economic analysis of the CDU to FA process.[349] In their model, CO_2 is captured by amine scrubbing as a worst-case scenario and H_2 is generated from water electrolysis. The FA production is conducted by homogeneous catalysis using a Ru- or phosphino-based catalyst *via* the formation of an amine–FA adduct based on data from a patent,[358] and the final product is purified to 85 wt% through reactive distillation. The net present value (NPV), a metric to evaluate the profitability, was positive when the FA price was higher than €$_{2014}$1700 per ton, which is approx. twice the current market price. However, the carbon footprint (CF) of only 0.166 kg_{CO_2} kg_{FA}^{-1} is much lower than that from the conventional FA process. Notably, the major cost is the high price of the Ru catalyst. When the price of consumables (including catalysts) is decreased by a factor of 6 (achieved by future R&D), with renewable electricity, the price to make CDU to FA profitable is close to the current market reference. Realizing the high catalyst expense and the heavy energy requirement during purification, Kim and Han further studied and compared two proposed processes.[359] Process A is similar to that by Pérez-Fortes, but process B uses an Au/TiO_2 catalyst, to replace the more expensive Ru system, and an amine-shift process to break the azeotrope to save the purification energy. Process design simulations showed that process B increased the energy efficiency by 24.3% and reduced CO_2 emission to 0.3 kg_{CO_2} kg_{FA}^{-1}. However, process B has a much longer process time, which results in a slightly higher cost than that of process A. Aldaco *et al.* combined a dynamic LCA with economic analysis to explore the potential transition from carbon capture and sequestration (CCS) to CCU.[360] The CCU process used here was again similar to what was studied by Pérez-Fortes.[349] It was

1236 | *Energy Environ. Sci.,* 2021, **14**, 1194–1246

This journal is © The Royal Society of Chemistry 2021

found that while CCS yields a greater reduction in CO_2 emissions than those of CCU scenarios and the conventional FA production processes, CCU offers better economic potential and lower fossil consumption, especially when powered by renewable electricity.

Sadhukhan and co-workers considered the integration of the CDU to FA process with a bioelectrochemical system (BES) for wastewater treatment.[361] The BES unit removes the chemical oxygen demand of wastewater and generates CO_2 and electricity. The liberated CO_2 is electrochemically reduced to FA in the CCU process. The economic analysis suggests that the production cost of FA will be around €$_{2018}$500–1500 per ton. While the purification cost was not considered in this study, the process is valuable because of the integrated framework combining wastewater treatment and energy production. Baena-Moreno et al. evaluated the CCU process using CO_2 captured from biogas containing 40% CO_2 and 60% methane.[362] A membrane technology is used for CO_2 capture. H_2 is generated from water electrolysis by a renewable electricity source. Similar to other analyses, FA is produced by homogeneous catalysis and purified by reactive distillation to reach 85 wt%. The economic analysis shows that at the production scale of 1000 m^3 h^{-1}, the FA price is still high at €1767 per ton. Again, the major cost in this study is the catalyst, accounting for 56% of the annualized costs.

Rumayor et al. evaluated the carbon footprint (CF) of different FA production processes using the LCA method.[363] Even if H_2 is produced by steam-reforming of methane, the CF of H_2 will be 1.7 kg$_{CO_2}$ kg$_{H_2}^{-1}$, and the total CF of the chemical catalysis process will be 0.26 kg$_{CO_2}$ kg$_{FA}^{-1}$. The CF of the electrochemical reduction process is heavily influenced by the FA concentration at the outlet of the electrolyzer. At a concentration of 1.68, 10 and 20.5 wt%, the CFs are 31.9, 5.3 and 1.6 kg$_{CO_2}$ kg$_{FA}^{-1}$. It is thus concluded that a minimum of 21 wt% FA concentration at the outlet of the electrolyzer is required to achieve an equivalent CF to that of conventional FA production by reducing the energy demand for purification. Han et al. also conducted a cradle-to-gate life cycle assessment of the CCU process and its comparison to conventional FA production.[364] The assessment is based on two parameters: climate change and fossil resource depletion (FD). Employing CO_2 captured from flue gas and even H_2 produced by water electrolysis using electricity from a fossil-fuel power plant to conduct the catalysis under a pressure of 180 bar and 40 °C, it was found that, compared to the conventional process, this CCU process is able to reduce the CO_2 emissions by 53.6% and FD by 28.3%. Baena-Moreno et al. considered CO_2 reduction into different C1 chemicals including formic acid, carbon monoxide, methanol and methane.[362] They determined the reduction of global warming and fossil depletion impacts based on 1 kg of hydrogen. The results show that reduction to formic acid can achieve the highest environmental impact reduction regardless of whether hydrogen is supplied by fossil-based processes or by water electrolysis. Similarly, Thonemann and Pizzol evaluated the environmental impact of twelve CO_2 conversion technologies (carbon monoxide, FA, methanol, methane, ethanol, dimethyl ether, dimethyl carbonate, dimethoxymethane, Fischer–Tropsch products, and polyols).[365] They identified that in both the near and long-term scenarios FA production

may provide the highest potential to relieve the global warming impact.

Thonemann and Shulte studied the environmental impact of the eCO$_2$RR to FA under super critical CO_2 conditions.[366] It was found that on the laboratory scale, the median of the global warming index (GWI) is extremely high at 9325 kg$_{CO_2}$ eq kg$_{FA}^{-1}$, but the GWI value can be reduced to the range of −0.4 to 6.5 kg$_{CO_2}$ eq kg$_{FA}^{-1}$ if the process is scaled-up. In fact, a recent analysis from Fust Energy suggested that approx. 4 kW h is needed to produce 1 kg of FA by the eCO$_2$RR at a rate of 1 ton$_{FA}$ h^{-1}.[367] Although a well-established H_2 production (from H_2O) electrolyzer of 1 MW can cost ∼$1.2 million, their estimation suggests that the CO_2-to-FA conversion reactor will cost at least 25% more due to the more complex design. Therefore, a total investment or capital expenditure (CAPEX) of ∼$7 million was estimated considering proper handling, storage, and separation. For the electro-catalytic CO_2-to-FA conversion process, the prices of CO_2 and electricity are one of the important factors, which primarily depend on the location, energy source(s), CCU capacity, consumption rate and scale, etc. The Jiao group described the current market prices for CO_2 and electricity falling in the range of $40–70 per ton$_{CO_2}$ and $30–40 per MW per h, respectively.[328] They also performed an economic analysis of a generalized CO_2 electrolyzer system to produce different carbon products including FA, CO, methanol, ethanol, ethylene, and propanol. The system model includes a CO_2 capture unit, an alkaline water electrolyzer stack and a distillation process. It was identified that CO and formic acid were the only profitable products. It was noted that for FA production the major cost is associated with the distillation process.

Different approaches were also adopted to predict a more accurate estimate for the FA production cost, including discounted cash flow, internal rate of return and net present value. While there is some uncertainty in the CAPEX due to unavailability of commercial electrolyzers for CO_2 reduction to FA, the operational cost (OPEX) can be well-defined ($170–330 per ton$_{FA}$) considering the electricity and CO_2 costs. A simplified relation between the CAPEX and OPEX (eqn (10)) is commonly used to estimate the total cost for FA[368]

$$OPEX = 0.15 \times CAPEX \qquad (10)$$

Assuming an average lifetime of around 15 years for the major equipment, the CAPEX/year can be related to the OPEX, according to eqn (11):

$$CAPEX/year = 0.45 \times OPEX \qquad (11)$$

with the factor of 0.45 obtained from $1/(0.15 \times 15)$.

With continuous progress and development in the field of technology and the substantial changes in the policies related to direct air carbon capture mitigating anthropogenic CO_2 emission, the implementation of more stringent regulations that can reduce the CO_2 price significantly is to be expected in the near future.

This journal is © The Royal Society of Chemistry 2021

Energy Environ. Sci., 2021, **14**, 1194–1246 | 1237

Table 12 Pros and cons of each typical CO_2-to-FA conversion process

Conversion processes	Pros	Cons
Homogeneous catalysis	(1) Catalysts dissolved in the reaction medium, allowing a high degree of interaction with the reactant(s) (2) Superior activity and selectivity (3) The selectivity can be tuned (4) Relatively easier to study/characterize reaction intermediates enabling interpretation of reaction mechanisms	(1) Catalyst and product separation, *e.g.*, formic acid, is difficult (2) Incomplete separation may lead to product (FA/formate) decomposition (3) Catalyst decomposition at high temperatures (4) Not recyclable (5) High pressure and a particular ratio of CO_2/H_2 are needed. (6) Often requires additional base/additives
Heterogeneous catalysis	(1) Easy separation of expensive catalyst and product(s) from the reaction mixture (2) Possible to recycle and reuse (3) Catalysts are generally highly robust and can withstand high temperature without subsequent decomposition and/or degradation (4) Sometimes solvents are not required	(1) Reactivity is poor because the reaction occurs only at the catalysts' surface (2) It often requires high surface area due to limited access of reactants over the surface adsorbed species (3) The selectivity is poor (4) It is challenging to study the catalytic systems; hence, the mechanisms are often unclear. (5) CO_2 hydrogenation to FA requires high pressure and a particular ratio of CO_2/H_2 (6) Often requires additional base/additives
Electrocatalysis	(1) To a certain extent, both the selectivity and activity can be controlled by adjusting the electrode potentials only (2) Catalysis is usually done at room temperature and an atmospheric pressure of CO_2 (3) Renewable electricity can be directly used, *e.g.*, solar, wind, *etc.* (4) Unlike homo- and heterogeneous catalysis, electrocatalysis does not require auxiliary chemicals like H_2 for CO_2-to-FA conversion (5) The set-up is modular and easy to scale up to meet industrial requirements (6) Can be paired with anodic organic oxidation reactions to generate valuable products at both electrodes (7) Allows for distributed small scale production, rather than large scale centralized production of today	(1) Difficult to distinguish different faradaic processes that occur simultaneously (2) A lot of *a priori* known information such as the formation of nanoparticles or other active species (mostly in the case of homogeneous electrocatalysis) should be considered to elucidate reaction mechanisms (3) Difficulty in the separation of liquid products or salts (FA/formate) from the electrolytic solution and/or supporting electrolyte (4) The competing HER often leads to a lowered FE for FA/formate production (5) In most cases, the desired product, FA, is too dilute and not suitable for commercial applications (6) A high purity water source is usually required (7) Long term stability ($>10\,000$ h) has not yet been demonstrated

5. Conclusion and outlook

Energy security and climate change is arguably the most challenging twin problem facing our society. The broad deployment of low-carbon energy generation and distribution systems is a must for our sustainable future. Energy storage and utilization technologies are needed to manage the intermittence of renewable solar and wind energies, to electrify transportation, *etc.* Because of several desirable properties as a liquid fuel, FA has been proposed as a hydrogen energy carrier. The potential application as a fuel may represent a manufacturing scale of multi-gigatonnes per year. However, to enable this potential, practical solutions for FA synthesis by "power to formic acid" need to be developed. In this review, we have discussed and highlighted both homogenous and heterogeneous catalysis for CO_2 hydrogenation as well as systems and catalysts for approaches in the eCO_2RR to FA. The pros and cons of each typical CO_2-to-FA conversion process are summarized in Table 12.

According to the literature LCAs, CDU to FA has great potential to mitigate climate issues, but all the current reaction systems are not yet profitable/practical compared to the conventional FA production process utilizing fossil fuels. The challenges and future improvements to meet the requirement for practical applications are outlined below.

For the CO_2 hydrogenation approaches:

(1) The main issue is the high costs of catalysts. A cost analysis should not be focused on the price of the metal alone; the associated costs of the ligands and supports need to be considered as well. One should also take TONs and TOFs into account using the catalyst price normalized to the TON (CON) and catalyst cost normalized to the TOF (COF) for a meaningful comparison.[12] Based on the preliminary CON analysis on the existing high performance catalysts in Section 2.3, even when assuming a base price of \$600 per ton$_{FA}$ and 90% cost reduction in catalyst preparation (Table 7), most of the CON values are still exceedingly too high for large scale utilization. Hence, fundamental studies on these areas should emphasize the development of economic but highly efficient catalysts.

1238 | *Energy Environ. Sci.*, 2021, **14**, 1194–1246

This journal is © The Royal Society of Chemistry 2021

(2) The use of a base/amine is necessary. Thus, additional energy needs to be invested in the purification step.[349] This issue is unlikely to be resolved for homogeneous systems. An ideal system may involve a gas phase reaction using a heterogeneous catalyst to allow the easy separation of FA by condensation and recycling of unreacted H_2 and CO_2. This process remains unknown, in sharp contrast to the well-developed CO_2 hydrogenation to other oxygenates, but represents great potential to enable large-scale CO_2 hydrogenation to FA.

For the electrochemical reduction methods:

(1) The CAPEX and OPEX analyses suggest that the eCO_2RR to FA could be economically feasible based on the relatively mature water electrolyzer systems and foreseeable savings on low-carbon electricity (*i.e.*, solar) and CO_2. Transition from the lab scale to pilot plant must be demonstrated to identify and tackle the problems about catalyst lifetime, current density, *etc.*

(2) The most pressing issue is the low FA concentration in the product stream, which also requires a considerable amount of energy for purification. Thus, fundamental studies should be focused on improving the FA concentration to at least 21 wt%, along with reducing the cost of catalyst systems. Notably, a pure FA production setup by the eCO_2RR has been recently demonstrated with an innovative cell design.[186] At the same time, integration with solar heat devices for product purification may be further explored.

In summary, very promising and exciting signs of progress in power to FA were witnessed. As Pérez-Fortes and co-workers suggested,[349] once CDU to FA using renewable electricity is workable, it has a market penetration potential of 10–30% in passenger and light commercial fuel cell vehicles, and back-up power supplies in the residential and industrial sectors by the year 2030. However, R&D efforts are required to overcome the challenges discussed above before practical and scalable applications can be realized to create a sizable positive impact on our future energy and environment.

Conflicts of interest

K.-W. H. declares the following competing financial interests: Huang is one of the inventors of EPO Patent No. 3,391,447 B1 "Electricity generation devices using formic acid" assigned to KAUST.

Acknowledgements

References

1 IEA, *World Energy Outlook 2019*, IEA, Paris, 2019.

2 BP, *Statistical Review of World Energy*, London, British Petroleum Co., 2020.

3 IPCC, Fourth Assessment Report, https://www.ipcc.ch/assessment-report/ar4/.

4 N. Mac Dowell, P. S. Fennell, N. Shah and G. C. Maitland, *Nat. Clim. Change*, 2017, **7**, 243–249.

5 S. Chatterjee and K.-W. Huang, *Nat. Commun.*, 2020, **11**, 3287.

6 REN21, Renewables 2020 Global Status Report, Paris, 2020, https://www.ren21.net/reports/global-status-report/.

7 J. A. Turner, *Science*, 2004, **305**, 972–974.

8 P. Moriarty and D. Honnery, *Int. J. Hydrogen Energy*, 2009, **34**, 31–39.

9 P. Moriarty and D. Honnery, *Int. J. Hydrogen Energy*, 2010, **35**, 12374–12380.

10 M. Felderhoff, C. Weidenthaler, R. von Helmolt and U. Eberle, *Phys. Chem. Chem. Phys.*, 2007, **9**, 2643–2653.

11 J. Alazemi and J. Andrews, *Renewable Sustainable Energy Rev.*, 2015, **48**, 483–499.

12 J. Eppinger and K.-W. Huang, *ACS Energy Lett.*, 2017, **2**, 188–195.

13 A. Boddien, C. Federsel, P. Sponholz, D. Mellmann, R. Jackstell, H. Junge, G. Laurenczy and M. Beller, *Energy Environ. Sci.*, 2012, **5**, 8907–8911.

14 M. Grasemann and G. Laurenczy, *Energy Environ. Sci.*, 2012, **5**, 8171–8181.

15 D. Mellmann, P. Sponholz, H. Junge and M. Beller, *Chem. Soc. Rev.*, 2016, **45**, 3954–3988.

16 A. K. Singh, S. Singh and A. Kumar, *Catal. Sci. Technol.*, 2016, **6**, 12–40.

17 J. Hietala, A. Vuori, P. Johnsson, I. Pollari, W. Reutemann and H. Kieczka, in *Ullmann's Encyclopedia of Industrial Chemistry*, Wiley-VCH Verlag GmbH & Co. KGaA, Weinheim, Germany, 2016, pp. 1–23, DOI: 10.1002/14356007.a12_013.pub3.

18 X. Yu and P. G. Pickup, *J. Power Sources*, 2008, **182**, 124–132.

19 C. Guan, Y. Pan, T. Zhang, J. Ajitha Manjaly and K.-W. Huang, *Chem. – Asian J.*, 2020, **15**, 937–946.

20 K.-W. Huang and J. Zheng, Electricity Generation Devices Using Formic Acid, *European Pat.*, EP3391447B1, 2019.

21 EPFL news, https://actu.epfl.ch/news/the-world-s-first-formic-acidbased-fuel-cell/, Accessed 12.06.2020.

22 PHE Centre for Radiation, Chemical and Environmental Hazards: Formic Acid Incident Management 2015.

23 Risk Management Option Analysis Conclusion Document by Ministry of Environment and Water, Bulgaria, 2017, https://echa.europa.eu/documents/10162/745cf276-1065-fa6f-19f3-72c69d16bc84.

24 B. Davis, S. Tsang, P. J. Hall, M. G. Davidson and C. M. Rayner, *A Feasibility Study into the Formic Acid Economy*, EPSRC Grant EP/D023335/1, 2005.

25 W. Leitner, *Angew. Chem., Int. Ed. Engl.*, 1995, **34**, 2207–2221.

26 P. G. Jessop, in *The Handbook of Homogeneous Hydrogenation*, ed. J. G. de Vries and C. J. Elsevier, Wiley-VCH Verlag GmbH & Co., 2007, ch. 17, DOI: 10.1002/9783527619382.ch17.

27 T. Sakakura, J.-C. Choi and H. Yasuda, *Chem. Rev.*, 2007, **107**, 2365–2387.

28 W. Wang, S. Wang, X. Ma and J. Gong, *Chem. Soc. Rev.*, 2011, **40**, 3703–3727.

This journal is © The Royal Society of Chemistry 2021

Energy Environ. Sci., 2021, **14**, 1194–1246 | **1239**

29 M. Aresta, A. Dibenedetto and A. Angelini, *Chem. Rev.*, 2014, **114**, 1709–1742.

30 D. A. Bulushev and J. R. H. Ross, *Catal. Rev.*, 2018, **60**, 566–593.

31 K. Sordakis, C. Tang, L. K. Vogt, H. Junge, P. J. Dyson, M. Beller and G. Laurenczy, *Chem. Rev.*, 2018, **118**, 372–433.

32 Y. Inoue, Y. Sasaki and H. Hashimoto, *J. Chem. Soc., Chem. Commun.*, 1975, 718–719, DOI: 10.1039/C39750000718.

33 Y. Inoue, H. Izumida, Y. Sasaki and H. Hashimoto, *Chem. Lett.*, 1976, 863–864.

34 E. Graf and W. Leitner, *J. Chem. Soc., Chem. Commun.*, 1992, 623–624, DOI: 10.1039/C39920000623.

35 F. Gassner and W. Leitner, *J. Chem. Soc., Chem. Commun.*, 1993, 1465–1466, DOI: 10.1039/C39930001465.

36 E. Graf and W. Leitner, *Chem. Ber.*, 1996, **129**, 91–96.

37 C. Yin, Z. Xu, S.-Y. Yang, S. M. Ng, K. Y. Wong, Z. Lin and C. P. Lau, *Organometallics*, 2001, **20**, 1216–1222.

38 P. G. Jessop, T. Ikariya and R. Noyori, *Nature*, 1994, **368**, 231–233.

39 P. G. Jessop, Y. Hsiao, T. Ikariya and R. Noyori, *J. Am. Chem. Soc.*, 1996, **118**, 344–355.

40 D. Preti, S. Squarcialupi and G. Fachinetti, *Angew. Chem., Int. Ed.*, 2010, **49**, 2581–2584.

41 P. Munshi, A. D. Main, J. C. Linehan, C.-C. Tai and P. G. Jessop, *J. Am. Chem. Soc.*, 2002, **124**, 7963–7971.

42 C.-C. Tai, J. Pitts, J. C. Linehan, A. D. Main, P. Munshi and P. G. Jessop, *Inorg. Chem.*, 2002, **41**, 1606–1614.

43 C. P. Lau and Y. Z. Chen, *J. Mol. Catal. A: Chem.*, 1995, **101**, 33–36.

44 Y. Gao, J. K. Kuncheria, H. A. Jenkins, R. J. Puddephatt and G. P. A. Yap, *J. Chem. Soc., Dalton Trans.*, 2000, 3212–3217, DOI: 10.1039/B004234J.

45 F. Joó, F. Joó, L. Nádasdi, J. Elek, G. Laurenczy and L. Nádasdi, *Chem. Commun.*, 1999, 971–972, DOI: 10.1039/A902368B.

46 F. Joó, G. Laurenczy, P. Kárády, J. Elek, L. Nádasdi and R. Roulet, *Appl. Organomet. Chem.*, 2000, **14**, 857–859.

47 Á. Kathó, Z. Opre, G. Laurenczy and F. Joó, *J. Mol. Catal. A: Chem.*, 2003, **204–205**, 143–148.

48 G. Kovács, G. Schubert, F. Joó and I. Pápai, *Catal. Today*, 2006, **115**, 53–60.

49 J. Elek, L. Nádasdi, G. Papp, G. Laurenczy and F. Joó, *Appl. Catal., A*, 2003, **255**, 59–67.

50 H. Horváth, G. Laurenczy and Á. Kathó, *J. Organomet. Chem.*, 2004, **689**, 1036–1045.

51 C. Federsel, R. Jackstell, A. Boddien, G. Laurenczy and M. Beller, *ChemSusChem*, 2010, **3**, 1048–1050.

52 Y. Himeda, N. Onozawa-Komatsuzaki, H. Sugihara, H. Arakawa and K. Kasuga, *Organometallics*, 2004, **23**, 1480–1483.

53 Y. Himeda, N. Onozawa-Komatsuzaki, H. Sugihara and K. Kasuga, *J. Am. Chem. Soc.*, 2005, **127**, 13118–13119.

54 Y. Himeda, N. Onozawa-Komatsuzaki, H. Sugihara and K. Kasuga, *Organometallics*, 2007, **26**, 702–712.

55 Y. Himeda, S. Miyazawa and T. Hirose, *ChemSusChem*, 2011, **4**, 487–493.

56 J. F. Hull, Y. Himeda, W.-H. Wang, B. Hashiguchi, R. Periana, D. J. Szalda, J. T. Muckerman and E. Fujita, *Nat. Chem.*, 2012, **4**, 383–388.

57 S. Xu, N. Onishi, A. Tsurusaki, Y. Manaka, W.-H. Wang, J. T. Muckerman, E. Fujita and Y. Himeda, *Eur. J. Inorg. Chem.*, 2015, 5591–5594.

58 Y. Maenaka, T. Suenobu and S. Fukuzumi, *Energy Environ. Sci.*, 2012, **5**, 7360–7367.

59 N. Onishi, S. Xu, Y. Manaka, Y. Suna, W.-H. Wang, J. T. Muckerman, E. Fujita and Y. Himeda, *Inorg. Chem.*, 2015, **54**, 5114–5123.

60 K. Muller, Y. Sun and W. R. Thiel, *ChemCatChem*, 2013, **5**, 1340–1343.

61 S. Sanz, M. Benítez and E. Peris, *Organometallics*, 2010, **29**, 275–277.

62 A. Azua, S. Sanz and E. Peris, *Chem. – Eur. J.*, 2011, **17**, 3963–3967.

63 N. Onishi, R. Kanega, E. Fujita and Y. Himeda, *Adv. Synth. Catal.*, 2019, **361**, 289–296.

64 R. Kanega, M. Z. Ertem, N. Onishi, D. J. Szalda, E. Fujita and Y. Himeda, *Organometallics*, 2020, **39**, 1519–1531.

65 R. Tanaka, M. Yamashita and K. Nozaki, *J. Am. Chem. Soc.*, 2009, **131**, 14168–14169.

66 R. Tanaka, M. Yamashita, L. W. Chung, K. Morokuma and K. Nozaki, *Organometallics*, 2011, **30**, 6742–6750.

67 T. J. Schmeier, G. E. Dobereiner, R. H. Crabtree and N. Hazari, *J. Am. Chem. Soc.*, 2011, **133**, 9274–9277.

68 C. A. Huff and M. S. Sanford, *ACS Catal.*, 2013, **3**, 2412–2416.

69 G. A. Filonenko, R. van Putten, E. N. Schulpen, E. J. M. Hensen and E. A. Pidko, *ChemCatChem*, 2014, **6**, 1526–1530.

70 G. A. Filonenko, M. P. Conley, C. Copéret, M. Lutz, E. J. M. Hensen and E. A. Pidko, *ACS Catal.*, 2013, **3**, 2522–2526.

71 G. A. Filonenko, E. J. M. Hensen and E. A. Pidko, *Catal. Sci. Technol.*, 2014, **4**, 3474–3485.

72 J. B. Geri, J. L. Ciatti and N. K. Szymczak, *Chem. Commun.*, 2018, **54**, 7790–7793.

73 H. Li, B. Zheng and K.-W. Huang, *Coord. Chem. Rev.*, 2015, **293**, 116–138.

74 H. Li, T. P. Gonçalves, D. Lupp and K.-W. Huang, *ACS Catal.*, 2019, **9**, 1619–1629.

75 C. Guan, Y. Pan, E. P. L. Ang, J. Hu, C. Yao, M.-H. Huang, H. Li, Z. Lai and K.-W. Huang, *Green Chem.*, 2018, **20**, 4201–4205.

76 Y. Pan, C. Guan, H. Li, P. Chakraborty, C. Zhou and K.-W. Huang, *Dalton Trans.*, 2019, **48**, 12812–12816.

77 T. Schaub and R. A. Paciello, *Angew. Chem., Int. Ed.*, 2011, **50**, 7278–7282.

78 Y.-N. Li, L.-N. He, A.-H. Liu, X.-D. Lang, Z.-Z. Yang, B. Yu and C.-R. Luan, *Green Chem.*, 2013, **15**, 2825–2829.

79 M. Yadav, J. C. Linehan, A. J. Karkamkar, E. van der Eide and D. J. Heldebrant, *Inorg. Chem.*, 2014, **53**, 9849–9854.

80 S. Wesselbaum, U. Hintermair and W. Leitner, *Angew. Chem., Int. Ed.*, 2012, **51**, 8585–8588.

1240 | *Energy Environ. Sci.*, 2021, **14**, 1194–1246

This journal is © The Royal Society of Chemistry 2021

81 J. Kothandaraman, M. Czaun, A. Goeppert, R. Haiges, J.-P. Jones, R. B. May, G. K. S. Prakash and G. A. Olah, *ChemSusChem*, 2015, **8**, 1442–1451.

82 J. Kothandaraman, A. Goeppert, M. Czaun, G. A. Olah and G. K. Surya Prakash, *Green Chem.*, 2016, **18**, 5831–5838.

83 S. Kar, A. Goeppert, V. Galvan, R. Chowdhury, J. Olah and G. K. S. Prakash, *J. Am. Chem. Soc.*, 2018, **140**, 16873–16876.

84 S. Kar, A. Goeppert and G. K. S. Prakash, *Acc. Chem. Res.*, 2019, **52**, 2892–2903.

85 C.-C. Tai, T. Chang, B. Roller and P. G. Jessop, *Inorg. Chem.*, 2003, **42**, 7340–7341.

86 C. Federsel, A. Boddien, R. Jackstell, R. Jennerjahn, P. J. Dyson, R. Scopelliti, G. Laurenczy and M. Beller, *Angew. Chem., Int. Ed.*, 2010, **49**, 9777–9780.

87 C. Ziebart, C. Federsel, P. Anbarasan, R. Jackstell, W. Baumann, A. Spannenberg and M. Beller, *J. Am. Chem. Soc.*, 2012, **134**, 20701–20704.

88 M. S. Jeletic, M. T. Mock, A. M. Appel and J. C. Linehan, *J. Am. Chem. Soc.*, 2013, **135**, 11533–11536.

89 N. Kumar, D. M. Camaioni, M. Dupuis, S. Raugei and A. M. Appel, *Dalton Trans.*, 2014, **43**, 11803–11806.

90 R. Langer, Y. Diskin-Posner, G. Leitus, L. J. W. Shimon, Y. Ben-David and D. Milstein, *Angew. Chem., Int. Ed.*, 2011, **50**, 9948–9952.

91 F. Bertini, N. Gorgas, B. Stöger, M. Peruzzini, L. F. Veiros, K. Kirchner and L. Gonsalvi, *ACS Catal.*, 2016, **6**, 2889–2893.

92 F. Bertini, M. Glatz, N. Gorgas, B. Stöger, M. Peruzzini, L. F. Veiros, K. Kirchner and L. Gonsalvi, *Chem. Sci.*, 2017, **8**, 5024–5029.

93 Y. Zhang, A. D. MacIntosh, J. L. Wong, E. A. Bielinski, P. G. Williard, B. Q. Mercado, N. Hazari and W. H. Bernskoetter, *Chem. Sci.*, 2015, **6**, 4291–4299.

94 A. Z. Spentzos, C. L. Barnes and W. H. Bernskoetter, *Inorg. Chem.*, 2016, **55**, 8225–8233.

95 Y. Zhang, P. G. Williard and W. H. Bernskoetter, *Organometallics*, 2016, **35**, 860–865.

96 Y. M. Badiei, W.-H. Wang, J. F. Hull, D. J. Szalda, J. T. Muckerman, Y. Himeda and E. Fujita, *Inorg. Chem.*, 2013, **52**, 12576–12586.

97 A. Dubey, L. Nencini, R. R. Fayzullin, C. Nervi and J. R. Khusnutdinova, *ACS Catal.*, 2017, **7**, 3864–3868.

98 F. Zhu, L. Zhu-Ge, G. Yang and S. Zhou, *ChemSusChem*, 2015, **8**, 609–612.

99 S. Enthaler, A. Brück, A. Kammer, H. Junge, E. Irran and S. Gülak, *ChemCatChem*, 2015, **7**, 65–69.

100 R. Watari, Y. Kayaki, S.-I. Hirano, N. Matsumoto and T. Ikariya, *Adv. Synth. Catal.*, 2015, **357**, 1369–1373.

101 M. M. T. Khan, S. B. Halligudi and S. Shukla, *J. Mol. Catal.*, 1989, **57**, 47–60.

102 J. C. Tsai and K. M. Nicholas, *J. Am. Chem. Soc.*, 1992, **114**, 5117–5124.

103 W. Leitner, E. Dinjus and F. Gaßner, *J. Organomet. Chem.*, 1994, **475**, 257–266.

104 H. Hayashi, S. Ogo and S. Fukuzumi, *Chem. Commun.*, 2004, 2714–2715, DOI: 10.1039/B411633J.

105 S. Moret, P. J. Dyson and G. Laurenczy, *Nat. Commun.*, 2014, **5**, 4017.

106 C. Fink, S. Katsyuba and G. Laurenczy, *Phys. Chem. Chem. Phys.*, 2016, **18**, 10764–10773.

107 S.-M. Lu, Z. Wang, J. Li, J. Xiao and C. Li, *Green Chem.*, 2016, **18**, 4553–4558.

108 K. Rohmann, J. Kothe, M. W. Haenel, U. Englert, M. Hölscher and W. Leitner, *Angew. Chem., Int. Ed.*, 2016, **55**, 8966–8969.

109 N. Westhues, M. Belleflamme and J. Klankermayer, *ChemCatChem*, 2019, **11**, 5269–5274.

110 A. Weilhard, M. I. Qadir, V. Sans and J. Dupont, *ACS Catal.*, 2018, **8**, 1628–1634.

111 A. Weilhard, K. Salzmann, M. Navarro, J. Dupont, M. Albrecht and V. Sans, *J. Catal.*, 2020, **385**, 1–9.

112 C. Fellay, P. J. Dyson and G. Laurenczy, *Angew. Chem., Int. Ed.*, 2008, **47**, 3966–3968.

113 G. Bredig and S. R. Carter, *Ber. Dtsch. Chem. Ges.*, 1914, **47**, 541–545.

114 M. W. Farlow and H. Adkins, *J. Am. Chem. Soc.*, 1935, **57**, 2222–2223.

115 C. J. Stalder, S. Chao, D. P. Summers and M. S. Wrighton, *J. Am. Chem. Soc.*, 1983, **105**, 6318–6320.

116 H. Takahashi, L. H. Liu, Y. Yashiro, K. Ioku, G. Bignall, N. Yamasaki and T. Kori, *J. Mater. Sci.*, 2006, **41**, 1585–1589.

117 D. Preti, C. Resta, S. Squarcialupi and G. Fachinetti, *Angew. Chem., Int. Ed.*, 2011, **50**, 12551–12554.

118 P. R. Upadhyay and V. Srivastava, *Catal. Lett.*, 2017, **147**, 1051–1060.

119 T. Umegaki, Y. Enomoto and Y. Kojima, *Catal. Sci. Technol.*, 2016, **6**, 409–412.

120 T. Wang, D. Ren, Z. Huo, Z. Song, F. Jin, M. Chen and L. Chen, *Green Chem.*, 2017, **19**, 716–721.

121 Y. Wu, Y. Zhao, H. Wang, B. Yu, X. Yu, H. Zhang and Z. Liu, *Ind. Eng. Chem. Res.*, 2019, **58**, 6333–6339.

122 D. Preti, S. Squarcialupi and G. Fachinetti, *ChemCatChem*, 2012, **4**, 469–471.

123 G. A. Filonenko, W. L. Vrijburg, E. J. M. Hensen and E. A. Pidko, *J. Catal.*, 2016, **343**, 97–105.

124 Q. Liu, X. Yang, L. Li, S. Miao, Y. Li, Y. Li, X. Wang, Y. Huang and T. Zhang, *Nat. Commun.*, 2017, **8**, 1407.

125 J. Su, L. Yang, M. Lu and H. Lin, *ChemSusChem*, 2015, **8**, 813–816.

126 Q.-Y. Bi, J.-D. Lin, Y.-M. Liu, X.-L. Du, J.-Q. Wang, H.-Y. He and Y. Cao, *Angew. Chem., Int. Ed.*, 2014, **53**, 13583–13587.

127 H. Song, N. Zhang, C. Zhong, Z. Liu, M. Xiao and H. Gai, *New J. Chem.*, 2017, **41**, 9170–9177.

128 C. Hao, S. Wang, M. Li, L. Kang and X. Ma, *Catal. Today*, 2011, **160**, 184–190.

129 W. Zhang, S. Wang, Y. Zhao and X. Ma, *Chem. Lett.*, 2016, **45**, 555–557.

130 N. Liu, R. J. Du and W. Li, *Adv. Mater. Res.*, 2013, **821–822**, 1330–1335.

131 N. Liu, J. Lei, M. Y. Li and P. Wang, *Adv. Mater. Res.*, 2014, **881–883**, 283–286.

This journal is © The Royal Society of Chemistry 2021

Energy Environ. Sci., 2021, **14**, 1194–1246 | **1241**

132 K. Mori, T. Taga and H. Yamashita, *ACS Catal.*, 2017, **7**, 3147–3151.

133 C.-S. He, L. Gong, J. Zhang, P.-P. He and Y. Mu, *J. CO2 Util.*, 2017, **19**, 157–164.

134 L. T. M. Nguyen, H. Park, M. Banu, J. Y. Kim, D. H. Youn, G. Magesh, W. Y. Kim and J. S. Lee, *RSC Adv.*, 2015, **5**, 105560–105566.

135 S. Masuda, K. Mori, Y. Kuwahara and H. Yamashita, *J. Mater. Chem. A*, 2019, **7**, 16356–16363.

136 Q. Sun, B. W. J. Chen, N. Wang, Q. He, A. Chang, C.-M. Yang, H. Asakura, T. Tanaka, M. J. Hülsey, C.-H. Wang, J. Yu and N. Yan, *Angew. Chem., Int. Ed.*, 2020, **59**.

137 Z. Xu, N. D. McNamara, G. T. Neumann, W. F. Schneider and J. C. Hicks, *ChemCatChem*, 2013, **5**, 1769–1771.

138 N. D. McNamara and J. C. Hicks, *ChemSusChem*, 2014, **7**, 1114–1124.

139 Y. Kuwahara, Y. Fujie and H. Yamashita, *ChemCatChem*, 2017, **9**, 1906–1914.

140 Y. Zhang, J. Fei, Y. Yu and X. Zheng, *Catal. Commun.*, 2004, **5**, 643–646.

141 Y. Ying-Min, Z. Yi-Ping, F. Jin-Hua and Z. Xiao-Ming, *Chin. J. Chem.*, 2005, **23**, 977–982.

142 Y. Yu, J. Fei, Y. Zhang and X. Zheng, *Chin. Chem. Lett.*, 2006, **17**, 1097–1100.

143 Y.-M. Yu, J.-H. Fei, Y.-P. Zhang and X.-M. Zheng, *Chin. J. Chem.*, 2006, **24**, 840–844.

144 Y. P. Zhang, J. H. Fei, Y. M. Yu and X. Zheng, *Chin. Chem. Lett.*, 2006, **17**, 261–264.

145 Z. Zhang, Y. Xie, W. Li, S. Hu, J. Song, T. Jiang and B. Han, *Angew. Chem., Int. Ed.*, 2008, **47**, 1127–1129.

146 Z. Zhang, S. Hu, J. Song, W. Li, G. Yang and B. Han, *ChemSusChem*, 2009, **2**, 234–238.

147 X. Feng, X. Ding and D. Jiang, *Chem. Soc. Rev.*, 2012, **41**, 6010–6022.

148 A. Nagai, Z. Guo, X. Feng, S. Jin, X. Chen, X. Ding and D. Jiang, *Nat. Commun.*, 2011, **2**, 536.

149 Z.-Z. Yang, H. Zhang, B. Yu, Y. Zhao, G. Ji and Z. Liu, *Chem. Commun.*, 2015, **51**, 1271–1274.

150 K. Park, G. H. Gunasekar, N. Prakash, K.-D. Jung and S. Yoon, *ChemSusChem*, 2015, **8**, 3410–3413.

151 J. J. Corral-Pérez, A. Billings, D. Stoian and A. Urakawa, *ChemCatChem*, 2019, **11**, 4725–4730.

152 G. Gunniya Hariyanandam, D. Hyun, P. Natarajan, K.-D. Jung and S. Yoon, *Catal. Today*, 2016, **265**, 52–55.

153 G. H. Gunasekar, J. Shin, K.-D. Jung, K. Park and S. Yoon, *ACS Catal.*, 2018, **8**, 4346–4353.

154 G. H. Gunasekar, K.-D. Jung and S. Yoon, *Inorg. Chem.*, 2019, **58**, 3717–3723.

155 J. H. Lee, J. Ryu, J. Y. Kim, S.-W. Nam, J. H. Han, T.-H. Lim, S. Gautam, K. H. Chae and C. W. Yoon, *J. Mater. Chem. A*, 2014, **2**, 9490–9495.

156 C. Mondelli, B. Puértolas, M. Ackermann, Z. Chen and J. Pérez-Ramírez, *ChemSusChem*, 2018, **11**, 2859–2869.

157 Y. Zhou, Y. Huang, B. Jin, X. Luo and Z. Liang, *Ind. Eng. Chem. Res.*, 2019, **58**, 44–52.

158 A. Kann, H. Hartmann, A. Besmehn, P. J. C. Hausoul and R. Palkovits, *ChemSusChem*, 2018, **11**, 1857–1865.

159 A. Jaleel, S.-H. Kim, P. Natarajan, G. H. Gunasekar, K. Park, S. Yoon and K.-D. Jung, *J. CO2 Util.*, 2020, **35**, 245–255.

160 B. An, L. Zeng, M. Jia, Z. Li, Z. Lin, Y. Song, Y. Zhou, J. Cheng, C. Wang and W. Lin, *J. Am. Chem. Soc.*, 2017, **139**, 17747–17750.

161 C. Wu, F. Irshad, M. Luo, Y. Zhao, X. Ma and S. Wang, *ChemCatChem*, 2019, **11**, 1256–1263.

162 D. T. Whipple and P. J. A. Kenis, *J. Phys. Chem. Lett.*, 2010, **1**, 3451–3458.

163 J.-P. Jones, G. K. S. Prakash and G. A. Olah, *Isr. J. Chem.*, 2014, **54**, 1451–1466.

164 X. Lu, D. Y. C. Leung, H. Wang, M. K. H. Leung and J. Xuan, *ChemElectroChem*, 2014, **1**, 836–849.

165 J. Qiao, Y. Liu, F. Hong and J. Zhang, *Chem. Soc. Rev.*, 2014, **43**, 631–675.

166 A. Taheri and L. A. Berben, *Chem. Commun.*, 2016, **52**, 1768–1777.

167 G. Zhao, X. Huang, X. Wang and X. Wang, *J. Mater. Chem. A*, 2017, **5**, 21625–21649.

168 A. Liu, M. Gao, X. Ren, F. Meng, Y. Yang, L. Gao, Q. Yang and T. Ma, *J. Mater. Chem. A*, 2020, **8**, 3541–3562.

169 W.-H. Wang, X. Feng and M. Bao, in *Transformation of Carbon Dioxide to Formic Acid and Methanol*, ed. W.-H. Wang, X. Feng and M. Bao, Springer Singapore, Singapore, 2018, pp. 43–52, DOI: 10.1007/978-981-10-3250-9_3.

170 E. Boutin, L. Merakeb, B. Ma, B. Boudy, M. Wang, J. Bonin, E. Anxolabéhère-Mallart and M. Robert, *Chem. Soc. Rev.*, 2020, **49**, 5772–5809.

171 D.-H. Nam, P. De Luna, A. Rosas-Hernández, A. Thevenon, F. Li, T. Agapie, J. C. Peters, O. Shekhah, M. Eddaoudi and E. H. Sargent, *Nat. Mater.*, 2020, **19**, 266–276.

172 B. M. Ceballos and J. Y. Yang, *Proc. Natl. Acad. Sci. U. S. A.*, 2018, **115**, 12686.

173 B. M. Ceballos and J. Y. Yang, *Organometallics*, 2020, **39**, 1491–1496.

174 Z. Sun, T. Ma, H. Tao, Q. Fan and B. Han, *Chem*, 2017, **3**, 560–587.

175 C. W. Lee, N. H. Cho, S. W. Im, M. S. Jee, Y. J. Hwang, B. K. Min and K. T. Nam, *J. Mater. Chem. A*, 2018, **6**, 14043–14057.

176 S. Zhao, S. Li, T. Guo, S. Zhang, J. Wang, Y. Wu and Y. Chen, *Nano-Micro Lett.*, 2019, **11**, 62.

177 R. Kortlever, J. Shen, K. J. P. Schouten, F. Calle-Vallejo and M. T. M. Koper, *J. Phys. Chem. Lett.*, 2015, **6**, 4073–4082.

178 A. S. Agarwal, Y. Zhai, D. Hill and N. Sridhar, *ChemSusChem*, 2011, **4**, 1301–1310.

179 A. J. Bard, R. Parsons and J. Jordan, *Standard potentials in aqueous solutions*, CRC Press, 1985.

180 R. Francke, B. Schille and M. Roemelt, *Chem. Rev.*, 2018, **118**, 4631–4701.

181 B. P. Sullivan, *Platinum Met. Rev.*, 1989, **33**, 2–9.

182 M. König, J. Vaes, E. Klemm and D. Pant, *iScience*, 2019, **19**, 135–160.

183 Q. Zhu, J. Ma, X. Kang, X. Sun, H. Liu, J. Hu, Z. Liu and B. Han, *Angew. Chem., Int. Ed.*, 2016, **55**, 9012–9016.

1242 | *Energy Environ. Sci.*, 2021, **14**, 1194–1246

This journal is © The Royal Society of Chemistry 2021

184 H. Wu, J. Song, C. Xie, Y. Hu and B. Han, *Green Chem.*, 2018, **20**, 1765–1769.

185 C. Xia, P. Zhu, Q. Jiang, Y. Pan, W. Liang, E. Stavitski, H. N. Alshareef and H. Wang, *Nat. Energy*, 2019, **4**, 776–785.

186 L. Fan, C. Xia, P. Zhu, Y. Lu and H. Wang, *Nat. Commun.*, 2020, **11**, 3633.

187 K. S. Udupa, G. S. Subramanian and H. V. K. Udupa, *Electrochim. Acta*, 1971, **16**, 1593–1598.

188 F. Köleli, T. Atilan, N. Palamut, A. M. Gizir, R. Aydin and C. H. Hamann, *J. Appl. Electrochem.*, 2003, **33**, 447–450.

189 W. Paik, T. N. Andersen and H. Eyring, *Electrochim. Acta*, 1969, **14**, 1217–1232.

190 N. Ikemiya, K. Natsui, K. Nakata and Y. Einaga, *RSC Adv.*, 2017, **7**, 22510–22514.

191 J. Resasco, L. D. Chen, E. Clark, C. Tsai, C. Hahn, T. F. Jaramillo, K. Chan and A. T. Bell, *J. Am. Chem. Soc.*, 2017, **139**, 11277–11287.

192 S. Kaneco, R. Iwao, K. Iiba, K. Ohta and T. Mizuno, *Energy*, 1998, **23**, 1107–1112.

193 Y. Tomita, S. Teruya, O. Koga and Y. Hori, *J. Electrochem. Soc.*, 2000, **147**, 4164.

194 D. Yang, Q. Zhu and B. Han, *Innovation*, 2020, **1**, 100016.

195 Y. Wang, M. Hatakeyama, K. Ogata, M. Wakabayashi, F. Jin and S. Nakamura, *Phys. Chem. Chem. Phys.*, 2015, **17**, 23521–23531.

196 J. D. Watkins and A. B. Bocarsly, *ChemSusChem*, 2014, **7**, 284–290.

197 X. Zhang, Y. Zhao, S. Hu, M. E. Gliege, Y. Liu, R. Liu, L. Scudiero, Y. Hu and S. Ha, *Electrochim. Acta*, 2017, **247**, 281–287.

198 T. N. Huan, P. Simon, G. Rousse, I. Génois, V. Artero and M. Fontecave, *Chem. Sci.*, 2017, **8**, 742–747.

199 N. Hollingsworth, S. F. R. Taylor, M. T. Galante, J. Jacquemin, C. Longo, K. B. Holt, N. H. de Leeuw and C. Hardacre, *Angew. Chem., Int. Ed.*, 2015, **54**, 14164–14168.

200 A. Atifi, D. W. Boyce, J. L. DiMeglio and J. Rosenthal, *ACS Catal.*, 2018, **8**, 2857–2863.

201 Y. Matsubara, D. C. Grills and Y. Kuwahara, *ACS Catal.*, 2015, **5**, 6440–6452.

202 D. Raciti, M. Mao, J. H. Park and C. Wang, *J. Electrochem. Soc.*, 2018, **165**, F799–F804.

203 M. Jitaru, D. A. Lowy, M. Toma, B. C. Toma and L. Oniciu, *J. Appl. Electrochem.*, 1997, **27**, 875–889.

204 Y. Hori, *Modern Aspects of Electrochemistry*, Springer, New York, 2008.

205 P. Bumroongsakulsawat and G. H. Kelsall, *Electrochim. Acta*, 2014, **141**, 216–225.

206 M. Ramdin, A. R. T. Morrison, M. de Groen, R. van Haperen, R. de Kler, E. Irtem, A. T. Laitinen, L. J. P. van den Broeke, T. Breugelmans, J. P. M. Trusler, W. D. Jong and T. J. H. Vlugt, *Ind. Eng. Chem. Res.*, 2019, **58**, 22718–22740.

207 K. Hara, A. Kudo and T. Sakata, *J. Electroanal. Chem.*, 1995, **391**, 141–147.

208 F. Proietto, B. Schiavo, A. Galia and O. Scialdone, *Electrochim. Acta*, 2018, **277**, 30–40.

209 A. R. T. Morrison, V. van Beusekom, M. Ramdin, L. J. P. van den Broeke, T. J. H. Vlugt and W. de Jong, *J. Electrochem. Soc.*, 2019, **166**, E77–E86.

210 M. Ramdin, A. R. T. Morrison, M. de Groen, R. van Haperen, R. de Kler, L. J. P. van den Broeke, J. P. M. Trusler, W. de Jong and T. J. H. Vlugt, *Ind. Eng. Chem. Res.*, 2019, **58**, 1834–1847.

211 J. Li, Y. Kuang, Y. Meng, X. Tian, W.-H. Hung, X. Zhang, A. Li, M. Xu, W. Zhou, C.-S. Ku, C.-Y. Chiang, G. Zhu, J. Guo, X. Sun and H. Dai, *J. Am. Chem. Soc.*, 2020, **142**, 7276–7282.

212 K. Hara and T. Sakata, *Bull. Chem. Soc. Jpn.*, 1997, **70**, 571–576.

213 M. Todoroki, K. Hara, A. Kudo and T. Sakata, *J. Electroanal. Chem.*, 1995, **394**, 199–203.

214 T. Mizuno, K. Ohta, A. Sasaki, T. Akai, M. Hirano and A. Kawabe, *Energy Sources*, 1995, **17**, 503–508.

215 M. B. Ross, P. De Luna, Y. Li, C.-T. Dinh, D. Kim, P. Yang and E. H. Sargent, *Nat. Catal.*, 2019, **2**, 648–658.

216 F. Lei, W. Liu, Y. Sun, J. Xu, K. Liu, L. Liang, T. Yao, B. Pan, S. Wei and Y. Xie, *Nat. Commun.*, 2016, **7**, 12697.

217 N. Han, H. Yang, J. Deng, J. Wu, Y. Li, Y. Wang and Y. Li, *Nat. Commun.*, 2018, **9**, 1320.

218 J. T. Song, H. Song, B. Kim and J. Oh, *Catalysts*, 2019, **9**, 224.

219 S. Lee, H. Ju, R. Machund, S. Uhm, J. K. Lee, H. J. Lee and J. Lee, *J. Mater. Chem. A*, 2015, **3**, 3029–3034.

220 Q. Wang, H. Dong and H. Yu, *J. Power Sci.*, 2014, **271**, 278–284.

221 Q. Wang, H. Dong and H. Yu, *RSC Adv.*, 2014, **4**, 59970–59976.

222 D. Kopljar, A. Inan, P. Vindayer, N. Wagner and E. Klemm, *J. Appl. Electrochem.*, 2014, **44**, 1107–1116.

223 A. D. Castillo, M. Alvarez-Guerra, J. Solla-Gullón, A. Sáez, V. Montiel and A. Irabien, *Appl. Energy*, 2015, **157**, 165–173.

224 Y. Fu, Y. Li, X. Zhang, Y. Liu, J. Qiao, J. Zhang and D. P. Wilkinson, *Appl. Energy*, 2016, 175.

225 A. Del Castillo, M. Alvarez-Guerra, J. Solla-Gullon, A. Saez, V. Montiel and A. Irabien, *J. CO2 Util.*, 2017, **18**, 222–228.

226 H. Xiang, H. A. Miller, M. Bellini, H. Christensen, K. Scott, S. Rasul and E. H. Yu, *Sustainable Energy Fuels*, 2020, **4**, 277–284.

227 F. P. G. D. Arquer, O. S. Bushuyev, P. D. Luna, C. T. Dinh, A. Seifitokaldani, M. I. Saidaminov, C. S. Tan, L. N. Quan, A. Proppe, M. G. Kibria, S. O. Kelley, D. Sinton and E. H. Sargent, *Adv. Mater.*, 2018, **30**, 1802858.

228 S. Min, X. Yang, A.-Y. Lu, C.-C. Tseng, M. N. Hedhili, L.-J. Li and K.-W. Huang, *Nano Energy*, 2016, **27**, 121–129.

229 Y. Wang, J. Zhou, W. Lv, H. Fang and W. Wang, *Appl. Surf. Sci.*, 2016, **362**, 394–398.

230 X. An, S. Li, A. Yoshida, T. Yu, Z. Wang, X. Hao, A. Abudula and G. Guan, *ACS Appl. Mater. Interfaces*, 2019, **11**, 42114–42122.

231 X. Zhang, X. Sun, S.-X. Guo, A. M. Bond and J. Zhang, *Energy Environ. Sci.*, 2019, **12**, 1334–1340.

232 F. Pan and Y. Yang, *Energy Environ. Sci.*, 2020, **13**, 2275–2309.

This journal is © The Royal Society of Chemistry 2021

Energy Environ. Sci., 2021, **14**, 1194–1246 | 1243

233 T. E. Teeter and P. Van Rysselberghe, *J. Chem. Phys.*, 1954, **22**, 759–760.

234 Y. Hori, in *Modern Aspects of Electrochemistry*, ed. C. G. Vayenas, R. E. White and M. E. Gamboa-Aldeco, Springer, New York, 2008, vol. 42, pp. 89–189.

235 C. H. Lee and M. W. Kanan, *ACS Catal.*, 2015, **5**, 465–469.

236 Z. Tao, Z. Wu, Y. Wu and H. Wang, *ACS Catal.*, 2020, **10**, 9271–9275.

237 Y. Hori, H. Wakebe, T. Tsukamoto and O. Koga, *Electrochim. Acta*, 1994, **39**, 1833–1839.

238 B. I. Podlovchenko, E. A. Kolyadko and S. Lu, *J. Electroanal. Chem.*, 1994, **373**, 185–187.

239 C. J. Stalder, S. Chao and M. S. Wrighton, *J. Am. Chem. Soc.*, 1984, **106**, 3673–3675.

240 X. Min and M. W. Kanan, *J. Am. Chem. Soc.*, 2015, **137**, 4701–4708.

241 M. Rahaman, A. Dutta and P. Broekmann, *ChemSusChem*, 2017, **10**, 1733–1741.

242 M. Liu, Y. Pang, B. Zhang, P. De Luna, O. Voznyy, J. Xu, X. Zheng, C. T. Dinh, F. Fan, C. Cao, F. P. Garcia de Arquer, T. S. Safaei, A. Mepham, A. Klinkova, E. Kumacheva, T. Filleter, D. Sinton, S. O. Kelley and E. H. Sargent, *Nature*, 2016, **537**, 382–386.

243 H. Jiang, Z. Hou and Y. Luo, *Angew. Chem., Int. Ed.*, 2017, **56**, 15617–15621.

244 S. Kim, W. J. Dong, S. Gim, W. Sohn, J. Y. Park, C. J. Yoo, H. W. Jang and J.-L. Lee, *Nano Energy*, 2017, **39**, 44–52.

245 G. Wen, D. U. Lee, B. Ren, F. M. Hassan, G. Jiang, Z. P. Cano, J. Gostick, E. Croiset, Z. Bai, L. Yang and Z. Chen, *Adv. Energy Mater.*, 2018, **8**, 1802427.

246 D. Wu, X. Shen, J. Liu, C. Wang, Y. Liang, X.-Z. Fu and J.-L. Luo, *Nanoscale*, 2019, **11**, 22125–22133.

247 R. Kortlever, I. Peters, S. Koper and M. T. M. Koper, *ACS Catal.*, 2015, **5**, 3916–3923.

248 W. Ma, S. Xie, X.-G. Zhang, F. Sun, J. Kang, Z. Jiang, Q. Zhang, D.-Y. Wu and Y. Wang, *Nat. Commun.*, 2019, **10**, 892.

249 W. Luc, C. Collins, S. Wang, H. Xin, K. He, Y. Kang and F. Jiao, *J. Am. Chem. Soc.*, 2017, **139**, 1885–1893.

250 V. S. S. Mosali, X. Zhang, Y. Zhang, T. Gengenbach, S.-X. Guo, G. Puxty, M. D. Horne, A. M. Bond and J. Zhang, *ACS Sustainable Chem. Eng.*, 2019, **7**, 19453–19462.

251 R. Kortlever, C. Balemans, Y. Kwon and M. T. M. Koper, *Catal. Today*, 2015, **244**, 58–62.

252 X. Zheng, P. De Luna, F. P. Garcia de Arquer, B. Zhang, N. Becknell, M. B. Ross, Y. Li, M. N. Banis, Y. Li, M. Liu, O. Voznyy, C. T. Dinh, T. Zhuang, P. Stadler, Y. Cui, X. Du, P. Yang and E. H. Sargent, *Joule*, 2017, **1**, 794–805.

253 Y.-W. Choi, F. Scholten, I. Sinev and B. Roldan Cuenya, *J. Am. Chem. Soc.*, 2019, **141**, 5261–5266.

254 X. Bai, W. Chen, C. Zhao, S. Li, Y. Song, R. Ge, W. Wei and Y. Sun, *Angew. Chem., Int. Ed.*, 2017, **56**, 12219–12223.

255 X. Zheng, Y. Ji, J. Tang, J. Wang, B. Liu, H.-G. Steinruck, K. Lim, Y. Li, M. F. Toney, K. Chan and Y. Cui, *Nat. Catal.*, 2019, **2**, 55–61.

256 K. Ye, Z. Zhou, J. Shao, L. Lin, D. Gao, N. Ta, R. Si, G. Wang and X. Bao, *Angew. Chem., Int. Ed.*, 2020, **59**, 4814–4821.

257 Y. Chen and M. W. Kanan, *J. Am. Chem. Soc.*, 2012, **134**, 1986–1989.

258 S. Zhang, P. Kang and T. J. Meyer, *J. Am. Chem. Soc.*, 2014, **136**, 1734–1737.

259 D. H. Won, C. H. Choi, J. Chung, M. W. Chung, E.-H. Kim and S. I. Woo, *ChemSusChem*, 2015, **8**, 3092–3098.

260 R. Zhang, W. Lv and L. Lei, *Appl. Surf. Sci.*, 2015, **356**, 24–29.

261 A. Dutta, A. Kuzume, M. Rahaman, S. Vesztergom and P. Broekmann, *ACS Catal.*, 2015, **5**, 7498–7502.

262 M. F. Baruch, J. E. Pander, J. L. White and A. B. Bocarsly, *ACS Catal.*, 2015, **5**, 3148–3156.

263 T. Yuan, Z. Hu, Y. Zhao, J. Fang, J. Lv, Q. Zhang, Z. Zhuang, L. Gu and S. Hu, *Nano Lett.*, 2020, **20**, 2916–2922.

264 F. Li, L. Chen, G. P. Knowles, D. R. MacFarlane and J. Zhang, *Angew. Chem., Int. Ed.*, 2017, **56**, 505–509.

265 S. Gao, Y. Lin, X. Jiao, Y. Sun, Q. Luo, W. Zhang, D. Li, J. Yang and Y. Xie, *Nature*, 2016, **529**, 68–71.

266 K. Mou, Z. Chen, S. Yao and L. Liu, *Electrochim. Acta*, 2018, **289**, 65–71.

267 E. Bertin, S. Garbarino, C. Roy, S. Kazemi and D. Guay, *J. CO2 Util.*, 2017, **19**, 276–283.

268 C. W. Lee, J. S. Hong, K. D. Yang, K. Jin, J. H. Lee, H.-Y. Ahn, H. Seo, N.-E. Sung and K. T. Nam, *ACS Catal.*, 2018, **8**, 931–937.

269 S. Rasul, A. Pugnant, H. Xiang, J.-M. Fontmorin and E. H. Yu, *J. CO2 Util.*, 2019, **32**, 1–10.

270 Y. Amao, *J. CO2 Util.*, 2018, **26**, 623–641.

271 A. R. Oliveira, C. Mota, C. Mourato, R. M. Domingos, M. F. A. Santos, D. Gesto, B. Guigliarelli, T. Santos-Silva, M. J. Romao and I. A. Cardoso Pereira, *ACS Catal.*, 2020, **10**, 3844–3856.

272 T. Reda, C. M. Plugge, N. J. Abram and J. Hirst, *Proc. Natl. Acad. Sci. U. S. A.*, 2008, **105**, 10654–10658.

273 F. A. Armstrong and J. Hirst, *Proc. Natl. Acad. Sci. U. S. A.*, 2011, **108**, 14049.

274 A. Bassegoda, C. Madden, D. W. Wakerley, E. Reisner and J. Hirst, *J. Am. Chem. Soc.*, 2014, **136**, 15473–15476.

275 K. Sakai, Y. Kitazumi, O. Shirai, K. Takagi and K. Kano, *Electrochem. Commun.*, 2016, **73**, 85–88.

276 L. B. Maia, I. Moura and J. J. G. Moura, *Inorg. Chim. Acta*, 2017, **455**, 350–363.

277 J. Seo, J. Shearer, P. G. Williard and E. Kim, *Dalton Trans.*, 2019, **48**, 17441–17444.

278 T. Fogeron, T. K. Todorova, J.-P. Porcher, M. Gomez-Mingot, L.-M. Chamoreau, C. Mellot-Draznieks, Y. Li and M. Fontecave, *ACS Catal.*, 2018, **8**, 2030–2038.

279 T. Fogeron, P. Retailleau, M. Gomez-Mingot, Y. Li and M. Fontecave, *Organometallics*, 2019, **38**, 1344–1350.

280 A. Mouchfiq, T. K. Todorova, S. Dey, M. Fontecave and V. Mougel, *Chem. Sci.*, 2020, **11**, 5503–5510.

281 C. Finn, S. Schnittger, L. J. Yellowlees and J. B. Love, *Chem. Commun.*, 2012, **48**, 1392–1399.

282 C. Costentin, M. Robert and J.-M. Savéant, *Chem. Soc. Rev.*, 2013, **42**, 2423–2436.

283 D. W. Cunningham, J. M. Barlow, R. S. Velazquez and J. Y. Yang, *Angew. Chem., Int. Ed.*, 2020, **59**, 4443–4447.

1244 | *Energy Environ. Sci.*, 2021, **14**, 1194–1246

This journal is © The Royal Society of Chemistry 2021

284 P. Kang, C. Cheng, Z. Chen, C. K. Schauer, T. J. Meyer and M. Brookhart, *J. Am. Chem. Soc.*, 2012, **134**, 5500–5503.

285 P. Kang, T. J. Meyer and M. Brookhart, *Chem. Sci.*, 2013, **4**, 3497–3502.

286 S. T. Ahn, E. A. Bielinski, E. M. Lane, Y. Chen, W. H. Bernskoetter, N. Hazari and G. T. R. Palmore, *Chem. Commun.*, 2015, **51**, 5947–5950.

287 H. D. Manamperi, S. E. Witt and C. Turro, *ACS Appl. Energy Mater.*, 2019, **2**, 7306–7314.

288 S. Min, S. Rasul, H. Li, D. C. Grills, K. Takanabe, L.-J. Li and K.-W. Huang, *ChemPlusChem*, 2016, **81**, 166–171.

289 J. P. Collin, A. Jouaiti and J. P. Sauvage, *Inorg. Chem.*, 1988, **27**, 1986–1990.

290 N. D. Loewen, T. V. Neelakantan and L. A. Berben, *Acc. Chem. Res.*, 2017, **50**, 2362–2370.

291 M. D. Rail and L. A. Berben, *J. Am. Chem. Soc.*, 2011, **133**, 18577–18579.

292 A. Taheri, E. J. Thompson, J. C. Fettinger and L. A. Berben, *ACS Catal.*, 2015, **5**, 7140–7151.

293 A. W. Nichols, S. Chatterjee, M. Sabat and C. W. Machan, *Inorg. Chem.*, 2018, **57**, 2111–2121.

294 A. W. Nichols, S. L. Hooe, J. S. Kuehner, D. A. Dickie and C. W. Machan, *Inorg. Chem.*, 2020, **59**, 5854–5864.

295 C. Costentin, M. Robert and J.-M. Savéant, *Acc. Chem. Res.*, 2015, **48**, 2996–3006.

296 B. Mondal, P. Sen, A. Rana, D. Saha, P. Das and A. Dey, *ACS Catal.*, 2019, **9**, 3895–3899.

297 L. Chen, Z. Guo, X.-G. Wei, C. Gallenkamp, J. Bonin, E. Anxolabehere-Mallart, K.-C. Lau, T.-C. Lau and M. Robert, *J. Am. Chem. Soc.*, 2015, **137**, 10918–10921.

298 S. Roy, B. Sharma, J. Pecaut, P. Simon, M. Fontecave, P. D. Tran, E. Derat and V. Artero, *J. Am. Chem. Soc.*, 2017, **139**, 3685–3696.

299 S. Dey, T. K. Todorova, M. Fontecave and V. Mougel, *Angew. Chem., Int. Ed.*, 2020, **59**, 15726–15733.

300 S. P. Cronin, J. M. Strain, M. S. Mashuta, J. M. Spurgeon, R. M. Buchanan and C. A. Grapperhaus, *Inorg. Chem.*, 2020, **59**, 4835–4841.

301 M. Isaacs, F. Armijo, G. Ramirez, E. Trollund, S. R. Biaggio, J. Costamagna and M. J. Aguirre, *J. Mol. Catal. A: Chem.*, 2005, **229**, 249–257.

302 H. Zhao, Y. Zhang, B. Zhao, Y. Chang and Z. Li, *Environ. Sci. Technol.*, 2012, **46**, 5198–5204.

303 B. Reuillard, K. H. Ly, T. E. Rosser, M. F. Kuehnel, I. Zebger and E. Reisner, *J. Am. Chem. Soc.*, 2017, **139**, 14425–14435.

304 D. B. Cluff, A. Arnold, J. C. Fettinger and L. A. Berben, *Organometallics*, 2019, **38**, 1230–1235.

305 R. Zhang, W. Lv, G. Li and L. Lei, *Mater. Lett.*, 2015, **141**, 63–66.

306 Q. Li, X. Zhang, X. Zhou, Q. Li, H. Wang, J. Yi, Y. Liu and J. Zhang, *J. CO2 Util.*, 2020, **37**, 106–112.

307 S. Zhang, P. Kang, S. Ubnoske, M. K. Brennaman, N. Song, R. L. House, J. T. Glass and T. J. Meyer, *J. Am. Chem. Soc.*, 2014, **136**, 7845–7848.

308 Y. Fang and J. C. Flake, *J. Am. Chem. Soc.*, 2017, **139**, 3399–3405.

309 H. Coskun, A. Aljabour, P. De Luna, D. Farka, T. Greunz, D. Stifter, M. Kus, X. Zheng, M. Liu, A. W. Hassel, W. Schöfberger, E. H. Sargent, N. S. Sariciftci and P. Stadler, *Sci. Adv.*, 2017, **3**, e1700686.

310 J. Huang, X. Guo, J. Yang and L. Wang, *J. CO2 Util.*, 2020, **38**, 32–38.

311 R. Lin, J. Guo, X. Li, P. Patel and A. Seifitokaldani, *Catalysts*, 2020, **10**, 473.

312 S. Liang, N. Altaf, L. Huang, Y. Gao and Q. Wang, *J. CO2 Util.*, 2020, **35**, 90–105.

313 C. Zhao and J. Wang, *Chem. Eng. J.*, 2016, **293**, 161–170.

314 T. Yamamoto, D. A. Tryk, A. Fujishima and H. Ohata, *Electrochim. Acta*, 2002, **47**, 3327–3334.

315 H. Li and C. Oloman, *J. Appl. Electrochem.*, 2005, **35**, 955–965.

316 J. J. Wu, F. G. Risalvato, P. P. Sharma, P. J. Pellechia, F. S. Ke and X. D. Zhou, *J. Electrochem. Soc.*, 2013, **160**, F953–F957.

317 Y. C. Li, D. Zhou, Z. Yan, R. H. Gonçalves, D. A. Salvatore, C. P. Berlinguette and T. E. Mallouk, *ACS Energy Lett.*, 2016, **1**, 1149–1153.

318 S. Pérez-Rodríguez, F. Barreras, E. Pastor and M. J. Lázaro, *Int. J. Hydrogen Energy*, 2016, **41**, 19756–19765.

319 D. Kopljar, A. Inan, P. Vindayer, N. Wagner and E. Klemm, *J. Appl. Electrochem.*, 2014, **44**, 1107–1116.

320 W. Lee, Y. E. Kim, M. H. Youn, S. K. Jeong and K. T. Park, *Angew. Chem., Int. Ed.*, 2018, **57**, 6883–6887.

321 L. Ma, S. Fan, D. Zhen, X. Wu, S. Liu, J. Lin, S. Huang, W. Chen and G. He, *Ind. Eng. Chem. Res.*, 2017, **56**, 10242–10250.

322 Y.-N. Li, L.-N. He, X.-D. Lang, X.-F. Liu and S. Zhang, *RSC Adv.*, 2014, **4**, 49995–50002.

323 H. Li and C. Oloman, *J. Appl. Electrochem.*, 2007, **37**, 1107–1117.

324 T. Li, E. W. Lees, Z. Zhang and C. P. Berlinguette, *ACS Energy Lett.*, 2020, **5**, 2624–2630.

325 Y. Hori, *J. Electrochem. Soc.*, 1983, **130**, 2387.

326 D. T. Whipple, E. C. Finke and P. J. A. Kenis, *Electrochem. Solid-State Lett.*, 2010, **13**, B109.

327 S. Nitopi, E. Bertheussen, S. B. Scott, X. Liu, A. K. Engstfeld, S. Horch, B. Seger, I. E. L. Stephens, K. Chan, C. Hahn, J. K. Nørskov, T. F. Jaramillo and I. Chorkendorff, *Chem. Rev.*, 2019, **119**, 7610–7672.

328 M. Jouny, W. Luc and F. Jiao, *Ind. Eng. Chem. Res.*, 2018, **57**, 2165–2177.

329 P. D. Luna, C. Hahn, D. Higgins, S. A. Jaffer, T. F. Jaramillo and E. H. Sargent, *Science*, 2019, eaav3506.

330 Y. Yang and F. Li, *Curr. Opin. Green Sustain. Chem.*, 2020, 100419, DOI: 10.1016/j.cogsc.2020.100419.

331 R. G. Grim, Z. Huang, M. T. Guarnieri, J. R. Ferrell, L. Tao and J. A. Schaidle, *Energy Environ. Sci.*, 2020, **13**, 472–494.

332 A. J. Martín and J. Pérez-Ramírez, *Joule*, 2019, **3**, 2602–2621.

333 L.-C. Weng, A. T. Bell and A. Z. Weber, *Energy Environ. Sci.*, 2019, **12**, 1950–1968.

334 C. M. Gabardo, C. P. O'Brien, J. P. Edwards, C. McCallum, Y. Xu, C.-T. Dinh, J. Li, E. H. Sargent and D. Sinton, *Joule*, 2019, **3**, 2777–2791.

This journal is © The Royal Society of Chemistry 2021

Energy Environ. Sci., 2021, **14**, 1194–1246 | 1245

335 Z. Yan, J. L. Hitt, J. A. Turner and T. E. Mallouk, *Proc. Natl. Acad. Sci. U. S. A.*, 2020, **117**, 12558.

336 Y. Lum, J. E. Huang, Z. Wang, M. Luo, D.-H. Nam, W. R. Leow, B. Chen, J. Wicks, Y. C. Li, Y. Wang, C.-T. Dinh, J. Li, T.-T. Zhuang, F. Li, T.-K. Sham, D. Sinton and E. H. Sargent, *Nat. Catal.*, 2020, **3**, 14–22.

337 S. Verma, S. Lu and P. J. A. Kenis, *Nat. Energy*, 2019, **4**, 466–474.

338 W. R. Leow, Y. Lum, A. Ozden, Y. Wang, D.-H. Nam, B. Chen, J. Wicks, T.-T. Zhuang, F. Li, D. Sinton and E. H. Sargent, *Science*, 2020, **368**, 1228.

339 J. P. Edwards, Y. Xu, C. M. Gabardo, C.-T. Dinh, J. Li, Z. Qi, A. Ozden, E. H. Sargent and D. Sinton, *Appl. Energy*, 2020, **261**, 114305.

340 C. M. Gabardo, A. Seifitokaldani, J. P. Edwards, C.-T. Dinh, T. Burdyny, M. G. Kibria, C. P. O'Brien, E. H. Sargent and D. Sinton, *Energy Environ. Sci.*, 2018, **11**, 2531–2539.

341 Y. Xu, J. P. Edwards, J. Zhong, C. P. O'Brien, C. M. Gabardo, C. McCallum, J. Li, C.-T. Dinh, E. H. Sargent and D. Sinton, *Energy Environ. Sci.*, 2020, **13**, 554–561.

342 C.-T. Dinh, T. Burdyny, M. G. Kibria, A. Seifitokaldani, C. M. Gabardo, F. P. García de Arquer, A. Kiani, J. P. Edwards, P. De Luna, O. S. Bushuyev, C. Zou, R. Quintero-Bermudez, Y. Pang, D. Sinton and E. H. Sargent, *Science*, 2018, **360**, 783.

343 Y. Chen, A. Vise, W. E. Klein, F. C. Cetinbas, D. J. Myers, W. A. Smith, T. G. Deutsch and K. C. Neyerlin, *ACS Energy Lett.*, 2020, **5**, 1825–1833.

344 S. Z. Oener, M. J. Foster and S. W. Boettcher, *Science*, 2020, **369**, 1099.

345 L. Pan, S. Ott, F. Dionigi and P. Strasser, *Curr. Opin. Electrochem.*, 2019, **18**, 61–71.

346 E. Jeng and F. Jiao, *React. Chem. Eng.*, 2020, **5**, 1768–1775.

347 B. Endrődi, E. Kecsenovity, A. Samu, F. Darvas, R. V. Jones, V. Török, A. Danyi and C. Janáky, *ACS Energy Lett.*, 2019, **4**, 1770–1777.

348 J. Hietala, A. Vouri, J. Pekka, P. Ilkka, W. Reutemann and K. Heinz, *Ullmann's Encyclopedia of Industrial Chemistry*, Wiley-VCH, Weinheim, Germany, 2000.

349 M. Pérez-Fortes, J. C. Jan, C. Schoneberger, A. Boulamanti, G. Harrison and E. Tzimas, *Int. J. Hydrogen Energy*, 2016, **41**, 16444–16462.

350 Global Formic Acid Market Report, https://dataintelo.com/report/formic-acid-market/, Accessed September 18, 2020.

351 G. T. Rochelle, *Science*, 2009, **325**, 1652–1654.

352 E. S. Rubin, J. E. Davison and H. J. Herzog, *Int. J. Greenhouse Gas Control*, 2015, **40**, 378–400.

353 S. Roussanaly, R. Anantharaman, K. Lindqvist and B. Hagen, *Sustainable Energy Fuels*, 2018, **2**, 1225–1243.

354 M. T. Ho, G. W. Allinson and D. E. Wiley, *Ind. Eng. Chem. Res.*, 2008, **47**, 1562–1568.

355 G. D. Surywanshi, B. B. K. Pillai, S. V. Patnaikuni, R. Vooradi and S. B. Anne, *Energy Sources, Part A*, 2019, **7036**, 1–16.

356 DNV, Carbon Dioxide Utilisation: Electrochemical Conversion of CO_2 – Opportunities and Challenges, https://issuu.com/dnv.com/docs/dnv-position_paper_co_2_utilization.

357 Mantra Releases Update on Demonstration Projects, https://www.marketscreener.com/MANTRA-VENTURE-GROUP-LTD-11095543/news/Mantra-Venture-Releases-Update-on-Demonstration-Projects-19806540/, Accessed September 18, 2020.

358 T. Schaub, D. M. Fries, R. Paciello, K.-D. Mohl, M. Schäfer, S. Rittinger and D. Schneider, Process for Preparing Formic Acid by Reaction of Carbon Dioxide with Hydrogen, *US Pat.*, US8791297B2, 2014.

359 D. Kim and J. Han, *Appl. Energy*, 2020, **264**, 114711.

360 R. Aldaco, I. Butnar, M. Margallo, J. Laso, M. Rumayor, A. Dominguez-Ramos, A. Irabien and P. E. Dodds, *Sci. Total Environ.*, 2019, **663**, 738–753.

361 M. Shemfe, S. Gadkari, E. Yu, S. Rasul, K. Scott, I. M. Head, S. Gu and J. Sadhukhan, *Bioresour. Technol.*, 2018, **255**, 39–49.

362 F. M. Baena-Moreno, L. Pastor-Perez, Z. Zhang and T. R. Reina, *Appl. Energy*, 2020, **268**, 115033.

363 M. Rumayor, A. Dominguez-Ramos and A. Irabien, *Appl. Sci.*, 2018, **8**, 914.

364 Y. Ahn, J. Byun, D. Kim, B.-S. Kim, C.-S. Lee and J. Han, *Green Chem.*, 2019, **21**, 3442–3455.

365 N. Thonemann and M. Pizzol, *Energy Environ. Sci.*, 2019, **12**, 2253–2263.

366 N. Thonemann and A. Schulte, *Environ. Sci. Technol.*, 2019, **53**, 12320–12329.

367 R. van Haperen, *Formic Acid as Energy Carrier*, Topsector Energie, 2016.

368 J. M. Douglas, *Conceptual design of chemical processes*, McGraw-Hill, 1988.

1246 | *Energy Environ. Sci.*, 2021, **14**, 1194–1246

This journal is © The Royal Society of Chemistry 2021